UNIVERSITÉ DE GENÈVE
Département de Physique
Nucléaire et Corpusculaire

FACULTÉ DES SCIENCES

Professeur Maurice Bourquin

Photon Structure Functions and Azimuthal Correlations from Lepton Pairs Produced in Tagged $\gamma\gamma$ Collisions.

THÈSE

présentée à la Faculté des Sciences
de l'Université de Genève
pour obtenir le grade de Docteur ès Sciences, mention Physique

par

Gabriele C. F. Susinno

de

Rome, Italie

Thèse No. —-

GENÈVE

1997

"Per correr miglior acque alza le vele
mai la navicella del mio ingegno,
che lascia dietro a sè mar sì crudele;
e canterò di quel secondo regno
ove l'umano spirito si purga
e di salire al ciel diventa degno."
Dante, Purgatorio I 1.

Remerciements

Mon premier, profond remerciement va à ma famille toute entière pour son soutien moral et intellectuel, pour avoir supporté mes humeurs alternes et m'avoir aidé a atteindre mes buts. Sans eux peu de choses auraient été possibles.

Un grand merci aux Professeurs Dieter Haidt de DESY et Michel Martin pour avoir accepté de faire partie de mon jury de thèse ainsi que pour leurs commentaires constructifs.

Je desire remercier Richard Nisius de l'expérience OPAL pour les discussions constructives sur les fonctions de structure ainsi que pour son aide et ses conseils.

Ma reconnaissance professionnelle va en premier lieu au Professeur M. Bourquin pour m'avoir accepté au sein de son équipe de recherche, me permettant ainsi d'aiguiser mes connaissances scientifiques et techniques dans un milieu éclectique et stimulant comme la collaboration L3. Provenant de la recherche en astrophysique, où les groupes de recherche sont encore constitués d'un nombre restreint de physiciens et où la plupart des progrès se contentent d'une approche qualitative, j'ai considéré ma nouvelle charge de physicien des particules, impliqué dans une expérience comme L3 dénombrant plus de cinq cents collaborateurs, comme un défi personnel que j'ai relevé avec le plus grand plaisir. Du point de vue scientifique, passer de l'étude des *quasars* à l'analyse des événements au LEP a été une transition qui a transporté mon intérêt au delà de la limite de dernière diffusion m'ouvrant l'accès à l'univers primordial au travers du "*grand télescope*" L3.

Ma reconnaissance est donc grande envers tous ceux qui m'ont permis de m'adapter, progresser et produire dans ce nouvel environnement. En particulier j'aimerais remercier le Dr. John H. Field pour l'ensemble de ses conseils éclairés ainsi que le Professeur Maria Kienzle pour avoir guidé mes recherches dans le physique des interactions photon-photon. Je remercie le Professeur Giulio D'Agostini de Rome pour le nombreuses discussions sur les techniques d'*unfolding* et sur l'approche bayesiène de ce problème. Je remercie mon cher collègue le Dr. Lotfi Fredj pour sa collaboration et pour les différends qui nous ont opposé lors de la conception du nouveau déclenchement à petit angle et qui ont permis, en amplifiant la synergie du groupe, de fournir l'expérience L3 d'un système de déclenchement stable et fiable. Je remercie les Docteurs Aurelio Bay et Williams Burger pour m'avoir permis de collaborer à la construction, au test et à l'installation du détecteur au silicium **SMD**.

Un grand remerciement à toute l'équipe d'ingénieurs électroniciens de l'Université de Genève qui ont toujours su satisfaire mes requêtes et cela dans la meilleure ambiance possible: P. Bené, B. Clerc, A. Léger et J.P. Richeux.

J'aimerais remercier fort chaleureusement tous mes collègues de travail: S. Braccini, C. Cecchi, M. Chemarin, P. Emonet, J. Fay, D. Goujon, H. Hoorani, F. Muheim et D. Sciarrino.

Contents

Chapitre 1

Resumé

Introduction

La physique des particules élémentaires vise à comprendre la nature de ces particules ainsi que leurs interactions. Les particules élémentaires, i.e. indivisibles puisque privées de structure interne, peuvent en principe participer à un nombre illimité de réactions mais il n'y a que quatre interactions fondamentales à la base de tout processus observé jusqu'à nos jours: l'interaction gravitationnelle, électromagnétique, faible et forte. Notre connaissance actuelle des particules et de leurs interactions est incorporée dans le Modèle Standard. Dans le cadre de ce modèle, les particules élémentaires se partagent en deux familles: les quarks et les leptons. Les quarks sont des particules de spin 1/2 et de charge fractionnaire ($+2/3e$ et $-1/3e$ où e est la charge de l' électron). Les leptons sont également des particules de spin 1/2 mais ils ont une charge entière. Si les quarks peuvent intervenir dans toutes les interactions fondamentales, les leptons ne subissent pas l'interaction forte. Au cours des années '60 Glashow, Weinberg et Salam ont formulé la theorie des interactions electrofaibles unifiant ainsi les interactions électromagnetiques et faibles dans un même modèle: le Modèle Standard des interactions électrofaibles [1]. Dans le Modèle Standard, basé sur la symetrie de jauge du groupe $SU(2) \times U(1)$, chaque interaction est transmise par l'échange d'un boson de jauge médiateur du champs de force correspondant: les bosons $W^{\pm}$, Z^o et γ qui sont donc les médiateurs de la force électrofaible. La Chromodynamique Quantique (QCD) decrit les interactions fortes, dans ce cas les gluons sont les médiateurs de la force forte. Enfin les gravitons jouent le rôle de médiateurs de la force gravitationnelle, mais il faut noter dans ce cas qu'une theorie quantique de l'interaction gravitationnelle est ancore loin de sa formulation définitive. L'existence des photons a été mise en évidence depuis 1905, l' observation d' événements à trois jets lors de collisions e^+e^- à PETRA (DESY) a permis la mise en évidence des gluons, alors que les expériences au collisionneur $p\overline{p}$ au CERN en 1983 ont permis l' observation des bosons médiateurs de l'interaction faible $W^{\pm}$ et Z^o. Les gravitons seuls restent à ce jour indétectés.

Le collisionneur LEP (Large Electron Positron Collider) a été construit afin de mesurer les paramètres du Modèle Standard et d'en vérifier la validité. En fonction au CERN depuis 1989, le LEP est à ce jour le plus grand collisionneur d' électrons-positrons au monde. Jusqu'en 1995, le LEP a fonctionné à une énergie dans le centre de masse d'environ 90 GeV permettant ainsi une copieuse production résonnante de bosons Z^o. Depuis, l'énergie des faisceaux a été augmentée ouvrant ainsi la possibilité de produire et étudier des paires W^+W^-.

Une classe d' événements de grand intérêt est constituée par les processus de diffusion photon-photon. Dans ce cas, les électrons et positrons du faisceau jouent le rôle de quasi spectateurs, la véritable collision ayant lieu entre deux photons virtuels émis lors d'une diffusion électron-positron. Ces types d'interactions sont d'un grand intérêt car caractéristiques du comportement quantique de l' électrodynamique. En effet, les équations classiques de l' électrodynamique interdisent les interactions des ondes électromagnétiques, alors que la formulation quantique de l' électrodynamique prédit l'existence d'interactions entre les photons via des fluctuations quantiques du vide. Par le principe d' indétermination, un photon peut fluctuer dans un état constitué d'une paire de particules dont le temps de vie est d'autant plus grand que l'énergie du photon est grande. Cela implique qu'aux énergies atteignables au LEP les paires de particules produites par l' oscillation de photons survivent suffisamment longtemps pour donner lieu à des interactions observables.

Les expériences de diffusion ont été, en physique des particules, un des domaines les plus riches en découvertes. Grâce à la nature duale du photon, (il est en même temps une particule et le quantum du champs de force électromagnétique), la diffusion d'un électron sur une cible est généralement considérée comme un sondage de la cible par un photon virtuel. Le fait que toute particule chargée soit entourée d'un nuage de photons virtuels, lesquels peuvent fluctuer dans des états de particule-antiparticule (polarisation du vide), permet de considérer le photon aussi comme cible. Lorsque un photon de haute virtualité (grand Q^2) est émis par un électron du faisceau diffusé à grand angle (étiqueté dans le détecteur), celui-ci peut être utilisé en tant que sonde permettant d'analyser la structure des fluctuations quantiques d'un photon cible de très faible virtualité (quasiment sur la couche de masse: $Q^2 \simeq 0$) entourant un électron[1] du faisceau opposé. La diffusion photon-photon peut donner lieu à un processus de diffusion profondement inélastique qui peut être étudié avec le même formalisme que celui utilisé pour la mise en évidence de la structure du proton lors des diffusions *ep*.

Dans cette thèse nous exposons notre étude de la production de paires de leptons par la réaction $e^+e^- \longrightarrow e^+e^-l\bar{l}$ $(l = e, \mu)$ en nous intéressant tout particulièrement à l'étude des fonctions de structure leptoniques du photon. Cette analyse, basée sur les données recueillies par l'expérience L3 à LEP de 1992 à 1994, outre à fournir un test de QED à l'ordre $O(\alpha^4)$, permet aussi un test expérimental des procédures qui par la suite pourront être appliquées à l'étude des fonctions de structure hadroniques du photon à L3.

Le LEP

Le LEP "*Large Electron Positron Collider*" est actuellement le plus grand collisionneur e^+e^- au monde. La conception de cette machine à démarré au CERN [2] en 1976, son but principal étant de permettre des tests précis de la théorie de jauge $SU(2) \times U(1)$ proposée par Glashow, Weinberg et Salam [3, 4] pour unifier les interactions électromagnétiques et faibles. Les premières collisions ont été enregistrées en 1989. Avec une énergie par faisceau de 45.6 GeV, une copieuse production de Z^o a pu démarrer en 1989 permettant ainsi des mesures de précision des paramètres du modèle standard.

[1] Pour des raisons de simplicité nous appelons aussi électrons les positrons du faisceau.

Les électrons et positrons, concentrés en paquets et circulant dans le LEP en directions opposées, sont mis en collision en quatre points de l' accélérateur en correspondance des quatre expériences L3 [5], ALEPH [6], OPAL [7] et DELPHI [8].Le LEP a été conçu pour fournir des faisceaux d' électrons et positrons à une énergie allant de 40 à 100 GeV, ceci permettant une étude détaillée de la résonance du Z^o (LEP1) ainsi que la production de paires de W^+W^- (LEP2). Le détécteur L3, dont les données ont été analysées dans cette thèse, a été conçu de façon à optimiser la résolution de la mesure de l'énergie pour $e^{\pm}$, γ et de l' impulsion des muons d'énergie supérieure à 2 GeV.

Le détecteur L3

Le détecteur L3 (figure 3.3) a été conçu pour permettre l'étude des collisions e^+e^- jusqu'à une énergie de 200 GeV dans le système du centre de masse. Le détecteur est composé d'une suite de sous-detecteurs à symétrie cylindrique imbriqués les uns dans les autres et contenus dans un aimant octogonal pesant 7800 tonnes et fournissant un champ magnétique de 0.5 Tesla. Une telle configuration a été choisie de sorte à optimiser la résolution sur la mesure de l' impulsion des muons qui augmente linéairement avec l'intensité du champs magnétique mais quadratiquement avec la longueur de la trace. Les détecteurs internes, sont dans l'ordre (du plus interne au plus externe): le détecteur de traces central, le calorimètre électromagnétique, les scintillateurs et le calorimètre hadronique. Ils sont soutenus mécaniquement par un tube de support en acier de 32 m de longueur et d'un diamètre de 4.5 m. A l'extérieur, entre le tube de support et les parois internes de l' aimant, sont logées trois couches de chambres proportionnelles permettant de reconstruire les traces des muons: les chambres à mu. Le système de coordonnées utilisé dans cette thèse est indiqué dans la figure 3.5. Les principaux détecteurs utilisés dans cette analyse sont:

- **Le détecteur de traces central**: Le détecteur de traces central, est constitué d'un détecteur de vertex au silicium, le SMD, et d'une chambre à fils fonctionnant en mode d' expansion temporelle, la TEC. Le tout est entouré de deux chambres proportionnelles de géometrie cylindrique, les chambres Z.

Dans les régions avant et arrière, où l'efficacité de la TEC est limitée par le petit nombre de fils touchés par les traces, il y a deux plans de tubes à dérive, les FTC, permettent d'augmenter l'efficacité de reconstruction des traces.

Le SMD, à la réalisation duquel nous avons participé activement (Annexe B), est constitué de deux couches d'échelles au silicium. La résolution du SMD seul est de 8 μm pour la mesure de la coordonnée $r - \phi$ et de 17 μm pour la coordonnée z. Le SMD a été installé en 1994.

La TEC est constituée de deux chambres à dérive cylindriques concentriques: la TEC interne et la TEC externe. L'extension radiale de la TEC interne va de 8.5 cm à 14.3 cm alors que la TEC externe s' étend jusqu'à 46.5 cm. La configuration des fils dans un secteur interne et externe de la TEC est montrée dans la figure 3.11.

- **Le calorimètre électromagnétique**: Le calorimètre électromagnétique entoure le détecteur de traces central et est utilisé pour une mesure de précision de l'énergie et de la position des électrons et photons. Il est constitué de 11360 cristaux de germanate de bismuth ($Bi_4Ge_3O_{12}$ par la suite appelé BGO). Les cristaux sont arrangés en un tonneau couvrant la zone centrale correspondant à $|\cos\theta| \leq 0.743$ et en deux bouchons couvrant les régions avant/arrière correspondant à $0.978 \leq |\cos\theta| \leq 0.788$. Chaque cristal a la forme d'une pyramide tronquée de 24 centimètres de longueur ($\simeq 22\ X_o$) dont l'axe est dirigé vers le point d'interaction. Une résolution de 1.4% à 45.6 GeVa été obtenue grâce à un système de monitoring faisant appel à la lumière produite par une lampe au Xenon.

- **Le calorimètre hadronique**: Le calorimètre hadronique, situé autour du calorimètre électromagnétique est constitué d'un tonneau central et d'un système de bouchons dans les régions avant/arrière. Il couvre 99.5% de l'angle solide total. Il est constitué de plaques de 5mm d'absorbeur d'uranium appauvri, intercalées par des chambres à fils proportionnelles. Le gaz utilisé dans les chambres est un mélange de 80% de Ar et 20% de CO_2 permettant une résolution en énergie de $0.55/\sqrt{E} + 0.05$ (E exprimé en GeV). La granularité pour la mesure du point d'impact est de $\Delta\theta = 2.5^o$ et $\Delta\phi = 3.5^o$.

- **Les détecteurs à petit angle polaire**: Pour maximiser la couverture aux petits angles polaires et pour optimiser la mesure de la luminosité du faisceau via la mesure de la section efficace d'événements Bhabha, le détecteur L3 est équipé d'un système de calorimètres à petit angle polaire. Dans notre analyse, nous avons utilisé ces détecteurs pour étiqueter les électrons du faisceau diffusés lors des interactions $\gamma\gamma$.

  – **Les LUMI**: Le rôle principal des moniteurs de luminosité (LUMI) est de fournir une mesure précise de la luminosité via la mesure du taux d' événements Bhabha. Il sont constitués d'un détecteur au silicium (SLUM) mesurant avec une grande précision le point d'impact des particules, suivi d'un calorimètre au BGO. Les moniteurs de luminosité couvrent les régions angulaires: $1.4^o \leq \theta \leq 3.9^o$ et $176.1^o \leq \theta \leq 178.6^o$. Ils sont donc placés de part et d'autre du point d'interaction. La précision dans la mesure de la luminosité, obtenue en utilisant le BGO seul, est de 0.6%. Le SLUM, installé en 1993, permet d' obtenir une mesure de la luminosité avec une précision de 0.05%. Notre analyse se base sur les événements photon-photon avec un électron du faisceau étiqueté dans les LUMI.

  – **Les ALR**: Les anneaux de plomb actifs (ALR), placés concentriquement à l'axe du faisceau de part et d'autre du point d'interaction (figure 3.19), couvrent une région angulaire correspondante à $0.9877 \leq \mid \cos\theta \mid \leq 0.9977$. Ils sont formés de 6 couches de plomb de 18.6 mm (3.3 X_o) intercalées de cinq couches de scintillateurs. En 1995 l'université de Genève a doté ce détecteur d'un système de déclenchement. Puisque nous avons été chargés de la conception et de la réalisation de ce déclenchement, l'annexe A lui est consacrée.

- **Déclenchement et acquisition des données**: A chaque croisement des faisceaux, les systèmes de déclenchement de L3 décident si oui ou non il faut garder l' événement. En cas de réponse positive, toutes les informations relatives à l' événement sont lues et transférées sur bande magnétique. Les système de déclenchement est composé de trois sous-systèmes de complexité croissante appelés niveau-1, niveau-2 et niveau-3. Une telle configuration minimise les temps morts et fournit un taux d' événements acceptés de l'ordre de 10 Hz.

L'acquisition des données fait principalement appel à des systèmes FASTBUS. Pour chaque événement lu, les informations stoquées dans les modules FASTBUS sont transférées vers l'ordinateur en ligne (VAX 8800) par le moyen d'une interface CHI (CERN Host Interface). Finalement, les événements sont transférés de la mémoire de la station VAX sur une bande magnétique.

Les procédures de déconvolution

Il est d'importance capitale en physique expérimentale d'établir des méthodes permettant de s'affranchir des effets des détecteurs sur les quantités observées de sorte à pouvoir fournir des résultats indépendant de la méthode de détection. Les méthodes de déconvolution (ou *unfolding*) jouent donc un rôle capital en physique expérimentale. En particulier dans la physique photon-photon, des événements hadroniques (jets) de faible énergie sont produits, avec une grande probabilité, à petit angle polaire. Les états finals ne sont donc qu'en partie détectés. Il faut donc déterminer le meilleur moyen de déconvoluer les effets d'acceptance et résolution propres au détecteur utilisé des distributions observées.

Supposons qu'une quantité physique x, définie sur un intervalle $[a, b]$ soit distribuée selon une distribution $f(x)$. Appelons y l'image de x vue au travers d'un détecteur, y sera distribué selon une distribution $o(y)$, et $A(x, y)$ décrira alors l'action du détecteur sur x. La distribution intéressante en physique est évidement $f(x)$ mais l'on observe $o(y)$ avec une erreur statistique $\sigma(y)$. Tout expérimentateur est alors forcé de résoudre l'équation aux valeurs propres de dimension finie suivante:

$$(\mathcal{A} - \sigma \cdot \mathbf{I})\vec{x} = \vec{o} \qquad \textit{(équation de Fredholm)} \tag{1.1}$$

ou sa version intégrale:

$$\int_a^b \mathcal{A}(x,y) \cdot f(x)dx + \sigma(y) = o(y) \qquad \textit{(équation intégrale de Fredholm de } 1^{ere} \textit{ espèce)} \tag{1.2}$$

La distribution de x peut être extraite des équations précédentes de façon triviale seulement dans le cas où l'effet dominant du détecteur est une acceptance limitée (i.e. A est une matrice diagonale). La solution dans un cas général est loin d'être triviale.

Dans le cadre de l'étude de la section efficace totale $\gamma\gamma \longrightarrow hadrons$, nous avons étudié différents algorithmes de déconvolution généralement utilisés en physique de hautes énergies. Ces algorithmes, étant basés sur le maximum de vraisemblance avec une hypothèse de départ sur l' allure générale de la solution (hypothèse de régularisation: lisse, lentement variable, etc.), ne peuvent pas être utilisés aveuglement et nécessitent d'être ajustés au problème étudié. Nous avons développé notre propre algorithme, mieux adapté aux exigences de notre analyse. Cet algorithme, que nous avons appelé *Aladino*, détermine par itérations successives la distribution de la variable physique x qui donne (en appliquant les équations de Fredholm) une distribution $o(y)$ qui soit la plus proche possible à la distribution réellement observée. Le schéma général de l'algorithme Aladino est représenté dans la figure 5.2. Cette méthode a été utilisée pour la détermination des corrélations azimuthales présentées dans cette thèse.

La sélection des événements

Dans une première étape, appelée présélection, les candidats leptoniques avec étiquetage sont sélectionnés par des coupures larges. On requièrt: un dépôt d'énergie de plus de 30 GeVdans les moniteurs de luminosité ou de plus de 10 GeVdans les bouchons du calorimètre électromagnétique. De plus cela doit être accompagné par au moins deux traces dans la TEC, devant satisfaire des réquisitions minimales, à savoir: au moins 5 fils touchés, la plus courte distance d'approche (DCA) inférieure à 10 mm et une impulsion transverse supérieure à 100 MeV. Les événements $\gamma\gamma \longrightarrow e^+e^-$, $\mu^+\mu^-$ avec étiquetage d'un seul électron du faisceau diffusé à grand angle sont ensuite extraits de l' échantillon présélectionné en exigeant:

- L' événement doit avoir une énergie totale déposée dans les calorimètres inférieure à 60 GeV.

- Les traces doivent se trouver à l'intérieur du volume fiduciel défini par: $28^o \leq \theta \leq 152^o$.

- Les traces doivent coïncider avec les dépôts d'énergie dans les calorimètres. La coïncidence est étudiée dans le plan $r - \phi$ et doit satisfaire la condition azimuthale: $\mid \phi_{TEC} - \phi_{BGO} \mid \leq 300$ mrad. La même procédure est appliquée pour étudier les correspondances entre le calorimètre électromagnétique et le calorimètre hadronique. En absence d'activité électromagnétique la coïncidence entre traces et dépôts d'énergie dans le calorimètre hadronique est directement étudiée.

- L'étiquetage est défini comme un et un seul dépot d'énergie supérieure à 75% de l'énergie du faisceau dans un volume fiduciel défini par: $1.55^o \leq \theta \leq 3.67^o$ ou $176.33^o \leq \theta \leq 178.45^o$.

- Seuls les événements avec une impulsion transverse totale au carré de plus de 0.015 GeV^2 sont considérés.

Les leptons de l'état final sont identifiés en analysant les caractéristiques des dépôts d'énergie dans les calorimètres. Les électrons sont identifiés en demandant que le rapport $R = E_{BGO} \sin \theta_{BGO} / P_{transverse}$ soit plus grand que 0.8, que l'énergie $E_{BGO} \geq 0.5$ GeVet qu'il n'y ait pas d'activité hadronique. Les muons sont identifiés en demandant un dépôt d'énergie inférieur à 0.40 GeVdans le calorimètre électromagnétique et, de plus, 95% de l'énergie mesurée doit être contenue dans au plus 6 cristaux. Une activité hadronique associée avec une trace sélectionnée doit être observée. De plus le nombre de fils touchés dans le calorimètre hadronique (normalisé au signal d'une particule au minimum d' ionisation) doit être supérieur à 0.5. Afin d'estimer le bruit de fond contaminant notre sélection, différents processus ont été analysés (table 6.5). Le bruit de fond contaminant le nombre d'événements sélectionnés est estimé être de $1.30\% \pm 0.04\%$ dans le cas des électrons et de $1.81\% \pm$

0.04% dans le cas des muons. Une erreur systématique sur le nombre d' événements sélectionnés a été estimé être de 1.90% dans le cas des électrons et de 3.2% dans le cas des muons.

Résultats

De la distribution du Q^2 observée on a extrait la distribution de la section efficace différentielle $d\sigma/dQ^2$ pour les états finals de di-électron et di-muon. Les résultats sont exposés dans la figure 7.1 . Dans le cas d'une diffusion profondement inélastique, la section efficace différentielle est étroitement liée à la fonction de structure F_2^γ par la relation: $F_2^\gamma(x, Q^2) =< K(x, Q^2) >^{-1} \cdot d^2\sigma/dxdQ^2$ où x est la variable de Bjorken et le facteur de correction $K(x, Q^2)$ peut être obtenu, dans chaque intervalle de x et de Q^2, à partir d'une simulation Monte Carlo. Dans le cas des muons, nous avons extrait par ce moyen la fonction de structure F_2^γ. Un clair effet imputable à la virtualité du photon cible a été observé (figure 7.2). En ajustant la fonction analytique pour F_2^γ sur les données expérimentales et en laissant la virtualité du photon cible comme paramètre libre, nous avons déduit une virtualité moyenne de $0.033 \pm 0.002\ GeV^2$ pour le photon cible. En introduisant cette valeur dans l'expression QED de $d\sigma/dQ^2$ nous avons obtenu les courbes théoriques représentées dans la figure 7.1. On remarque alors un excellent accord entre données expérimentales et prédiction théorique.

La fonction de structure F_2^γ n'est pas la seule à fournir des informations sur la structure du photon. En étudiant la distribution de l'angle azimutal χ dans le système du centre de masse des deux photons (figure 4.6), d'autres fonctions de structure peuvent être extraites. Elles sont reliées aux termes d' interférence de l' amplitude de diffusion de photons polarisés longitudinalement et transversalement comme montré dans la figure 4.7. Nous avons extrait, en quatre intervalles de x, la valeur expérimentale des fonctions de structure F_B^γ, décrivant l' interférence entre deux photons transverses, et F_A^γ décrivant l' interférence entre des états longitudinal-transverse et transverse-transverse des amplitudes de diffusion des deux photons en collision. Ces résultats sont en excellent accord avec les prévisions de QED.

Conclusions

Nous avons étudié la section efficace de la réaction $e^+e^- \longrightarrow e^+e^-l\bar{l}$ où $l = e, \mu$, dans le cas où l'un des deux électrons du faisceau est observé dans le détecteur de luminosité. Cette mesure a été effectuée à une énergie dans le centre de masse de 91 GeVutilisant les données collectées par le détecteur L3. Nous avons par la suite extrait la fonction de structure leptonique F_2^γ. La distribution expérimentale $F_2^\gamma(x)$ est sensiblement en désaccord avec avec les prédictions analytiques de QED si l'on néglige la virtualité du photon cible. En ajustant la courbe théorique sur les valeurs expérimentales, nous avons déduit une valeur moyenne de la virtualité du photon cible de $t^2 = 0.033 \pm 0.005$ GeV^2. Ce résultat doit être pris en compte dans l'étude des fonctions de structure hadroniques du photon puisque les parametrisations théoriques des fonctions de densité partoniques doivent inclure les effets de la virtualité du photon cible. De plus la contribution hadronique non-perturbative à la structure du photon, devrait s' annuler pour une virtualité du photon cible suffisamment élevé. La diminution de la partie non-perturbative avec l'augmentation de la virtualité du photon cible dépend du modèle utilisé et nécessite donc une clarification expérimentale. Une connaissance plus approfondie de cette transition est importante aussi pour l'extraction des fonctions de structure du photon dans le cas des événements à étiquetage simple.

L'étude des corrélations azimuthales dans le centre de masse du système $\gamma\gamma$ a permis d'extraire, pour la première fois, d'autres fonctions de structure reliées aux termes d' interférence entre différents états de polarisation des amplitudes de diffusion. Nous avons présenté ici la première mesure des fonctions de structure F_A^γ et F_B^γ. Une telle mesure de QED permet aussi de vérifier les procédures à utiliser pour l'extraction des fonction de structure hadroniques du photon. En effet, dans le cas leptonique, les particules produites lors de l'interaction $\gamma\gamma$ peuvent être identifiée et une mesure directe des différentes fonctions de structure est alors possible. De plus les prédictions théoriques découlent directement de la théorie des perturbations. Dans le cas hadronique par contre, les différentes fonctions de structure sont obtenues par convolution avec les densités partoniques du photon et dépendent donc des modèles sous-jacents, de plus la mesure des corrélations azimuthales nécessite une reconstruction très précise de l'état final hadronique. Le cas QED permet donc une étude détaillée des effets produits par les différentes hypothèses de travail et par les effets du détecteur sur la mesure des corrélations azimuthales.

Chapter 2

Introduction

The aim of elementary particle physics is to understand the nature of those particles and how they interact. Elementary particles are usually defined as particles that cannot be decomposed into constituents. Elementary particles participates to a virtually unlimited number of processes, but only four types of fundamental interactions have been observed so far: electromagnetic, weak, strong and gravitational. Our present knowledge of elementary particles and their interactions is embedded in the Standard Model. In the framework of this model, the elementary particles are divided into two families: quarks and leptons. Quarks are spin 1/2 fermions with a fractionary charge ($+2/3e$ and $-1/3e$ where $-e$ is the electron's charge). They participate in all the four fundamental interactions. Only six spin 1/2 fermions are known not to participate in strong interaction, they are the so-called leptons: the electron e, the muon μ, the tau-lepton τ and their neutrinos (ν_e, ν_μ, ν_τ).

In the Standard Model, each interaction is mediated by the exchange of a gauge boson. The electroweak force is mediated by the exchange of $W^\pm$, Z^o and γ bosons, the strong interaction is mediated by eight colored gluons and finally gravitons should play the role of gravitational force mediators [1]. The existence of the photon is an evidence since 1905, gluons have been discovered by observing three jets events in e^+e^- collisions at PETRA (DESY), while the mediators of the weak interaction have been observed in 1983 in $p\overline{p}$ collisions at CERN. For the time being only gravitons have not been observed.

The LEP (*Large Electron Positron*) collider, the biggest electron positron collider in the world, is functioning at CERN since 1989. The principal aim of this machine is to allow for a precise measurement of the Standard Model parameters. Until 1995 LEP has delivered approximately an integrated luminosity of 150 pb^{-1} at a center of mass energy of 90 GeVallowing for a resonant production of the Z^o boson. Since 1995, the LEP energy has been risen above the threshold of $W^+ W^-$ production.

An interesting class of events is constituted by the two-photon collisions. In this case scattered electrons and positrons emits virtual photons which can afterward collide. This kind of interaction is of great interest since it derives directly from the quantum formulation of electrodynamics. Equations of classical electrodynamics do not allow interactions between electromagnetic waves. However the quantum electrodynamics predicts photon-photon interactions via quantum fluctuations of the vacuum. By the uncertainty principle, a photon can fluctuate into a particle-antiparticle state (which must conserve the quantum numbers of the photon) whose lifetime is proportional to the photon energy. This imply that at the LEP energies, pairs of particles-antiparticles produced by those photon fluctuations can survive enough to produce observable interactions.

Scattering experiments have been source of a number of important discoveries in particle physics. The duality of the photon, which is a particle and a quantum of the electromagnetic field, allows to see electron-target scattering as a probe of the target by a virtual photon. Since charged particles are surrounded by a cloud of virtual photons, which can spent part of their time in a particle-antiparticle state (vacuum polarization), the photon can also be considered as a target. When a photon of high virtuality (high Q^2; Q^2 being the square of the momentum transfer) is emitted by a scattered electron (tagged) in an e^+e^- diffusion, this photon can be used as a probe to investigate the structure of quantum fluctuations of a target photon almost on-shell ($Q^2 \simeq 0$) belonging to the cloud surrounding a target particle (untagged). Thus, at high energies, two-photon interactions can give rise to a deep inelastic process. These processes can be studied using the same formalism adopted to bring in evidence the internal structure of the proton in *ep* scattering experiments.

Recently, untagged $\gamma\gamma$ events have been used to measure the running coupling constant $\alpha_{QED}(Q^2)$ by the TOPAZ [9] experiment. The measurement has been performed at $Q^2 = 57.77$ GeV^2. The cross-section of $e^+e^- \longrightarrow e^+e^-\mu^+\mu^-$ where both final electrons are untagged is proportional to $\alpha^4_{QED}(Q^2 \simeq 0)$. Measuring the ratio between the cross-section of $e^+e^- \longrightarrow \mu^+\mu^-$ and $e^+e^- \longrightarrow e^+e^-\mu^+\mu^-$ allows for a direct measurement of the ratio $\alpha^2_{QED}(Q^2)/\alpha^4_{QED}(0)$. This method notably reduces the systematic errors on the final result.

Hadronic two-photon events, where a $q\overline{q}$ final state is produced by the two colliding photons, are of capital interest in QCD. In this case the quark and gluon contents of the photon can be investigated. Varying the virtuality of the incoming photons can helps to better define the interplay between perturbative short-distance and non-perturbative large-distance QCD mechanism [10]. Moreover, if next-to-leading order contributions are properly taken into account, the scale parameter Λ_{QCD} can be extracted from the absolute value of the photon structure functions [11].

Electron-positron colliders are well suited for the study of photon-photon interactions. Since the cross-section of those interactions rises with the energy of the beams, high energy e^+e^- collider are mostly two-photon colliders.

A deep understanding of $\gamma\gamma$ interactions, as well as being of great interest in its own right, is essential for the study of other physical reactions. At LEP energies the two-photon processes are one of the principal sources of background to other physical processes, due to their high cross-section and the variety of their final states.

In this thesis we expose our study of di-lepton pairs production by the two-photon reaction $e^+e^- \longrightarrow e^+e^-l\overline{l}$ ($l = e, \mu$). The analyzed data sample has been collected with the L3 detector from 1992 to 1994. We have focussed our interest in the extraction of different leptonic structure functions of the photon. This analysis, as well as being a test of QED up to the order $O(\alpha^4)$, allows to define and test procedures used to extract different structure functions of the photon. Since in the QED case the final states are clearly signed and the theoretical expectations can be analytically computed, the effects on the final results, induced by the approximations and by the detector effects, can be studied. Consequently these results can be applied in studies of hadronic two photon reactions with the L3 detector.

After a concise description of the L3 detector in Chap. 3, in Chap. 4 we will review the theoretical framework acquired for the analysis presented in this thesis. Different procedures of unfolding are presented in Chap. 5. In Chap. 6 we describe the method applied to extract the sample of di-electron and di-muon events originating from tagged $\gamma\gamma$ collisions. The determination of the leptonic structure functions of the photon, related to the different helicity states of the colliding $\gamma\gamma$ system, is exposed in Chap. 7.

Chapter 3

LEP Collider and L3 detector

The conception of LEP has begun at CERN [2] in 1976. The aim of this accelerator, which is the most powerful electron-positron collider in the world, is to allow for a precise test of the gauge theory $SU(2) \times U(1)$ proposed by Weinberg and Salam [3, 4] to unify electromagnetic and weak interactions. The conception and the construction of LEP took more than ten years and the first e^+e^- collisions have been produced in 1989. With a beam energy of 45.6 GeV, a copious production of Z^o bosons has begun allowing for a precision measurements of Standard Model parameters. The realization of LEP has been done in parallel with the progresses in the study of a gauge theory of strong interactions (QCD), describing colored quarks interactions via eight gauge bosons called gluons. Therefore, at the end of eighties physicists had both technical and theoretical tools to perform precise tests of the models describing three of the four fundamental interactions.

The LEP is contained in a "circular" tunnel with a circumference of about 26.7 Km located at the French-Swiss border near Geneva (Fig. 3.1) and lies some 50 to 150 meters below ground level. The LEP ring contains eight straight and eight curved sections. Electrons and positrons, concentrated in 4 or 8 bunches each are brought into collision in the middle of four of the eight straight sections. Those regions, equally spaced, corresponds to the location of the four detectors: L3 [5], ALEPH [6], OPAL [7] et DELPHI [8]. In the four points corresponding to the middle of the remaining straight sections, electrostatic separators prevent bunches to collide.

Even though these detectors have been conceived to study the same physics, they have distinctive features in technologies adopted for particle detection. In particular the L3 detector, whose data have been analyzed in this thesis, has been conceived in order to optimize the energy measurement resolution for $e^{\pm}$, γ and the momentum resolution for muons above 2 GeV.

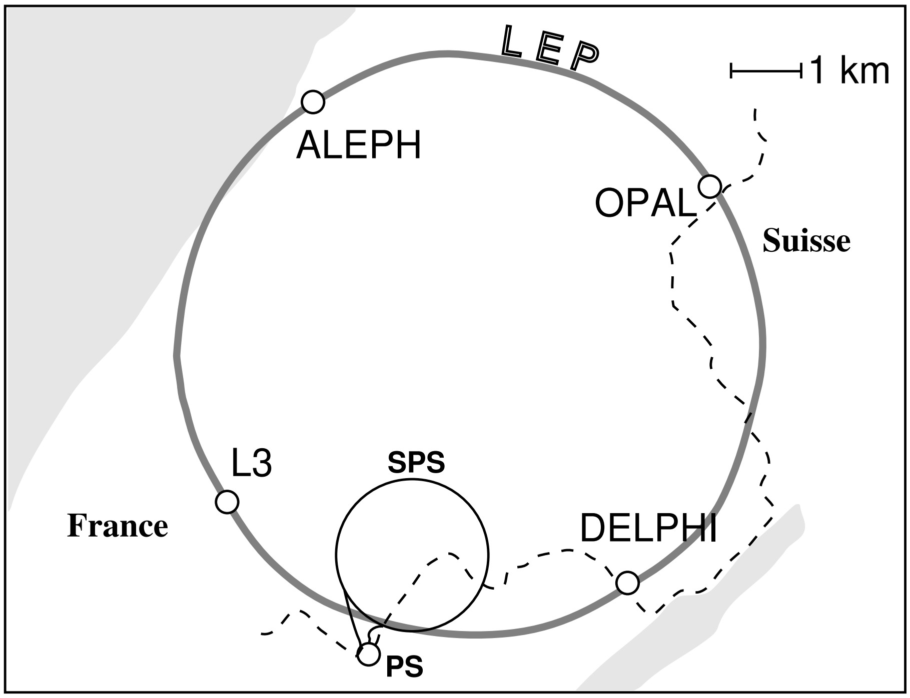

Figure 3.1: The map of LEP with its four detectors.

3.1 The LEP

The LEP has been designed to produce 40 to 100 GeVelectron and positron beams to allow a detailed study of the Z^o resonance (LEP1) and the production of W^+W^- pairs (LEP2). The dimensions of the LEP ring are a compromise between geological constraints and construction costs. The circumference has been chosen as large as possible to reduce the energy loss, due to synchrotron radiation suffered by accelerated charged particles. The energy loss per revolution being proportional to E_b^4/R, where E_b is the beam energy and R the radius of the orbit, a 45 GeVelectron in LEP loses 220 MeVper turn.

The LEP storage ring is constituted by eight linear sections and eight curved sections. Each one of the curved sections is constituted by 31 standard cells which are comprised of bending dipole magnets, and focusing quadrupole and sextupole magnets. The bending field of these dipoles is 0.1 Tesla. In LEP1, the acceleration is performed by 128 copper radio-frequency cavities [12] grouped in four sets and disposed in both sides of the interaction points P2 and P6.

The luminosity delivered by the machine is given by [13]:

$$\mathcal{L} = \frac{N_e N_p N_b f_{rev}}{4\pi \sigma_x \sigma_y}$$

where N_e and N_p are the number of electrons and positrons per bunch, respectively, N_b the number of bunches and σ_x, σ_y are the transverse dimensions of the beams at the colliding points. To maximize the luminosity, in both sides of each detector, the beams are tightly focused by a doublet of superconducting quadrupoles that focus the transverse beam dimensions to about 10 μm and 250 μm in the vertical and horizontal planes respectively.

In the LEP only the last phase of the electron and positron bunches acceleration is performed. Before to be injected in the LEP, bunches of electrons and positrons are accumulated and accelerated up to an energy of 20 GeV with a system made of four particle accelerators: the LEP injectors (Fig. 3.2).

The injectors consists of two linacs of 200 and 600 MeV where electrons and positrons are produced, accelerated and injected in the Electron-Positron Accumulator (EPA). The EPA accumulates electrons and positrons in bunches of approximatively 10^{10} particles and inject them in the CERN Proton Synchrotron (PS) operating as a 3.5 GeV e^+e^- synchrotron. Particles from the PS are then sent to the CERN Super Proton Synchrotron (SPS) where they are accelerated up to 20 GeV and transfered to the LEP collider where the bunches of electrons and positrons are brought up to the nominal energy. The number of bunch crossings per cycle has

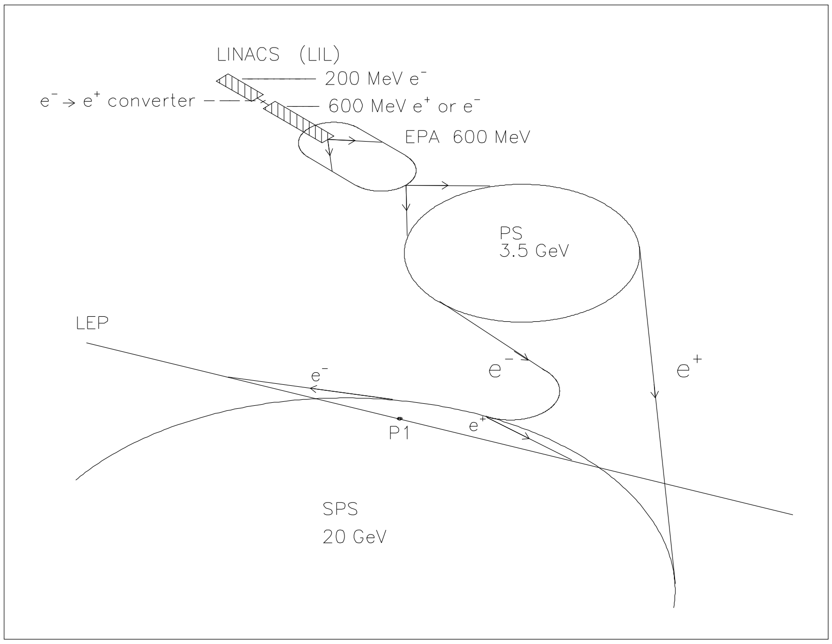

Figure 3.2: The LEP injection system.

eveloved with the constant improvements of LEP gonig from 4x4 to 8x8. In 1995 a major improvment has been done with 4x4 bunch crossing per cycle, each bunch being constituted by four bunches.

From the first beams, in 1989, to 1995 the LEP has worked at the energy of the Z^o peak. Since 1995, LEP2 phase has started. By adding superconducting RF cavities to the acceleration system, LEP was able to deliver higher energy beams enabling the observation of the process $e^+e^- \longrightarrow W^+W^-$.

3.2 The L3 Detector

The L3 [5] experiment is installed, 50 meters underground, at the interaction point P2. The detector is composed by successive layers of sub-detectors of cylindrical geometry housed in a 7800t octagonally shaped solenoid coil magnet (Fig. 3.3). The maximum magnetic field reached is relatively low (0.5T) but the volume has been maximized in order optimize the muon momentum resolution which improves only linearly with the field but quadratically with the track length as shown by the Glückstern formula:

$$\frac{\sigma_p}{p} \propto \frac{p \sin\theta}{0.3BL^2}$$

where p is the particle momentum, B the magnetic field and L the length of the track projected into the bending plane.

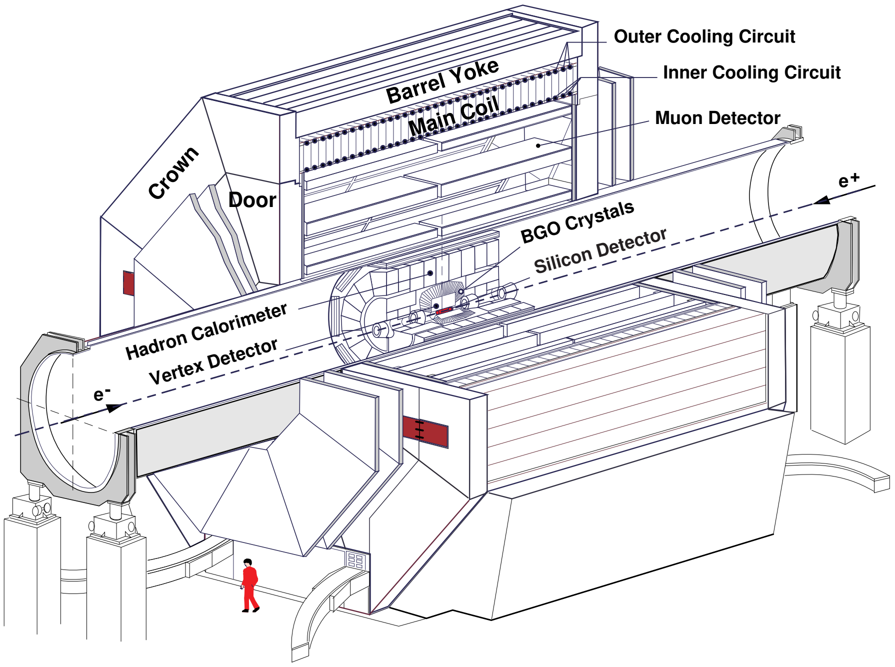

Figure 3.3: The L3 Detector.

A transverse view of the L3 detector is shown in Fig. 3.4. The detector is supported by a 32 m long and 4.45 diameter steel tube concentric with the LEP beam line and symmetric with respect to the interaction point. A feedback system is used to continuously align the support tube to the LEP beam. The muon spectrometer forms three high precision concentric drift chambers. They allow for a sagitta

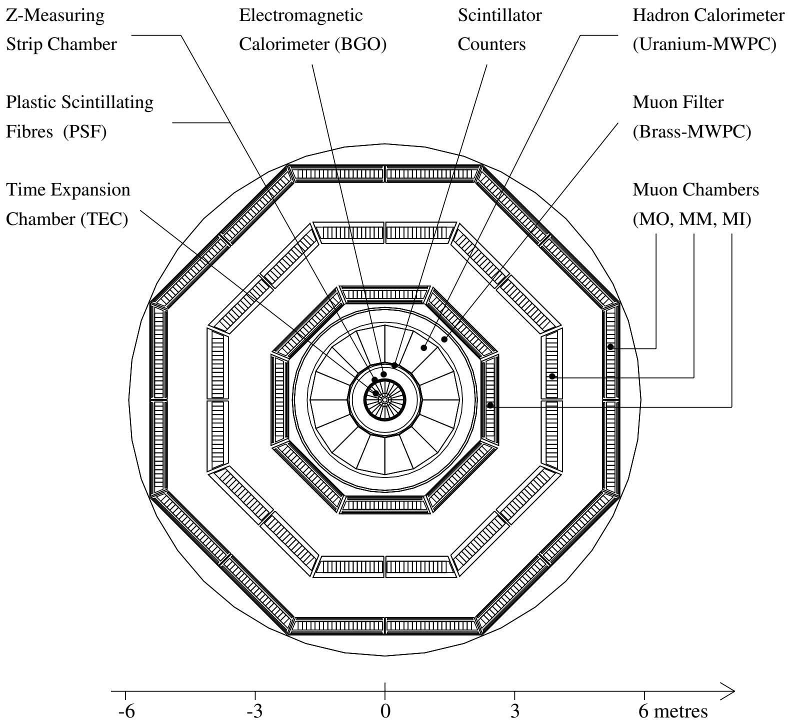

Figure 3.4: A transverse view of the L3 Detector.

measurement with a lever arm of $L = 2.9$ m. The inner detectors are located in the central section of the support tube. Going radially from the interaction point outwards, the inner detectors consist of:

- a central tracking detector;
- an Electromagnetic Calorimeter (EC) using large arrays of Bismuth Germanate (BGO) crystals arranged in a barrel and two end caps covering approximately 94% of the solid angle;
- a cylindric system of scintillator counters;

- a Hadronic Calorimeter (HCAL) using layers of depleted Uranium plates interspersed with proportional wire chambers. The HCAL has two parts: the barrel part and the forward-backward part. More than 99% of the full solid angle is covered by the HCAL.

To detect particles in the very forward regions, two additional detectors are used:

- the Luminosity monitors,
- the Active Lead Rings.

The coordinate system used in this thesis is shown in Fig. 3.5.

In the following sections we will describe the different sub-detectors of L3 with a particular emphasis on the elements used in the analysis presented in this thesis. In Appendix are discussed in more details systems to which we have apported a sizeable contribution.

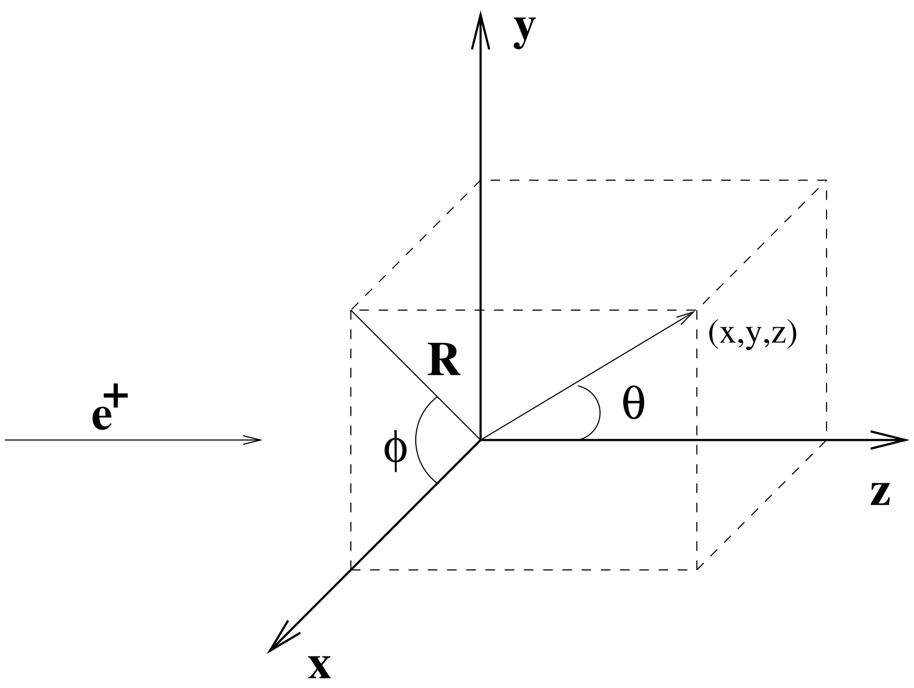

Figure 3.5: The Coordinate system of the L3 Detector.

3.3 The Central Tracking Detector

The compact design of the inner detector, which has to be contained inside the support tube, the low magnetic field and the needs of precise track measurement with a good vertex and momentum resolutions had driven the conception of the L3 tracking detector. It is composed by an inner Silicon Microvertex Detector (SMD) and by an outer drift chamber working in time expansion mode (TEC). The system is surrounded by two cylindrical proportional chambers with cathode strip readout: the Z-chambers. Moreover, in the forward-backward regions, where the TEC efficiency is limited by the small number of wires hit by the tracks, two layers of drift tubes have been inserted (FTC). The aim of the tracking detector can be summarized as follow:

- detection of charged particles;
- determination of the transverse momentum and sign of the charge for particles up to 50 GeV;
- impact point and direction reconstruction for charged particles at the entrance of the electromagnetic calorimeter;
- secondary vertices reconstruction for particles with lifetime greather than 10^{-13} s;
- determination of the track multiplicity originating from the interaction region at the trigger level and dE/dx measurement.

A longitudinal view of the tracking system is shown in Fig. 3.6.

3.3.1 The Silicon Microvertex Detector

The original L3 tracking system [5] did not include the use of a silicon detector. At the beginning of 1991, the radius of the LEP beam pipe at its four interaction points was reduced from 8.0 cm to 5.5 cm. The newly acquired space between the beam

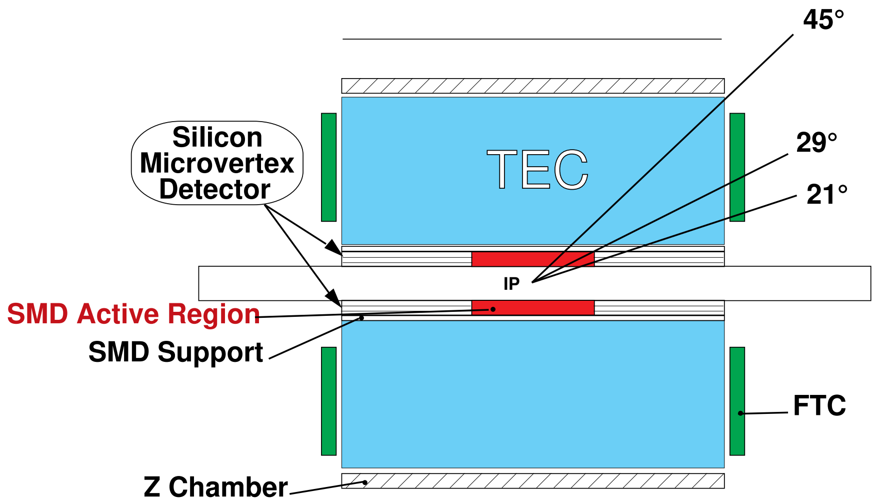

Figure 3.6: The L3 tracking detector.

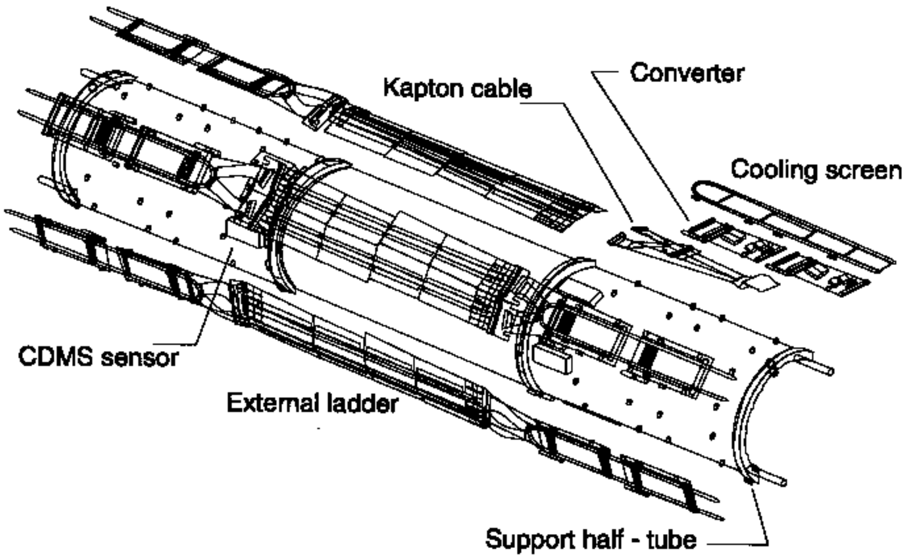

Figure 3.7: The L3 tracking detector.

pipe gave to L3 the possibility to install a silicon vertex detector. The installation was completed in 1993.

The SMD is built from 2 radial layers of double-sided silicon strip detectors [14, 15, 16, 17] providing $r - \phi$ and z coordinate measurement over the polar angle range $22^o < \theta < 158^o$ (Fig. 3.6) and over the full azimuth. The basic detector element of the SMD is a "ladder" which is built from two separate "half-ladders". The mechanical structure of the SMD [18] is shown in Fig. 3.7. The ladders are attached to a mechanical support at two mean radii: $r = 60.7$ mm and $r = 77.5$ mm (Fig. 3.8). The inner ladders are mounted with their axis parallel to the beam direction and crenellated with a 5% overlap to aid the alignment via the measure of tracks in the overlap region. To facilitate pattern recognition, the outer ladders are mounted so that their half-ladders are tilted by a stereo angle of 2^o with respect to the beam direction to facilitate pattern recognition.

The front end readout chip for the 73,000 SMD readout channels is based on a CMOS VLSI circuit, the SVX-H3 [19], originally developed for the CDF silicon strip tracker. Each half-ladder is readout by a set of six SVX-H3 for the $r - \phi$ and z sides, each SVX-H3 being able to handle 128 channels. The data transmission to a custom built VME-based data acquisition system (DRP V05) is performed via optical fibers. The optical communication allows to separate efficiently the electrical ground of the detector from the data acquisition ground.

The advantage of placing a tracking system with a resolution of $\simeq 10$ μm in the $r - \phi$ plane, close to the interaction point, is evident. The transverse momentum resolution and the impact parameter resolution have been significantly improved by SMD as shown in Fig. 3.9. This is an important advance for many topics at LEP2 like the W-pair production or the enhancement of b-quark tagging capability to aid a potential Higgs detection [20].

3.3.2 The Time Expansion Chamber

The limited space available for this detector, within the electromagnetic calorimeter, has determined its design. The total lever arm for the coordinate measurements in the

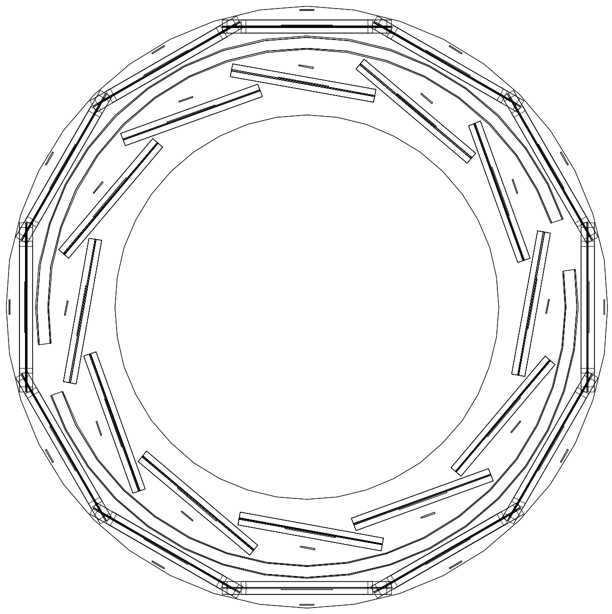

Figure 3.8: $r - \phi$ view of the L3 SMD detector.

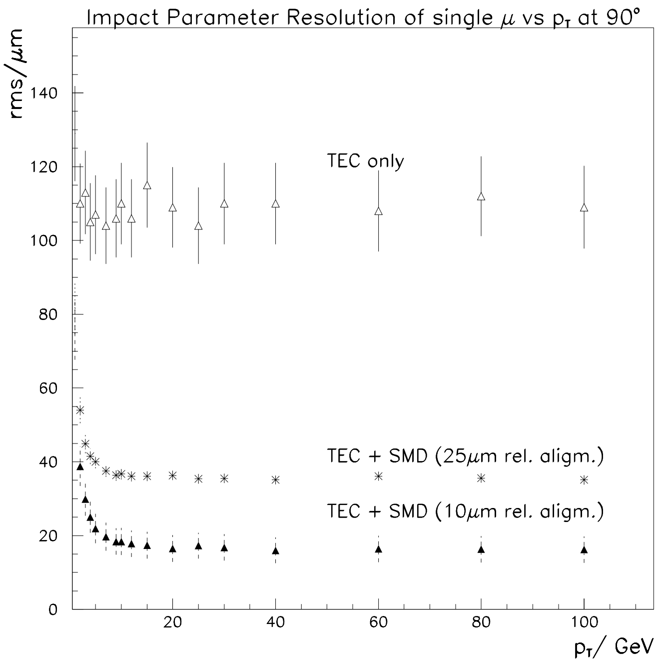

Figure 3.9: Impact parameter resolution of single μ vs p_T at 90^o.

chamber is 31.7 *cm* radially. With 50 coordinate measurements, a 50 μm resolution allows the charge identification of 50 GeVparticles with 95% confidence level. This is accomplished by two concentric cylindrical drift chambers on common end plates operated in time expansion mode, the inner TEC and the outer TEC [5, 21]. The radial extension of the inner TEC goes from 8.5 cm to 14.3 cm while the outer TEC extends up to 46.5 cm. Each inner sector covers an angle of 30^o in ϕ; the coverage in ϕ for a single outer sector is 15^o. A general view of the central track detector is shown in Fig. 3.10.

Following the TEC principle [22, 23], the high field amplification region at the sense wire plane is separated from the low field drift region by an additional grid wire plane. In the region close to the anode wire an high electric field allows for the multiplication of the incoming charges. In the drift region, the low drift speed (~ 6 μm/ns) allows a precise determination of the centroid of the time distribution of particles created by ionization. This allows to obtain a single wire accuracy of 56 μm for the inner TEC and 46 μm in the outer TEC.

The anode wire planes are arranged radially forming 12 inner and 24 outer sectors. The technical wire configuration in an orthogonal section of the TEC is shown in Fig. 3.11. Three different types of sensitive wires are used:

- The standard anode wires measure the drift time. They are connected to preamplifiers with decoupling capacitors of 100 pF.

- The Left-Right (LR) wires are groups of five grid wires on each side of the amplification region which are also read out (pic-up wires represented by a "∇" in Fig. 3.11). Comparing the induced signals, the left-right ambiguity for the corresponding standard anode can be resolved.

- The Charge Division wires (CD) are coupled with low impedance capacitors (1 nF) to the amplification electronics. They are used to determine the z coordinate. Collecting a signal on both extremities of those wires allow the measurement of a charge asymmetry. The z coordinate is then obtained by comparing the signals collected on both extremities of these wires (Q_+ and

Q_-) as follow [24, 25]:

$$z = \frac{Q_+ - Q_-}{Q_+ + Q_-} \times \frac{L_{eff}}{2}$$

where L_{eff} is the sensitive wire length (982 mm).

The inner sectors include six standard and two CD wires, while the outer sectors include 31 standard, 14 LR and 9 CD wires.

The TEC operates with 80% CO_2 and 20% iC_4H_{10} which has a negligible Lorentz angle and permits a low drift speed. A Plastic Scintillating Fibers (PSF) system is used to monitor the drift speed with an accuracy of 0,1%.

3.4 The Electromagnetic Calorimeter

The electromagnetic calorimeter consists of about 11000 crystals of bismuth germanate ($Bi_4Ge_3O_{12}$ hereafter called BGO) as both the showering and detecting medium. The BGO is of particular interest for an electromagnetic calorimeter [26] because of his short radiation length and his large nuclear interaction length. The comparison of the physical properties between the BGO and a scintillator of common use, the NaI(Tl), [5, 27] are shown in Tab. 3.1. All the BGO crystals point to the interaction region; each crystal is a 24 cm long truncated pyramid with a section of 2×2 cm^2 at the inner and 3×3 cm^2 at the outer end. They are arranged in two half barrels surrounding the central tracking chamber giving a polar angle coverage of $| \cos\theta | \leq 0.743$ and by two end caps, with track chambers (FTC) in front (see Fig. 3.13), giving a polar angular coverage of $0.978 \leq | \cos\theta | \leq 0.788$. To achieve the best solid angle coverage the structural material is confined to thin walls around the cells, each crystal is pressed from its back onto the front of its cell by a spring-loaded holding device. The thickness of the cellular structure has been minimized, in the limit of technical feasibility, each crystal being separated from its neighbors by a wall of 100 μm. To detect the BGO scintillation light, 1,5 cm^2 Hamamatsu S2662 photodiodes are used. Each crystal has two photodiodes glued in its rear face (Fig. 3.12). Since they have a unity gain, the signal from the photodiode being about

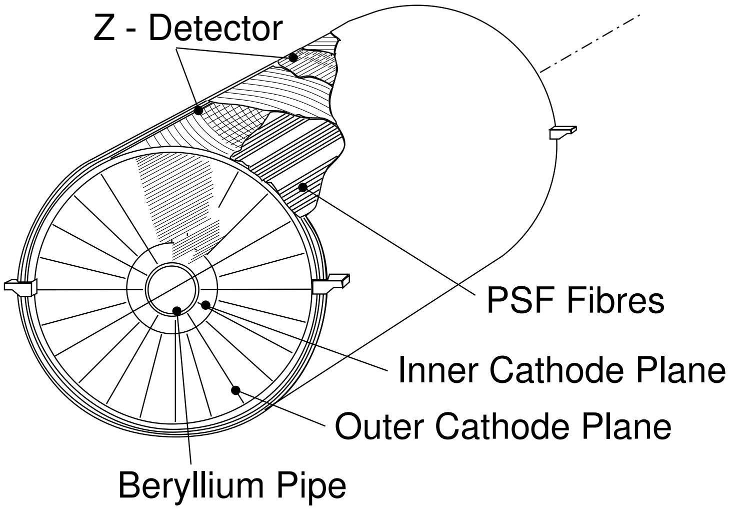

Figure 3.10: A perspective view of the Time Expansion Chamber.

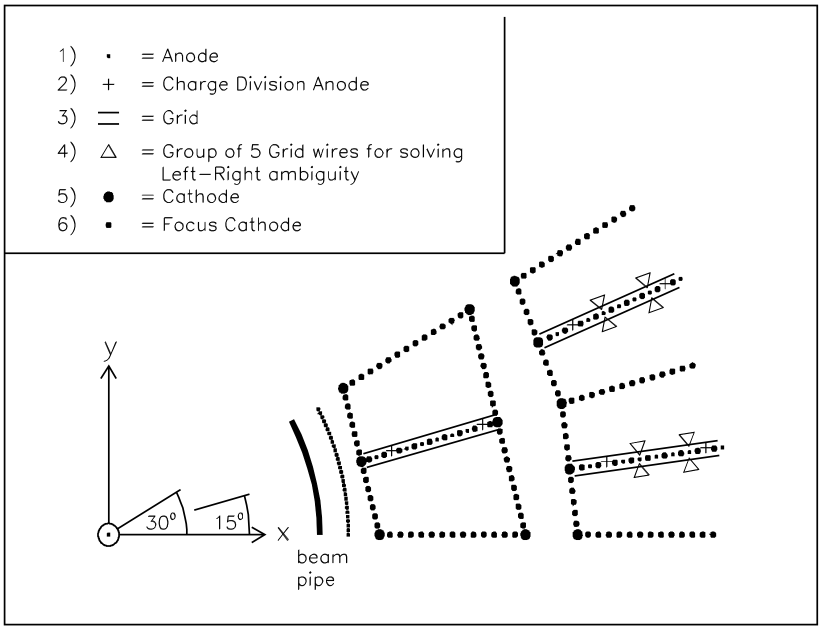

Figure 3.11: The wire configuration in one inner TEC sector and part of two outer sectors.

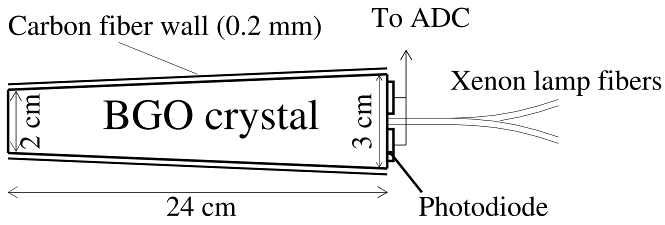

Figure 3.12: Leteral view of a BGO crystal.

0,2 fC/MeV, a charge sensitive preamplifier [28] is used. It is mounted directly behind the crystal. An important characteristic of the photodiode-preamplifier combination is the rms random noise level which is less than 1000 electrons.

The precision on energy measurement, for an electromagnetic shower in the barrel region, can be parametrized by [29]:

$$\frac{\sigma(E)}{E} = \sqrt{\left(\frac{a}{\sqrt{E}} + b\right)^2 + d^2 + \frac{c^2}{E^2}}$$

where E is expressed in GeV and:

$$\begin{aligned} a &= 1.54 \times 10^2 GeV^{1/2} \\ b &= 0.38 \times 10^{-2} \\ c &= 0.25 \pm 0.15 \times 10^{-2} \\ d &= 1.18 \pm 0.11 \times 10^{-2}. \end{aligned}$$

An energy resolution of 1.4% at 45.6 GeVhas been achieved and maintained by using a xenon monitoring system developed by the University of Geneva [30, 31, 32]. Light pulses are injected into each crystal and allows for a relative calibration of

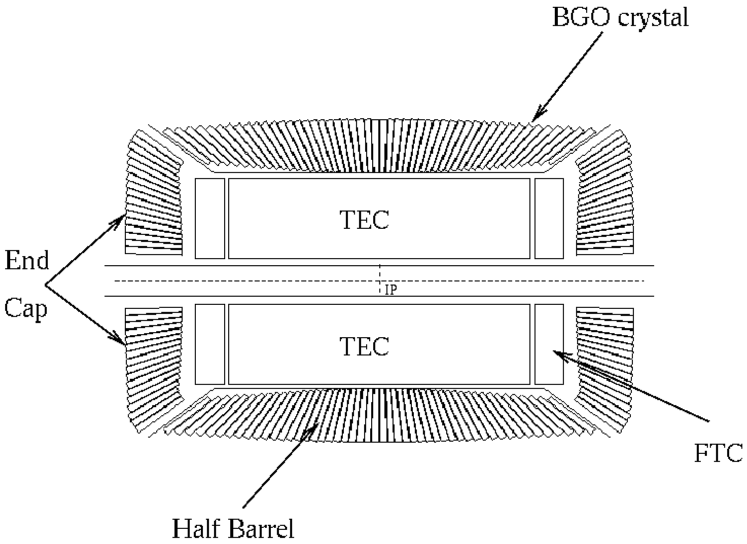

Figure 3.13: Longitudinal cut throught the electromagnetic calorimeter.

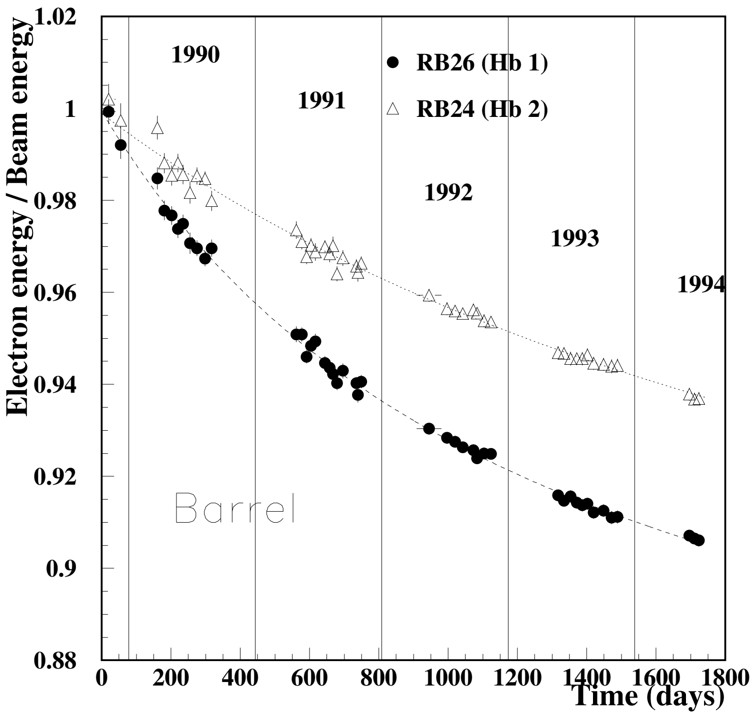

Figure 3.14: Time Evolution of the light output of the BGO calorimeter for 45.6 GeVelectrons. A similar curve is observed in the end caps.

Properties	BGO	NaI(Tl)
Density [g/cm^3]	7.13	3.67
Radiation length [cm]	1.12	2.59
Moliere radius [cm]	2.3	4.4
dE/dx [MeV/cm]	9	4.8
Interaction length [cm]	22	41
Refractive index	2.15	1.85
Maximum emission wavelength [nm]	480	410
Temperature coefficient of light yield [$\%/^oC$]	-1.55	0.22
Luminosity lifetime [μs]	0.3	0.23
Hygroscopic sensitivity	no	yes

Table 3.1: BGO and NaI(Tl) properties.

all crystals in a geometrical region illuminated by the same lamp. The absolute calibration is then performed using Bhabha events ($e^+e^- \longrightarrow e^+e^-$). An aging effect as been observed from the monitoring of the light output of the crystals induced by Bhabha electrons (Fig. 3.14). This effect can be parametrized by the following expression [29]:

$$\frac{\text{Electron energy}}{\text{Beam energy}} = \frac{a'}{t + t_o} + c$$

with:

$$a', c, t_o = \text{parameters determined from the experimental points.}$$

The parameter c is the asymthotic limit of the time evolution; its value is about 85% for the barrel and 70% for the end caps.

3.5 The Scintillation Counters

The scintillation counters [33] are located between the electromagnetic and the hadronic calorimeter (Fig. 3.16). Their time resolution < 1 ns allows to distinguish di-muon events from cosmic muons. Since they are 875 mm away from the beam, the time-of-flight difference between two opposite counters will be zero for a di-muon event and 5.8 ns for cosmic muons. The scintillators are 2.9 m long and 1 cm thick plates of Bicron BC-412 plastic scintillators; the angular coverage is $|\cos\theta| < 0,83$ for the polar angle and 93% of 2π for the azimuthal angle. To enhance the time resolution, time slewing corrections can be applied by digitizing the charge of the photomultiplier pulse. A time resolution of $\simeq 0.5$ ns is obtained as shown in Fig. 3.15

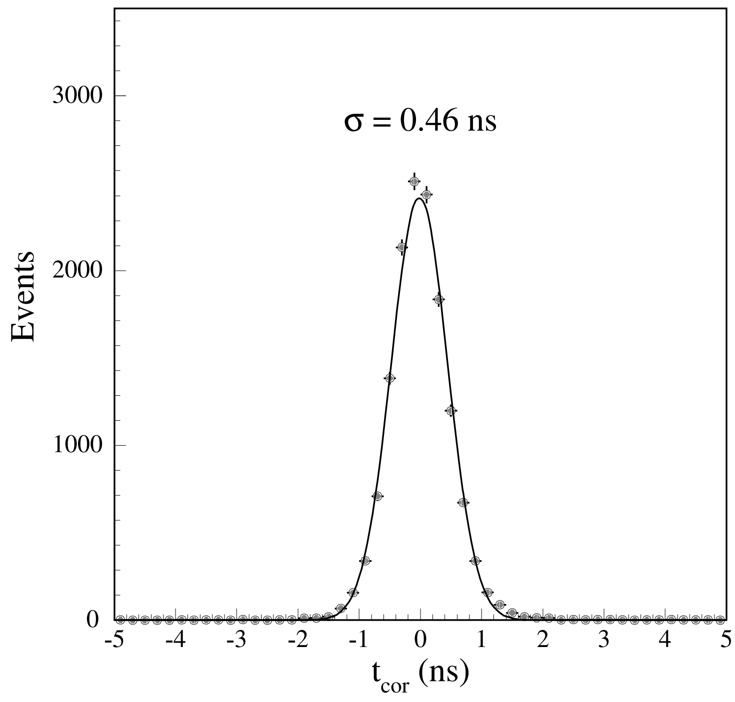

Figure 3.15: Time resolution of the scintillation counters.

3.6 The Hadron Calorimeter

Energy and containment of showers initiated by strongly interacting particles are measured by the Hadron CALorimeter (HCAL) surrounding the electromagnetic calorimeter. It is a gas sampling calorimeter using towers of depleted Uranium plates as an absorber interspersed with proportional wire chambers. The Uranium provides a constant in situ source of gammas for calibrations but it also adds to the per channel noise during data taking. For a gate width of 300 ns, the Uranium noise is equivalent to 2 MeV r.m.s equivalent hadron energy deposition per channel. The passage of MeV neutrons from nuclear spallation, initiated by fast hadrons or by fission processes in the Uranium, usually produces large ionization deposits which in turn produce large high energy tails in the hadron energy distribution which can worsen the energy distribution. To minimize this problem, the proportional chambers are filled with a 80% Ar and 20% CO_2 giving an $e/\pi \simeq 1.25$ and an energy resolution of $0.55/\sqrt{E} + 0.05$ (E measured in GeV)[34]. Some general features of the HCAL [34, 35] are summarized in Tab 3.2.

Gas	80% Ar/20% CO_2
Gain	$\sim 10^4$
Energy Deposit	$\sim$ 25 $MeV/m.i.p.$
Readout	22000 channels
Energy Resolution	13% at 45 GeV
Spatial Resolution (with muons)	$\sigma_\theta(\mu) = 28$ mrad $\sigma_\phi(\mu) = 25$ mrad $\sigma_z(\mu) = 8$ mm

Table 3.2: Hadronic Calorimeter Properties.

The HCAL is composed by a barrel and two end caps and covers 99.5% of the full solid angle (Fig. 3.16). The barrel has a modular structure consisting of 9 rings of 16 modules each. Two types of modules are used: the three internals rings are made up of 60 layers of multiwire proportional chambers interspersed with 58 layers of Uranium; the six outer layers are made up of 53 layers of chambers and 51 layers of Uranium. To limit the number of channels to be read out still conserving a good granularity, the wires in each module are grouped to form readout towers. In the ϕ projection the towers point to the beam axis with a constant angular interval and achieved granularity is: $\Delta\theta = 2.5^o$ and $\Delta\phi = 3.5^o$. The end caps have a similar

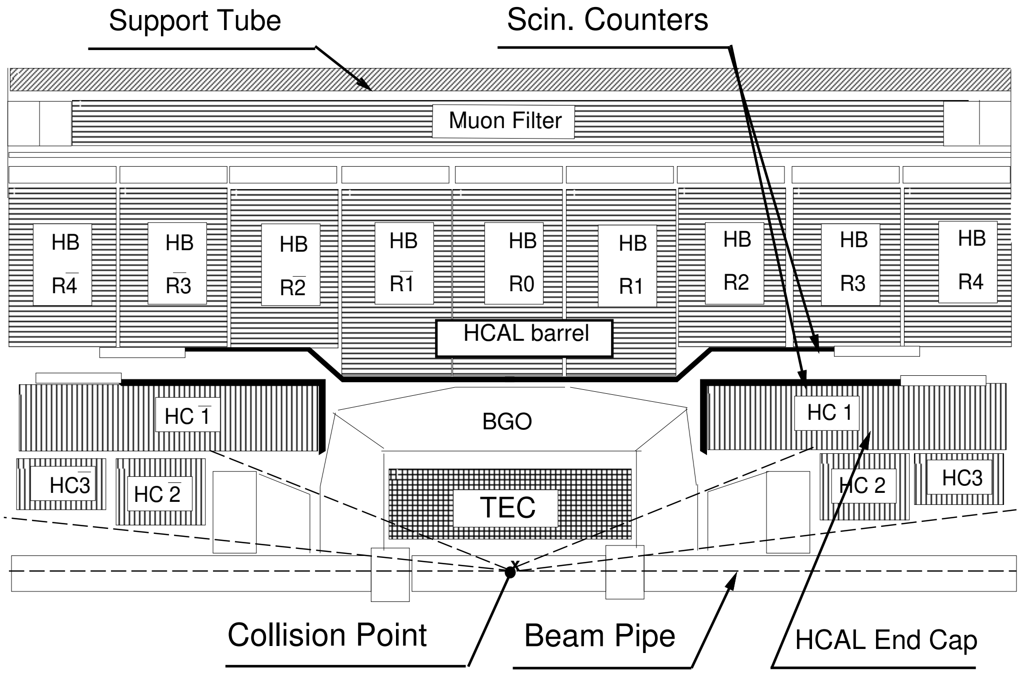

Figure 3.16: A longitudinal section of the hadron calorimeter surrounding the electromagnetic calorimeter (BGO) and the vertex chamber. The position of the scintillation counters is also shown.

structure; they are subdivided in three rings: an outer ring (HC1) and two inner rings (HC2 and HC3). Each ring is split vertically into half-rings, resulting in a total of 12 separate modules. The mechanical conception of the hadronic calorimeter end caps is such to allow their fast withdrawal providing access to the other L3 central detectors.

3.6.1 The Muon Filter

To prevents muons originating from π decays to enter in the muon spectrometer, 1.03 absorption length has been interleaved in the space between the hadronic calorimeter and the inside wall of the support tube (Fig. 3.16). The muon filter consists of eight identical octants, each made of six 1-cm absorber plates (65% $Cu + 35\%$ Zn), interleaved with five layers of proportional chambers and followed by five 1.5 cm thick absorber plates matching the circular shape of the support tube.

3.7 The Muon Spectrometer

The momentum of high energy muons is determined by measuring the sagitta of the tracks. The muon spectrometer [36] occupy a volume of $\sim$ 1000 m^3 and has an octagonal structure (Fig. 3.4). Each octant consists of a mechanical structure

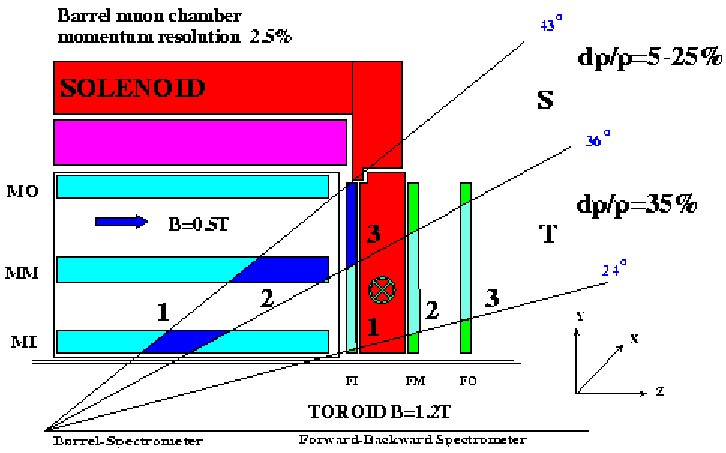

Figure 3.17: Side view of the muon spectrometer.

supporting three layers of drift chambers: the inner (MI), the middle (MM) and the outer (MO). This structure, referred as "muon barrel", covers, on both sides of the interaction point (Fig. 3.17):

- the region between 90^o and 44^o in θ with three detection layers,
- the region between 44^o and 36^o in θ with two detection layers.

The muon track in the $r - \phi$ plane is measured by 24 wires in the layer MM, and by 16 wires in the MI and MO layers with a resolution of 50 μm; they allow for a sagitta measurement with a total lever arm of 2.9 m. The z coordinate is measured with a precision of 500 μm by dedicated chambers located around MI and MO. The precision of 2.5% on the muon momentum measurement (Fig. 3.18) is obtained by measuring the sagitta of the track with an accuracy better than 88%.

Since February 1995, the L3 experiment is fully equipped with a forward-backward muon spectrometer in order to improve the muon momentum resolution between 44^o and 36^o, and to allow muon momentum measurement down to 24^o. The forward-backward spectrometer consists of 96 drift chambers, divided into 16 sectors with 3 layers each on both sides of the detector [37].

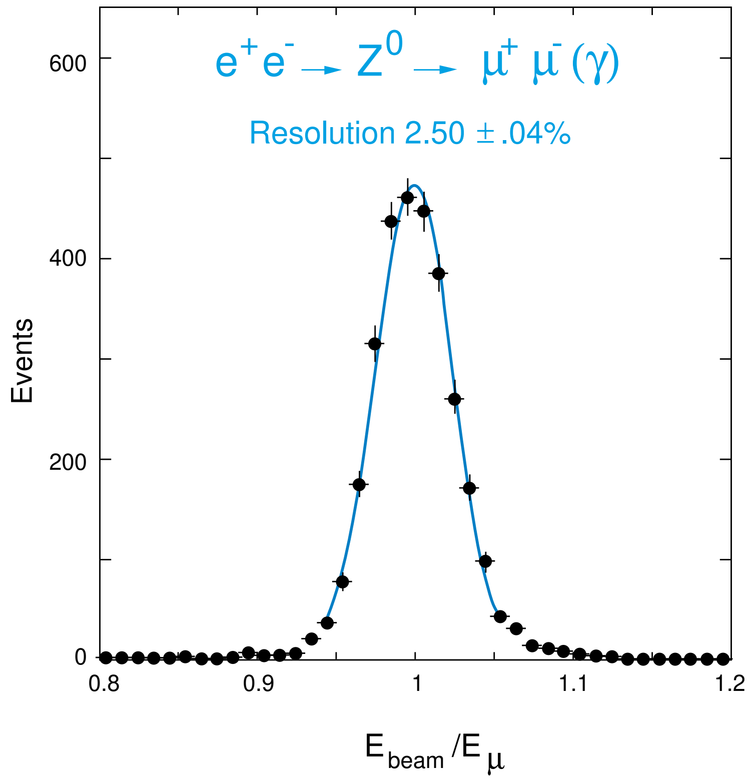

Figure 3.18: Muon momentum resolution.

3.8 The Forward-Backward Detectors

To maximize the solid angle coverage and to allow for a reliable luminosity estimations via the measurement of the rate of Bhabha events, the L3 detector is equipped with a system of low polar angle calorimeters. The location of the forward-backward detectors is shown in Fig. 3.19

3.8.1 The Luminosity Monitors

The principal role of the Luminosity Monitors (LUMI) is to provide reliable luminosity measurements by measuring the rate of Bhabha events. It consists of a charged particle tracking device followed by an highly segmented BGO array. The system covers the following polar angle regions: $1.4^o \leq \theta \leq 3.9^o$ and $176.1^o \leq \theta \leq 178.6^o$.

The BGO calorimeter consists of two detectors located symmetrically in each side of the interaction point at a distance of 2.73 m. Each detector is cylindrical symmetric and contains 305 BGO crystals parallel to the beam axis as shown in Fig. 3.20 [38]. Crystals cover 15 mm radially and are arranged in eight rings. Azimuthally the detector is segmented into 16 sectors, each covering an angle of 22.4^o. The accuracy on the luminosity measurement obtained with the BGO luminosity calorimeter is 0.6%.

The particle tracking device, installed in 1993, is a silicon strip detector (SLUM). There are three layers in each side: two layers of strips concentric with the beam axis to measure the θ angle of incoming particles, and one layer of strips perpendicular to the beam axis to measure the angle ϕ. Since the selection of Bhabha events is improved by the fine granularity of this detector; by coupling the SLUM measurements with those of the BGO luminosity calorimeter, the absolute luminosity can be measured with an experimental precision of 0.05%.

The LUMI as been extensively used in the analysis presented in this thesis (Chap. 6) to select scattered beam electrons (tag) in two-photon events (Chap. 4).

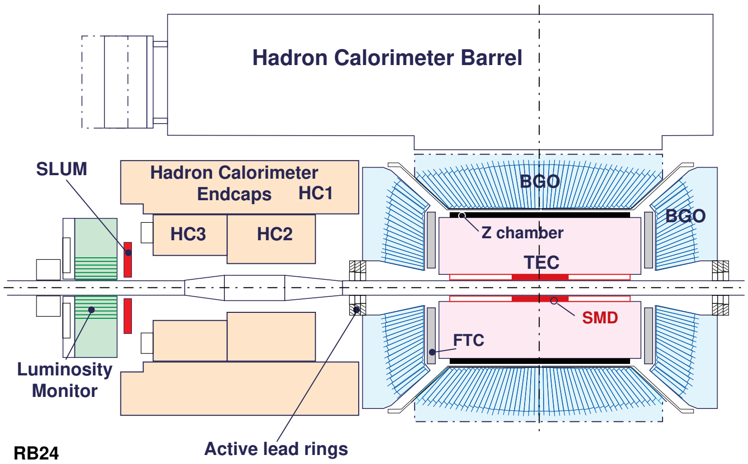

Figure 3.19: Side view of the central region of the L3 experiment, showing the location of the luminosity monitors (Luminosity BGO + SLUM) and the Active Lead Rings. Only one side is represented.

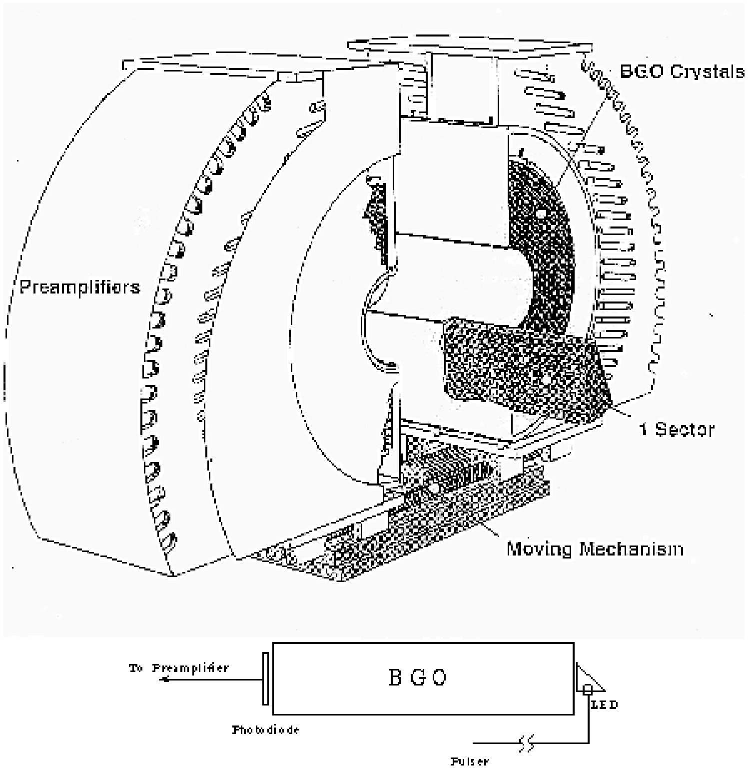

Figure 3.20: Isometric view of the BGO luminosity calorimeter. The location of crystals, preamplifiers and the moving mechanism are shown.

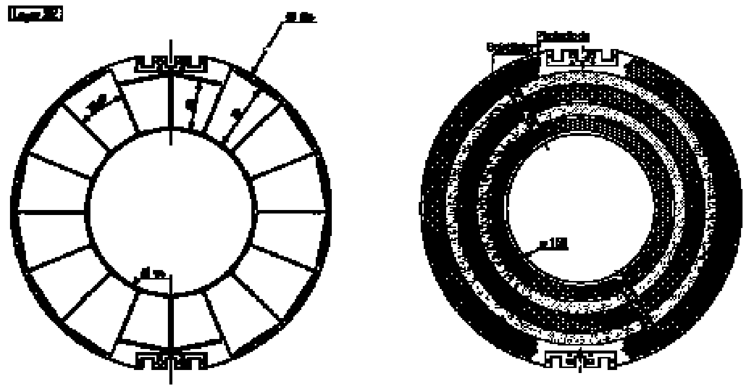

Figure 3.21: $x - y$ views of ALR scintillator layers. Shown on the left is a layer of ϕ-scintillator while a layer of θ-scintillators is shown on the right.

3.8.2 The Active Lead Rings

The Active Lead Rings detector (ALR) covers the forward and backward region between 4^o and 9^o [39]. Originally the ALR were installed to protect the inner tracking chamber from stray background particles. Instrumenting the lead material with plastic scintillators allowed to use them as vetoes, improving on the hermeticity of the whole L3 detector. The elements consist of 3 scintillator layers 10 mm thick placed behind 18.5 mm (3.3 X_o) thick lead converters [40]. The scintillators, which have trapezoidal shape (ϕ-scintillators) subtends 22.5^o in ϕ, and since the successive layers are tilted by 1/3 of the width of the scintillator, the effective ϕ segmentation is 7.5^o. The read out is performed with photodiodes of dimensions 10x20 mm^2 placed at the outer edge of the scintillators. To use this detector also as an electron tagger, thus extending the Q^2 range (Chap. 4) for the measurement of the photon structure function, a segmentation in polar angle θ has been implemented in 1995 by adding semi-circular shaped scintillators (θ-scintillators) read at their both ends by photodiodes. An $x - y$ view of the scintillator layers is shown in Fig. 3.21.

3.9 The L3 Trigger and Data Acquisition

At each beam crossing, a trigger system decides whether an e^+e^- interaction took place and if so, whether the event should be recorded. To perform this function three levels (level-1,level-2 and level-3) of increasing complexity triggers are operational reducing the 45 KHz (90 KHz), 4x4 (8x8) LEP bunch mode, beam crossing rate to a few Hz tape writing rate. All the detectors are read by the front end electronics for each beam crossing. In addition to the main data, each detector provides a coarser and less accurate trigger data available in digitized form within few μs. All the trigger data streams, originated from the front end electronics of the detectors, are analyzed by different dedicated systems. At the level-1 trigger the decision of either keep or abandon the event is made by a logic "OR" between the different subtriggers, and should be made within 22.2 (11.1) μs. In case of a negative decision the front end electronics is cleared before the next beam crossing so there is no level-1 contribution to the dead time. For events selected by the level-1 trigger, the detector data are digitised and stored within 500 μs in multievent buffers and the system is readied for the next beam crossing.

After a level-1 trigger, the trigger data are further analyzed by the level-2 trigger composed by a set of programmable processors which reject background events accepted by the level-1 trigger. A rejection rate of 10 is performed at this level.

Events which have been selected by the first two trigger levels, are finally analyzed by the level-3 trigger in charge of making the final selection based on the online reconstruction of the complete set of digitised data from all the detector components.

3.9.1 The Level-1 Trigger

The level-1 trigger is simply the logical "OR" of trigger conditions from different sources:

The Energy Trigger

The energy trigger [41, 42] processes the information given by the electromagnetic and hadronic calorimeters and by the luminosity monitors. The logical "OR" of the following energy sub-triggers is used by the level-1 trigger:

- **Total Energy Trigger:** Based on a total energy deposition in the electromagnetic and hadronic calorimeter. A trigger is given if the total energy is above a predefined threshold which depends on the ratio of electromagnetic to hadronic energy.
- **Cluster Trigger:** A cluster is a localized deposit of energy observed in different detector layers at the same θ and ϕ coordinates. The energy threshold depends on the calorimeters involved. A trigger is given if at least one cluster is found. The TEC and scintillation counters information helps to lower the thresholds.
- **Single Photon:** A single photon trigger is given if a BGO cluster accounting for more than 80% of the total electromagnetic energy of the event is found. No track should be detected in coincidence with the cluster.
- **Hit Counting Trigger:** A trigger is given if there is at least two cells with more than 5 GeV.
- **The Luminosity Trigger:** Two high energy hits with strong back to back correlation in the luminosity monitors are requested.
- **Single Tag Trigger** An energy deposit greater than 30 Gev is requested in the luminosity monitors. A prescaling of 40 is set for this trigger if there are no tracks detected by the TEC otherwise a prescaling of 1 is used.

The ALR Trigger

This trigger, developed by the University of Geneva [43, 44], is operational since 1995 and has been implemented to enlarge the low angle tagging capabilities of the L3 detector at LEP2. This trigger will be discussed in more details in Appendix A. It provides the logic "OR" of three subtriggers:

- **Prescaled Single Tag Trigger:** At least one high energy (> 20 GeV) deposit in the ALR.
- **Bhabha Trigger:** An high energy deposit (> 20 GeV) in both sides of the ALR detector.
- **Gamma-Gamma Trigger:** An high energy deposit (> 15 GeV) in the ALR detector and at least one track detected in the TEC.

Events selected by the ALR trigger are directly transferred to the L3 DAQ.

The TEC Trigger

The charged particle trigger [45, 46, 47] search for tracks pointing to the interaction point in the $r-\phi$ projection (i.e. in the plane orthogonal to the beam axis). Due to the beam background conditions, only the outer TEC sectors are used.

The Scintillator Trigger

The scintillator trigger is based on the signal of 30 barrel and 32 end cap scintillation counters. It is used for high multiplicity events and to suppress cosmic background from the muon trigger triggered sample.

The Muon Trigger

At least one particle in the muon spectrometer is required. Since the cosmic muons can contribute with a rate of 10 Hz to the trigger rate, the muon trigger [48] ask also for a coincidence with the scintillator trigger.

3.9.2 The Level-2 Trigger

The main purpose of the level-2 trigger [49] is to reduce event rate by:

- correlating the detection of clustered energy in the BGO and in the hadron calorimeter
- computing the transverse and longitudinal imbalance of the clustered energy,
- recognizing the vertex along the beam axis by using the charge division wires of the TEC.

3.9.3 The Level-3 Trigger

Unlike the level-1 and level-2 triggers, for which only data with coarse granularity and lower resolution are available, the level-3 trigger has access to the complete digitized data. FORTRAN algorithms select good events on the basis of:

- Correlation of the energy deposited in the BGO and in the hadron calorimeter.
- The reconstruction of muon tracks in the Z chambers.
- Reconstruction of the vertex in the TEC.

In case of a positive level-3 decision, the data are transferred to the main data acquisition computer for tape writing.

3.9.4 The Data Acquisition

The data acquisition uses mostly FASTBUS. The system [5] includes ample buffering capacity to allow asynchronous operation without contributing to the dead time. The digitized data for each detector component are stored in several event memories situated in the detector FASTBUS crates. These data are then merged together, for each event, by the combination of three FASTBUS modules: a general purpose master (GPM), a block mover (BM) and a dual slaver memory (DSM). The event is then sent to a central crate connected to a CERN Host Interface (CHI) which insure the buffering into the online computer, a VAX 8800. In the last step the event is transferred, in a raw data format, from the VAX memory into a tape. To be used for the physics analysis, each event is reconstructed across the whole L3 detector using the REL3 program (Fig. 3.22). At this stage all the calibration constants are applied.

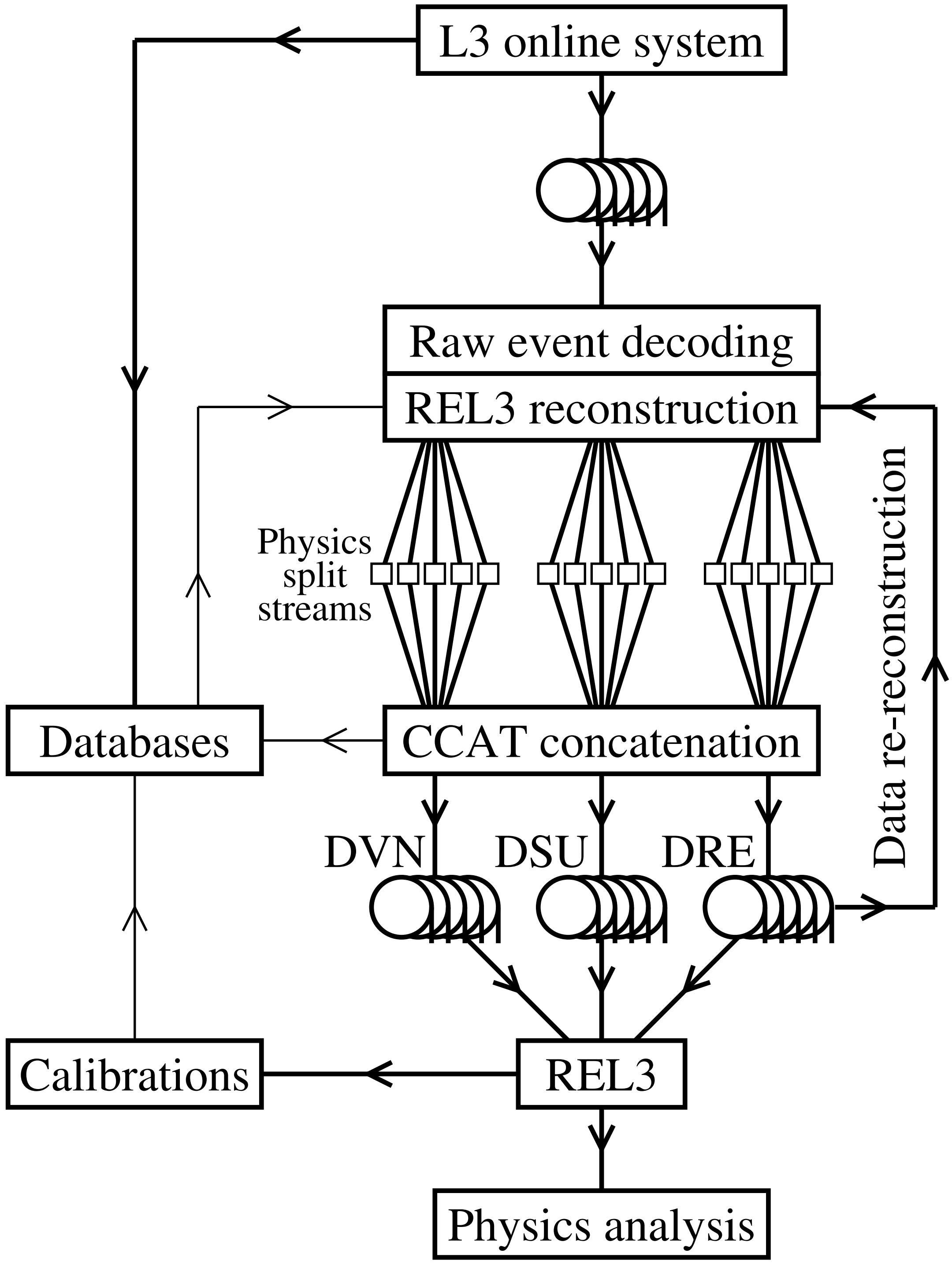

Figure 3.22: Schema of the reconstruction procedure. Reconstructed data are selected and split in different physics streams. The final product ready for the physics analysis is produced in three different formats containing different informations for the analysis.

"denique nil sciri siquis putat, id quoque nescit an sciri possit, quoniam nil scire fatetur."
Lucrezio, De Rerum Natura, IV 466.

Chapter 4

The Two Photon Physics

This chapter does not have the ambition to give a general overview of the two-photon physics. The theoretical framework recquired for the analysis presented in this thesis is briefly reviewed. A complete review of two photon physics can be found in [10, 11, 50, 51].

4.1 Introduction

Photon-photon scattering is a direct consequence of the quantum formulation of electrodynamics. The classical formulation of Maxwell equations is linear in the electromagnetic field and thus cannot lead to any scattering between light waves. In quantum mechanics, however, following the uncertainty principle, a photon of energy E_γ can fluctuate into states of charged particle pairs. The lifetime Δt of this intermediate state is directly related to the uncertainty principle and is found to be:

$$\Delta t \simeq \frac{2E_\gamma}{m^2_{pair}}$$

where m_{pair} is the mass of the intermediate state. For high energy photons, Δt becomes large enough to allow photon-photon scattering via the interaction of intermediate particles.

In 1935 Euler and Kokel [52] have computed the cross-section for $\gamma\gamma$ elastic scattering described by the box diagram shown in Fig. 4.1. For photons of energy $E_\gamma \geq m_e$, inelastic channels (e.g. Fig. 4.2) becomes observable.

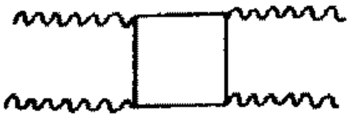

Figure 4.1: Box diagram for elastic $\gamma\gamma$ scattering.

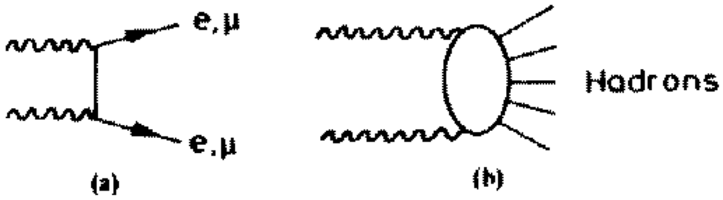

Figure 4.2: Inelastic two-photon reactions: a) $\gamma\gamma \longrightarrow e, \mu$, b) $\gamma\gamma \longrightarrow$ *hadrons*.

Indirect evidences of inelastic light-by-light scattering involving only real photons have been obtained from γ-ray astronomy. For visible light, photons carry an energy of a few eV, so the $\gamma\gamma$ elastic cross-section is only of the order of 10^{-30} nb [53]. Nevertheless, at any point between galaxies in the universe, one encounters a field of photons ranging in energy from 10^{-12} eV to at least 10^{11} eV and possibly 10^{20} eV (which is the upper end of the cosmic ray spectrum observed at earth) [54]. Since the cross-section of pair-production by inelastic two-photon scattering increases with the center-of-mass energy, high energy γ-rays, propagating over cosmological distances, suffer pair-producing reactions with photons from the extragalactic background radiation. This mechanism was recently invoked to explain why many EGRET blazars are not seen at TeV energies by ground-based instruments [55]. In this context, it is interesting to mention that only very recently the first laboratory evidence for inelastic light-by-light scattering involving only real photons has been obtained at the Final Focus Test Beam at SLAC [56]

Despite the abundance of photons in our Universe, the direct observation of two-photon interactions has needed the advent of high energy accelerators. Since it is very difficult to built high energy photon beams, two-photon reactions have been studied by observing the interactions of virtual photons (off-shell) emitted by high energy particles. The first clear observation of a two-photon process was made by Anderson in 1932 at the time of the discovery of the positron [57]. In 1934 Landau and Lifshitz [58] performed the first cross-section calculation for the complete two-photon reaction: $e^+e^- \longrightarrow e^+e^-e^+e^-$. However, apart many Primakov effect experiments [59], little progress has been done in experimental two-photon physics until the beginning of the sixties. Then the first e^+e^- colliders (Stanford, VEPPII, ACO) were designed and built. Unfortunately at that time the delivered luminosity was too low and the first relevant results of particle pair production have been obtained only ten years later. The first observation of electron-pair production has been made in 1971 at VEPPII by V.A. Bolakin and collaborators [60] and followed, in 1974, by the di-muon production with ADONE at Frascati by G. Barbiellini and Collaborators [61].

Since then, a number of e^+e^- colliders, such as PEP, PETRA, SPEAR, TRISTAN and finally LEP, have been built with higher energies and luminosities producing a wealth of data. Detectors at e^+e^- colliders are well suited for investigating photon-photon collisions. Due to the growth of the photon emission probability with the beam energy, e^+e^- colliders can be considered as a continuous energy $\gamma\gamma$ collider, and the cross-section for the two-photon process is much higher at LEP than in any previous electron-positron storage ring.

With the growing importance of electron-positron experiments, much attention has been focussed on reactions with cross-sections which do not decrease with increasing energy and thus exceed all the other cross-sections studied in high energy colliding beams (Fig. 4.3). Deepening the experimental and theoretical knowledge of $\gamma\gamma$ processes, as well as being of considerable interest in its own right, is of capital importance to make reliable estimates of the background provided by these high cross-section processes to new physics expected at LEP2 [62].

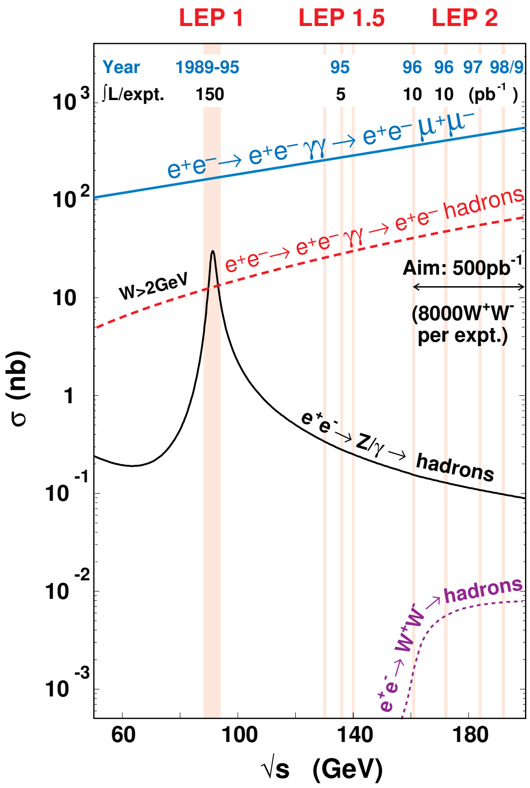

Figure 4.3: The cross-section of various e^+e^- processes as a function of the LEP collider center of mass energy.

4.2 The Two-Photon Physics at LEP

One of the dominant processes at LEP1 (indeed the dominant one at LEP2 as shown in Fig. 4.3) is: $e^+e^- \longrightarrow e^+e^-X$ where X is the system produced by the two-photon scattering. In effect, for quasi-real (i.e. close to the *on mass shell* condition) photon-photon collisions, the cross-section grows as $\ln s^3$, where s is the square of the center of mass energy of the incoming e^+e^- pair, whereas for annihilation the cross-section decreases like s^{-1}.

Two main physics domains in the study of $\gamma\gamma$ physics may be distinguished:

the "traditional" study of resonance formation and the study of two-body reactions. For the former, we will only mention that heavy resonances in the $C = +1$ state (e.g. η_c [63], η' [64], χ_c [65]), which are not directly observable in e^+e^- collisions, can be easily produced and studied in a clean environment (for more details see e.g. [10, 11]). In the case of two-body reactions, when one of the outgoing electrons is tagged, it is possible to probe the target photon at short distances. At high energies photon-hadron and photon-photon interactions are dominated by quantum fluctuations of the photons into fermion-antifermion pairs and into vector mesons which have the same spin-parity as the photon. This is called the photon structure [66]. Electron-positron collisions at LEP and positron-proton collisions at HERA are an ideal laboratory for studying photon structure in the interactions of quasi-real and virtual photons [66]. For the study of the structure of the photon, i.e. its quark and gluon content, LEP is the analogue to ep and pp colliders for the study of the proton structure. Thanks to the energy spectrum and to the high luminosity provided by LEP it is possible to undertake precision phenomenology in $\gamma\gamma$ physics and obtain quantitative tests of perturbative QCD. Deep inelastic two-photon interaction can be viewed as the interaction of the probe photon with the constituents of the target photon, coupling to a $q\overline{q}$ bound state (hadron-like part described by the Vector meson Dominance Model VDM [67, 68]) or splitting into a free $q\overline{q}$ state (point-like part described by the Quark Parton Model QPM [69, 70]). In the hadron-like process, the photon can fluctuate in a vector meson (ρ, ω, ϕ, ...) and the process looks like deep-inelastic electron-hadron scattering. The description of such a process is non-perturbative. On the other hand, when a target photon splits into quarks with a large transverse momentum with respect to the photon-photon axis, a perturbative calculation is applicable. Thus exclusive hadron-pair production allow to probe the interplay between perturbative short-distance and non-perturbative large-distance QCD mechanisms [68, 11]. Varying the virtuality (defined by the tagged electron) of the incoming photon, helps to better constrain the non-perturbative component of the photon and to understand the transition from a non-perturbative to a perturbative regime in QCD. The study of the structure functions of the photons helps to analyze the quark-gluon content of the photon.

A major problem using e^+e^- colliders as $\gamma\gamma$ colliders, arises from the fact that the initial energy is not fixed which turn out to be a major nuisance in the study of deep-inelastic structure function of the photon. To fully exploit the increasing statistic and kinematical coverage provided by LEP, and to approach the experimental accuracy of electron-hadron structure function studies, improved techniques to reduce systematic uncertainties are needed. This can be done e.g. by studying $e^+e^- \to e^+e^-\gamma\gamma \to e^+e^-l^+l^-$ $(l = e, \mu)$ which provides not only a QED test up to $O(\alpha^4)$ but also an experimental check for the procedures adopted in the study of the hadronic photon structure functions. Moreover the application of advanced statistical techniques like unfolding (Chap. 5) helps to limit the influence of physics hypothesis used to correct the observed distributions for limited acceptance and efficiency of the detectors.

4.2.1 Di-Lepton production

The reaction $e^+e^- \to e^+e^-\gamma\gamma \to e^+e^-l^+l^-$ in a single tag configuration, where l can be any charged lepton, arises from QED $O(\alpha^4)$ processes [50] and may be considered as deep inelastic $e-\gamma$ scattering. In fact, high energy electrons can split off photons with a lifetime of order $\tau \simeq \frac{E}{m_e}p_T^{-1}$ where E is the beam energy and p_T is the γ transverse momentum relative to the beam direction. Time dilation renders this lifetime much longer than typical reaction times (of order 10^{-23} sec) so that the photons can well be treated as real particles in a scattering process [11].

Using the data collected from 1991 to 1994 with the L3 experiment at LEP, we have investigated deep inelastic $e-\gamma$ scattering using the following leptonic reactions:

$$e\gamma \to e + e^+ + e^-,$$

$$e\gamma \to e + \mu^+ + \mu^-,$$

where the three final leptons are detected and γ is an almost real photon radiated by the untagged electron.

The lowest order Feynman diagrams which describe the reactions $e^+e^- \to 4$ leptons can be classified as: multiperipheral, annihilation, bremsstrahlung and conversion (Fig.4.4). The dominant contribution is the multiperipheral diagram, which

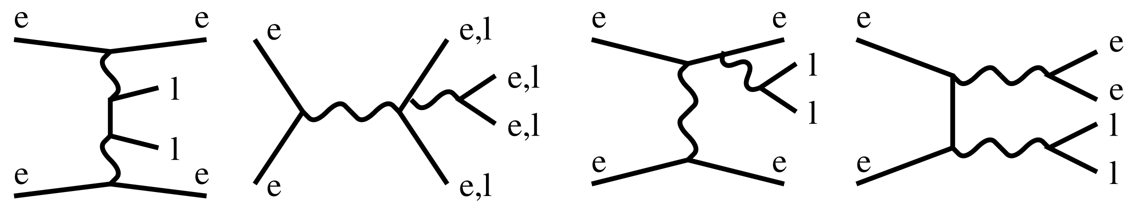

Multiperipheral **Annihilation** **Bremsstrahlung** **Conversion**

Figure 4.4: Lowest order diagrams describing the reaction $e^+e^- \longrightarrow e^+e^-l^+l^-$.

involves the two-photon interaction. Annihilation and Bremsstrahlung contributions become important only for small di-lepton masses.

4.2.2 Kinematics and Cross-Sections

The kinematical configuration and the description of the variables used hereafter are described in Fig.4.5. The e^+ (resp. e^-) and e^- (resp. e^+) of the beam are scattered at an angle $\theta_{1,2}$. The probe and target photon have four-momenta k_1 and k_2 with virtualities $Q^2 = -k_1^2$ and $t^2 = -k_2^2$. The value of Q^2 is measured by the four-momentum transfer squared of the tagged electron:

$$Q^2 \simeq 2E_{beam}E_1(1-\cos\theta_1) \text{ where } E_1 \text{ is the energy of the tagged electron.}$$

The energy of the photon scaled by the beam energy defines the variables $x_{1,2} = k^0_{1,2}/E_{beam} = E^{\gamma}_{1,2}/E_{beam}$. The Bjorken scaling variables x and y are defined as

$$x = \frac{Q^2}{2k_1k_2} = \frac{Q^2}{Q^2+W^2_{\gamma\gamma}}; \qquad y = \frac{k_2k_1}{k_2p_1} \simeq 1 - \frac{E_1}{E_{beam}}\cos^2\frac{\theta_1}{2} \simeq x_1$$

where the mass squared of the produced lepton pair is $M_{ll} = W^2_{\gamma\gamma} = (k_1+k_2)^2$.

The cross-section for deep-inelastic electron scattering on a photon target can be written as the sum of the contributions of transverse (T) and longitudinal (L) photons. By using the target photon flux $dn(x_2)/dx_2$, the differential cross-section

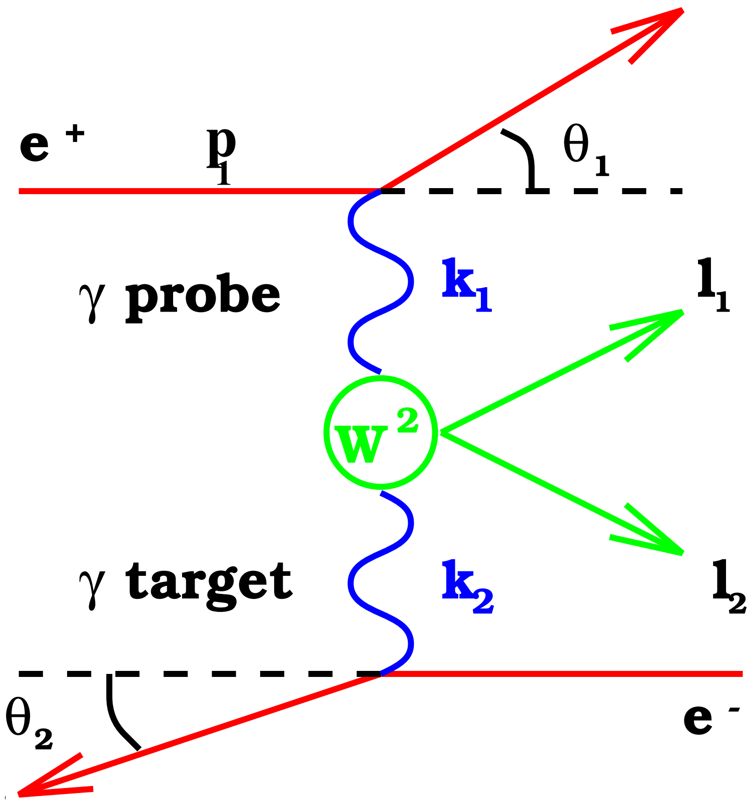

Figure 4.5: Definition of kinematical variables.

is written as [50, 71]:

$$\frac{d^3\sigma}{dxdQ^2dx_2} = \frac{4\pi\alpha^2}{Q^4}\frac{1}{x}\frac{dn(x_2)}{dx_2}\left\{[(1-y+\frac{y^2}{2})]F_2^\gamma(x,Q^2) + \frac{y^2}{2}F_L^\gamma(x,Q^2)\right\} \tag{4.1}$$

where the flux of the target photon is given by:

$$\frac{dn(x_2)}{dx_2} = \frac{\alpha}{\pi x_2}\left\{[1+(1-x_2)^2]\ln\left(\frac{2E(1-x_2)}{m_e x_2}sin\frac{\theta_2^{max}}{2}\right) - 1 + x_2\right\} \tag{4.2}$$

and

$F_T^\gamma \propto \sigma_{TT}$; $F_L^\gamma \propto \sigma_{TL}$ and $F_2^\gamma = 2xF_T^\gamma + F_L^\gamma$

are the photon structure functions, proportional to the cross-sections σ_{ij} for transversely and longitudinally polarized virtual photons. The first index refers to the target photon while the second index refers to the probe photon. In the present analysis, y^2 is small, on average $< 4.5 \cdot 10^{-2}$; therefore the measurement of the differential cross-section is sensitive only to F_2^γ. By neglecting terms of the order of m_l^2/Q^2, the QED prediction for the photon structure function $F_2^\gamma(x, t^2, W_{\gamma\gamma}^2)$ is [71]:

$$F_2^\gamma = \frac{\alpha}{\pi} x \left\{ [x^2 + (1-x)^2] \ln \frac{W_{\gamma\gamma}^2}{m_l^2 + t^2 x(1-x)} - 1 + 8x(1-x) + \frac{t^2 x(1-x)}{m_l^2 + t^2 x(1-x)} \right\} \tag{4.3}$$

The measurement of the differential cross-section $d^2\sigma/dxdQ^2$ gives access to the determination of F_2^γ, whereas F_L^γ will not be obtained with this approach. Moreover, F_L^γ is not the only structure function that contains additional information.

Triggering on a final-state particle a, additional structure functions become accessible by studying the differential cross-section as a function of the direction of a. In this case, the cross-section can be written in terms of differential structure functions[1] $\overline{F_i}^\gamma$, $i = T, L, A$ and B as follow[10]:

$$\frac{d^3\sigma}{dxdyd\Omega_a/4\pi} = \frac{2\pi\alpha^2}{Q^2} \frac{1+(1-y)^2}{xy} [\underbrace{(2x\overline{F}_T^\gamma + \epsilon(y)\overline{F}_L^\gamma)}_{F_2^\gamma} - \rho(y)\overline{F}_A^\gamma \cos\chi + \frac{1}{2}\epsilon(y)\overline{F}_B^\gamma \cos 2\chi] \tag{4.4}$$

where [72]

$$\epsilon(y) = \frac{2(1-y)}{1+(1-y)^2} \simeq 1,$$
$$\rho(y) = \frac{(2-y)\sqrt{1-y}}{1+(1-y)^2} \simeq 1$$

and χ is defined in Fig. 4.6. This analysis is of major interest in QCD applications since for hadronic final states the quantities $\overline{F}_i^\gamma$ involve a convolution over the parton densities of the photon. However, before applying this method to a complex hadronic final-state, it is interesting to apply the azimuthal correlations method in a QED configuration where the $\overline{F}_i^\gamma$'s for leptonic final-states are uniquely given by perturbation theory.

[1] The structure functions are obtained by integrating $\overline{F_i}^\gamma$ over Ω_a.

We have successfully applied this method to the di-muon final state (see Chapter 8), obtaining the first measurement of the leptonic structure functions F_A^γ and F_B^γ. The framework used and the relation between the new structure functions F_A^γ, F_B^γ and the helicity states of the colliding photons is explained in the next section.

4.2.3 Azimuthal Correlations

The scattering amplitude of longitudinally polarized photons may be observed by measuring angular correlations in the $\gamma\gamma$ center-of-mass [71, 72, 73, 74]. Assuming that the target photon direction is parallel to the beam axis, two independent angles can be defined in the $\gamma\gamma$ center of mass system (Fig. 4.6): the polar angle of the μ^-, θ^*, and the azimuthal angle χ. The azimuthal angle is the angle between the plane of the two-body final state and the $\gamma\gamma$ axis, and the plane defined by the tagged electron and the $\gamma\gamma$ axis.

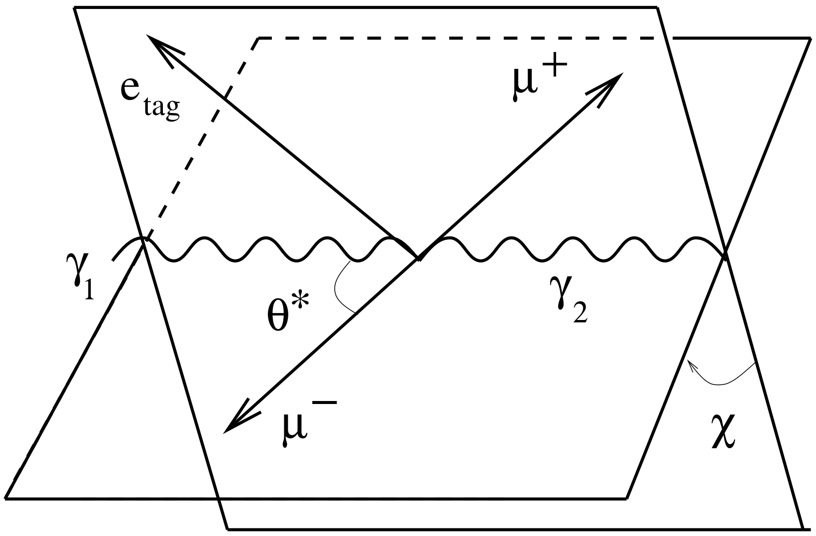

Figure 4.6: Definition of the angles θ^* and χ in the $\gamma\gamma$ center of mass frame, used for the analysis of the azimuthal correlations.

The decomposition of the cross-section into the contributions from the different photon helicity amplitudes leads to a formula with 13 terms each having a different azimuthal dependence [73]. In the single-tag configuration, neglecting the longitudinal component of the target photon, only three terms remain in the cross-section formula which can be written as [72] (equivalent to Eq. 4.4):

$$\frac{d^4\sigma}{dxdydzd\chi} = \frac{2\pi\alpha^2}{Q^2}\frac{1+(1-y)^2}{xy}[A_1(x,z) + A_2(x,z)\cdot\cos\chi + A_3(x,z)\cdot\cos 2\chi] \tag{4.5}$$

where $z = \cos\theta^*$. The coefficients A_1, A_2, A_3 are related to the three differential structure functions $\overline{F}_2^\gamma, \overline{F}_A^\gamma, \overline{F}_B^\gamma$ [72]:

$$\begin{aligned} A_1 &= \overline{F}_2^\gamma(x,z) = 2x\overline{F}_T^\gamma(x,z) + \overline{F}_L^\gamma(x,z) \\ A_2 &= -\overline{F}_A^\gamma(x,z) \\ A_3 &= \tfrac{1}{2}\overline{F}_B^\gamma(x,z) \end{aligned} \tag{4.6}$$

The sum of the amplitudes squared of the helicity states is given by A_1 while A_2 and A_3 are the interference terms leading to the $\cos\chi$ and $\cos 2\chi$ modulation [73]. The coefficients A_i are calculable in QED. They can be expressed in good approximation[2] as [71, 72, 74]:

$$\begin{aligned} A_1 &\simeq \frac{x\alpha}{\pi}\left([x^2+(1-x)^2]\frac{1+(\beta z)^2}{1-(\beta z)^2} + 4x(1-x)\right) \\ A_2 &\simeq -\frac{4\alpha}{\pi}x(1-2x)\sqrt{x(1-x)}\frac{z}{\sqrt{1-(\beta z)^2}} \\ A_3 &\simeq \frac{2\alpha}{\pi}x^2(1-x) \end{aligned}$$

where $\beta = \sqrt{1-4xm_l^2/[Q^2(1-x)]}$. The symbol $\simeq$ indicates that $\gamma\gamma$ luminosity functions, proportional to $1-y$ ($\epsilon(y)$ and $\rho(y)$ in Eq. 4.4), have been set to one [50]. Also it is assumed that the target photon is purely transverse.

The structure functions F_2^γ, F_A^γ and F_B^γ are recovered by integrating $\overline{F}_i^\gamma$ over z. Since A_2 comes from the interference between longitudinal and transverse photons (Fig.4.7), it is sensitive to the amplitude with two-photon helicity $\lambda = 1$ whose square is the longitudinal structure function.

[2]Note that the formulae in Ref.[74] are incorrect.

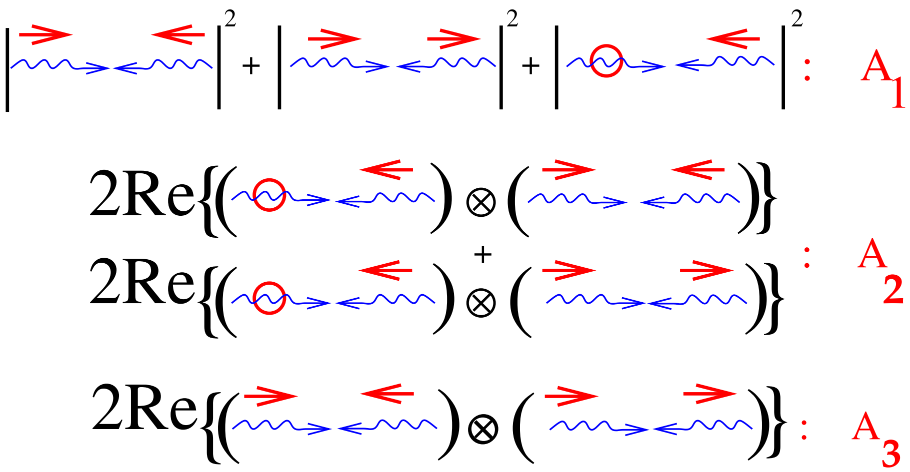

Figure 4.7: For a single-tag configuration, the target photon is almost real and, in a very good approximation, purely transverse. There are only three possible independent helicity amplitudes. We show here, schematically, the relation between the coefficients A_i's and the photon helicity states. A_1 is the quadratic sum of the total photon helicity $\lambda = 0, 2$ and 1. A_2 and A_3 are interference terms. Target photons are represented on the right and probe photons on the left. The longitudinal component of the probe photon can be obtained from a measurement of A_2.

The interference between two transverse photons is described by $A_3 \propto F_B^\gamma$. It must be noted that although F_L^γ and F_B^γ are described in QED by the same function of x and z, and, although in the literature both are referred to as 'F_L^γ', their helicity structure is different. Indeed, in F_B^γ the photons are purely transverse. Since the longitudinal structure function F_L^γ appears in the cross-section formula (Eq.4.1) multiplied by the small factor y^2 it is difficult to obtain it from a cross-section measurement. The coefficient A_2 has no such suppression factor and therefore we have access to the longitudinal amplitude from the measurement of the azimuthal angle distribution.

At LEP, the leptonic structure function F_2^γ has been measured by OPAL [75] and DELPHI [76]. OPAL has also analyzed the azimuthal correlations [77], they extracted only the value of A_3.

4.3 Monte Carlo Simulation Techniques

The problem to simulate a distribution according to an underlining theory, can be treated in terms of a multiple integration over a given set of probability distributions. This implies that an N-dimensional integral has to be computed. Moreover, in an ideal experiment, measured distributions can by directly compared to theoretical predictions. In practice, the observed distributions contains background and reflect limited acceptance and detector inefficiencies. The magnitude of the distortion induced by the detector on a given observed distribution depends usually upon many probability distributions.

Analytical evaluation of such integrals is not possible, so numerical methods must be used. However, for integrals with many dimensions, even a numerical integration becomes challenging. The Monte Carlo method gives a way of evaluating these multi-dimensional integrals by a random sampling from probability density distributions [78].

Usually different phases can be distinguished:

- **Generation:** events, i.e. ensemble of 4-vectors, are "generated" by Monte Carlo techniques according to the theoretical description of the studied process.
- **Simulation and reconstruction:** The passage of the particles through the detector is simulated taking into account the possible decays of those particles and their interactions with different materials of the detector. A final phase, called reconstruction, applies all the detector inefficiencies to the simulated events, so that a direct comparison between these artificial events and the observed ones is possible.

The first phase depends only on the particular physical process studied and is therefore detector independent, whereas the successive simulation and reconstruction are directly related to the characteristics of the detector used.

In our analysis, to calculate efficiencies and backgrounds and to compare the data to the QED predictions, two Monte Carlo generators, together with a full detector simulation and reconstruction, have been used: the Berends, Daverveldt and Kleiss

(BDK) generator [79] and the Vermaseren [80] generator. The former, which calculates to $O(\alpha^4)$ the full set of QED diagrams taking into account interference effects, has been used as a reference [3] while the second, which is much faster since it has exact calculations only for the multiperipheral diagram, has been used to produce large statistics Monte Carlo samples. None of these generators simulates the initial state radiation. To check the influence of the initial state radiation on our results we have also used a Monte Carlo generator developed by F.A. Berends and P.H. Daverveldt [81, 82] which simulates the process $e^+e^- \longrightarrow e^+e^-\mu^+\mu^-(\gamma)$.

In the following subsections the different Monte Carlo generators will be briefly described.

4.3.1 The Berends, Daverveldt and Kleiss Generator (Diag36)

Among the existing $\gamma\gamma$ Monte Carlo generators, Diag36 developed by F.A. Berends, P.H. Daverveldt and R. Kleiss [79, 82, 83] is the most complete. In effect, the Diag36 Monte Carlo can generate events distributed according to the exact differential cross-section, where all the lowest order Feynman diagrams contribute and all masses are properly taken into account. In Tab. 4.1 the number of Feynman diagrams involved in the four lepton final states are given grouped in three gauge invariant sets.

Final state	Bremsstrahlung	Annihilation and Conversion	Multiperipheral
$e^+e^-e^+e^-$	16 (4)	12 (0)	8 (4)
$e^+e^-\mu^+\mu^-$	4 (2)	6 (0)	2 (2)

Table 4.1: Number of lowest order Feynman diagrams involved in the ee and $\mu\mu$ production. In parenthesis the number of diagrams involved in the single tag configuration

The principal achievement of BDK arises from the large number of Feynman diagrams which have to be taken into account. The complete calculation of a matrix element squared cannot be deduced from the standard spin summing and trace calculation. Instead, the calculation is performed on the amplitude level [84] which avoids

[3] In the BDK program, large angle tagging cuts can only be put in by hand, i.e. by throwing away those events that do not satisfy the cuts, reducing considerably the efficiency in this application.

spin summation. Therefore the generator treat the cross-section as the square of a sum of specifically chosen sub-amplitudes. An accurate description of the generation algorithm (see the articles [79, 82, 83]) is beyond the scope of this text and we limit this outlook to a few general comments. The major difficulties are related both to the right choice of the spinor representation and to the choice of the best set of variables describing all the peaks (up to 657 in the ee final state) of the differential cross-section in a seven dimensional space. The first choice must allow to factorize the amplitude of each diagram into a product of scalar quantities, whereas the choice of the variables describing the structure of all the peaks of the differential cross-section is essential to avoid numerical instabilities. Therefore the cross-section is treated as a squared amplitude internally subdivided in a number of sub-amplitudes corresponding to the each of the invariant sets contributing to the final state: multiperipheral, annihilation, conversion and bremsstrahlung. Each sub-amplitude being generated by a dedicated sub-generator. The interference between the sub-amplitudes is taken into account by weighting the events.

Since a number of processes such as $e^+e^- \longrightarrow e^+e^-e^+e^-$, $e^+e^- \longrightarrow e^+e^-\mu^+\mu^-$, $e^+e^- \longrightarrow \mu^+\mu^-\mu^+\mu^-$, $e^+e^- \longrightarrow \mu^+\mu^-\tau^+\tau^-$, can be generated via Diag36, the generator can be used either to produce distributions according to the studied process or to estimate the number backgrounds events contributing to it. The relatives contributions to the total cross-section from the different sets of lowest order Feynman diagrams, can also be studied as function of the kinematical cuts, which can be entered beforehand by the user.

4.3.2 The Vermaseren Generator

The main practical difference between the BDK and Vermaseren generators, is that the Vermasersen generator takes into account only the Multiperipheral diagram moreover, the algorithm is less time consuming than the one used by the BDK generator. Hence, once verified that the other sets on gauge invariant Feynman diagrams are negligible in our kinematical configuration, the Vermaseren Generator can be used to produce a large sample of Monte Carlo events. With present-day computer technology, algorithms performances are rarely a problem, but, only few years ago it was not the case and Vermaseren generator allows for a massive production of $e^+e^- \longrightarrow e^+e^-\mu^+\mu^-$ Monte Carlo events. The basic concept of this generator [85] is to reduce the difficulties arising in computing cross-sections integrated over an experimental acceptance. Many mathematically oriented integration methods may have great difficulties with discontinuities caused by experimental cuts. To overcome this problem, the method used by Vermaseren is to rewrite the phase-space integrals so that the denominators of the propagators (responsible of the severe matrix element's peaks) can be directly used as integration variables. The consequence of this approach is that nearly all cuts become conditions that are functions of more than one variable. The VEGAS program [86] is then used to compute the integrals. In that way, the Vermaseren program can deal with any kind of experimental cuts. A carefull comparson between those two generators can be found in [47].

4.3.3 Radiative Corrections

The comparison of data with theory requires a careful treatment of radiative QED effects. It is clear that, for the cross section relevant for experimental analyses, there should be no contribution from final-state radiation as the calorimetric measurements combine the particle with nearby photon(s). A formal approach of this problem can be found in e.g. [87, 88]. For the case of charged lepton-nucleon scattering QED corrections are dominated by photon radiation off the tagged lepton line. For the case of electron-photon scattering, there might be additional sizeable corrections to the untagged electron line and thus influence of radiative corrections must be carefully analized [89]. An improved version of Diag36 [81] allows to produce unweighted events of the type $e^+e^- \longrightarrow e^+e^-\mu^+\mu^-(\gamma)$. The cross-section is divided into two parts: a hard one contains events with hard bremsstrahlung (i.e. with an energy above a certain threshold), and a soft one which comprises all other events. The energy spectrum of hard bremsstrahlung photons generated by this Monte Carlo is shown in Fig. 4.8. On the basis of the total cross-section for soft and hard bremsstrahlung it is decided which kind of event will be produced.

Monte Carlo events with radiative corrections have been mainly used to monitor the effect of radiative corrections on the treatment of azimuthal correlations.

4.4 Extraction of $F_2^\gamma(x,Q^2)$ from $\frac{d^2\sigma}{dxdQ^2}$

The extraction of the structure function F_2^γ from the observed differential cross-section (Eq. 4.1) is not straightforward. The cross-section is the product of the structure function and the luminosity function of the target photon. To calculate the latter the phase space of the untagged electron must be integrated over. To do so, the following semi-analytical procedure suggested by John H. Field[4] has been applied.

For clarity, we recall the definition (see Fig. 4.5) of the variables used:

$$\begin{aligned} Q^2 &= 4EE_{tag}\sin^2\frac{\theta_1}{2}, \\ x &= Q^2/(Q^2+W^2), \\ W^2 &= W_{\gamma\gamma}^2 = (k_1+k_2)^2, \\ x_1 &= E_{\gamma_1}/E_{beam},\ x_2 = E_{\gamma_2}/E_{beam} \end{aligned}$$

and

$$y = 1 - \frac{E_{tag}}{E_{beam}}\cos^2\frac{\theta_1}{2} \simeq x_1$$

From Eq. 4.1 neglecting $O(y^2)$ terms, one obtains:

$$F_2(x,Q^2,x_1,x_2) = \frac{Q^4 x}{4\pi\alpha^2}\frac{1}{(1-x_1)}\cdot\frac{1}{(dn(x_2)/dx_2)}\cdot\frac{d^3\sigma}{dx_2 dQ^2 dx}$$

where $dn(x_2)/dx_2$ describes the photon flux of the target photon. In the single tag configuration, with θ_2^{max} small, x_2 (the scaled target photon energy) can be calculated from the measured quantities x, Q^2, x_1. Changing variables from $x, Q^2, x_2 \rightarrow x, Q^2, x_1$ the following expression can be written:

$$F_2^\gamma(x,Q^2)/\alpha = \mathcal{W}(x_1,x,Q^2)\frac{d^3\sigma}{dx_1 dQ^2 dx} \tag{4.7}$$

[4] J.H. Field, private communication.

where $\mathcal{W}(x_1, x, Q^2)$ plays the role of a weight. x_2 can be expressed in terms of x_1, x, Q^2 by introducing the following dimensionless variables:

$$\begin{aligned} q^2 &= \frac{Q^2}{4E_{beam}^2}, \\ Z &= \frac{W}{2E_{beam}}, \\ x &= \frac{q^2}{(q^2+Z^2)} \end{aligned} \tag{4.8}$$

and the following relations hold:

- $Z^2 = x_1 x_2 - \frac{1}{2}(1-x_1)(1-x_2)\cos(\Theta)$
- $\cos(\Theta) = \sin(\theta_1)\sin(\theta_2)\cos(\phi) - \cos(\theta_1)\cos(\theta_2)$
- $\phi = \phi_1 - \phi_2$ where ϕ_1, ϕ_2 are the azimuthal angles of the scattered e^+, e^- around the beam direction.

In a single tag configuration, the following approximations can be made:

$$\theta_1 >> \theta_2 \simeq 0 \Rightarrow \cos\Theta \simeq -\cos\theta_1 \Rightarrow Z^2 \simeq x_1 x_2 - q^2(1-x_2)$$

which implies:

$$\begin{aligned} x_1 &= \frac{Z^2 + q^2(1-x_2)}{x_2} \\ x_2 &= \frac{q^2+Z^2}{q^2+x_1} \end{aligned}$$

4.4.1 Extraction of $F_2(x, Q^2)$

In the discrete case, corresponding to the physical measurement of the differential cross-section, one has:

$$\frac{d^2\sigma}{dQ^2dx} \simeq \frac{1}{\mathcal{L}}\frac{\Delta^2 N}{\Delta Q^2 \Delta x}$$

where $\mathcal{L}$ is the integrated luminosity (in pb^{-1}) corresponding to the data sample used, and $\Delta^2 N/\Delta Q^2 \Delta x$ is a 2-dimensional histogram containing the number of events in bins of x and Q^2. Integrating Eq. 4.7 over x_1 one has:

$$\frac{1}{\alpha}\int_{x_1^{min}}^{x_1^{max}} F_2^\gamma(x,Q^2)dx_1 = \int_{x_1^{min}}^{x_1^{max}} \mathcal{W}(x_1,x,Q^2)\frac{1}{\mathcal{L}}\frac{\delta N(x_1)}{\delta x_1 \delta Q^2 \delta x}dx_1 \tag{4.9}$$

$$\Rightarrow \frac{(x_1^{max}-x_1^{min})}{\alpha}F_2^\gamma(x,Q^2) = \frac{1}{\mathcal{L}\Delta Q^2 \Delta x}\sum_{i=1}^{\Delta N}\mathcal{W}(x_1^i,x,Q^2) \tag{4.10}$$

$$\Downarrow$$

$$F_2^\gamma(x,Q^2)/\alpha = \frac{1}{(x_1^{max}-x_1^{min})\mathcal{L}\Delta Q^2 \Delta x}\sum_{i=1}^{\Delta N}\mathcal{W}(x_1^i,x,Q^2) \tag{4.11}$$

Thus the structure function $F_2^\gamma(x,Q^2)$ is obtained by histograming the mean[5] weight $\overline{\mathcal{W}}(x,Q^2)$ in bins of Δx, and ΔQ^2.

4.4.2 Calculation of x_1^{min} and x_1^{max}

The boundaries x_1^{min} and x_1^{max} (Eq. 4.9) are directly related to experimental cuts:

- $E_{tag} > E^o \Rightarrow x_1 < 1 - \frac{E^o}{E}$ **(A)**; where E^o is the lower energy cut for the tag.
- $\theta_1^{min} < \theta_1 < \theta_1^{max}$ (tagging acceptance)
- $\theta_2 < \theta_2^{max}$ (anti-tag condition)

For a given q^2, x_1^{min} and x_1^{max} are obtained from:

- $q^2 = (1 - x_1^{max})\sin^2\frac{\theta_1^{max}}{2}$ **(B)**
- $q^2 = (1 - x_1^{min})\sin^2\frac{\theta_1^{min}}{2}$ **(C)**

x_1^{min} is also limited by:

$$x_1 = \frac{Z^2 + q^2(1-x_2)}{x_2}$$

[5] Since it has been averaged over x_1.

$$x_2 \longrightarrow 1 \Rightarrow x_1^{min} = Z^2 \qquad \textbf{(D)}$$

and the following limits are then found:

$$\textbf{(A),(B)} \Rightarrow x_1^{max} = min\left\{1 - \frac{E^o}{E};\ 1 - \frac{q^2}{\sin^2(\theta_1^{max}/2)}\right\}$$
$$\textbf{(C),(D)} \Rightarrow x_1^{min} = max\left\{Z^2;\ 1 - \frac{q^2}{\sin^2(\theta_1^{min}/2)}\right\}$$

4.4.3 Determination of the mean weight factor $\mathcal{W}$

The mean value of the weight $\mathcal{W}$ averaged over x_1 for a given x and Q^2 bin can be extracted using Monte Carlo events with a full detector simulation. The experimental structure function is then obtained from the relation:

$$F_2^\gamma(x, Q^2)^{data} = \alpha\overline{\mathcal{W}}(x, Q^2)^{MC}\left(\frac{d^2\sigma}{dxdQ^2}\right)^{data}$$

where the bar on $\mathcal{W}$ indicates the average over $x_1 = \frac{W^2+Q^2(1-x_2)}{4E^2beamx_2}$ as in Eq. 4.10.

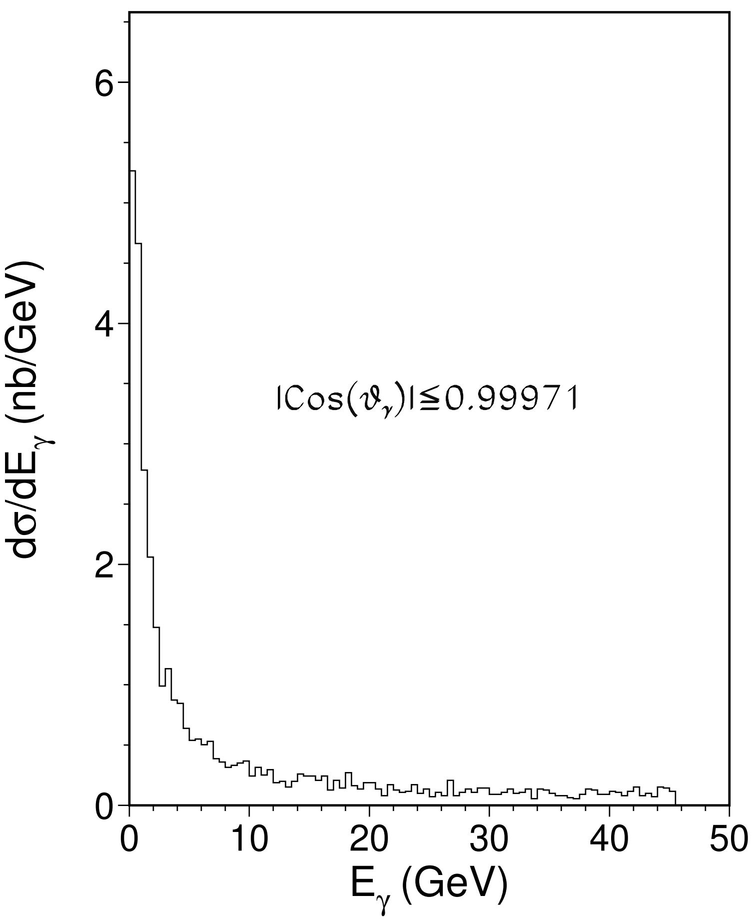

Figure 4.8: Monte Carlo Energy spectrum of hard ($E_\gamma > 200$ MeV) bremsstrahlung photons emitted inside the detector acceptance.

"Tu stesso ti fai grosso
col falso imaginar, sì che non vedi
ciò che vedresti se l'avessi scosso."
Dante, Paradiso I 88

Chapter 5

Unfolding Procedures

In high energy physics experiments, measured distributions are usually affected by the imperfections of the detector. Specifically, large uncertainties stem from the model dependence of the detector response matrix, which relates the true and observed distributions. Therefore it is important to develop methods to reduce the model dependence on the corrected distributions.

The unfolding methods are of major importance in the study of hadronic $\gamma\gamma$ processes. In this case hadrons at low angles with respect to the beam line escape detection and the model dependence of the detector response matrix causes a major problem in correcting the observed distributions for the detector effects[90, 91]. For the measurement of the leptonic structure functions of the photon, where the full final system is observed, correcting the observed distributions with unfolding techniques helps to correctly take into account the finite resolution and acceptance of the detector.

5.1 Introduction

A physical measurement is always distorted by detector effects. Two detector effects can be distinguished: limited acceptance and resolution. The former implies that the probability to observe a given event is less than one; the latter means that the quantities related to a given event can only be measured with a certain measurement error.

Every analysis requires the best possible knowledge of the response function of the detector, and this is usually achieved using a Monte Carlo simulation method. Monte Carlo simulations need two steps: the first one generates events according to the physical process, while the second one, hereafter called reconstruction, simulates the detector effects.

Lets divide quantities into three domains:

- The "*Generated domain*", assumed to reflect the physical process or our best estimation of it. It refers to the direct result of the Monte Carlo simulation without any detector effects.
- The "*Reconstructed domain*" which refers to a full detector simulated Monte Carlo. In this domain the same selections used to extract quantities of interest from the observed data can be applied, and the results can be compared to the actual observations.
- The "*Observed domain*" which refers to the actual observations. The word *measure*, in the following text, will always refers to the *observed* domain.

The widely used method, to extract from the observed data a detector independent quantity, is to use acceptance and efficiency corrections estimated from Monte Carlo simulations. A "*Reconstructed*" set of events is used to obtain the correction factors which should be applied to the measured data distribution to get rid of the detector effects. Usually this task is achieved in the following way: each Monte Carlo event, accepted by the analysis cut in the *reconstructed* domain, can be taken back to its original position in the *generated* domain, obtaining the distribution of accepted events at the Generator level. The ratio between the accepted distribution and the generated one, gives the acceptance which is directly related to the normalization of the real distribution. The ratio between the Monte Carlo reconstructed sample and the accepted one, gives a correction for a generalized efficiency (which in that case can be larger than unity). The acceptance and the generalized efficiency factors are then used to correct, bin-by-bin, the observed experimental distribution. Applying this method in one dimension needs the same binning for the Monte Carlo distributions and for the data and neglects the bin-to-bin migration. Therefore it cannot be applied if the standard deviation of the smearing produced by the detector resolution is bigger than the bin size needed for the analysis. Enlarging the bin size can solve the problem but it reduces the amount of information which can be extracted from the observed distributions. If the migration cannot be neglected, it is always possible to build the response matrix $\mathcal{A}$ which connects the number x_i of events generated in the bin i to the number of events o_j observed in the bin j with a statistical error σ_j. The problem is then to solve the finite-dimensional eigenvalue problem [92]:

$$\mathcal{A} \cdot \vec{x} + \vec{\sigma} = \vec{o} \qquad \textit{(Fredholm equation)} \tag{5.1}$$

or its integral version:

$$\int_a^b \mathcal{A}(x,y) \cdot f(x)dx + \sigma(y) = o(y) \qquad \textit{(Fredholm integral equation of the } 1^{st} \textit{ kind)} \tag{5.2}$$

where $o(y)$ (resp. $\vec{o}$) is the distribution of an observed quantity y related, by the convolution integral Eq. 5.2, to the distribution $f(x)$ of the physical quantity x defined over the interval $[a;b]$. $\mathcal{A}$ is usually called the *Kernel* of the Fredholm equation. An accurate determination of the response matrix $\mathcal{A}$ is essential for any meaningful analysis of the data.

Although it is always possible to evaluate, using Eq. 5.1 or Eq. 5.2, an expected observed distribution $o_{th}(y)$ for a given theoretical prediction $f_{th}(x)$, the inverse statement is a difficult task to achieve. The reconstruction of $\vec{x}$ or $f(x)$ from an observed distribution is called unfolding. It is an ill-posed problem [93], which can admit highly oscillating solutions.

The basic problem of an unfolding algorithm is to minimize the bias produced by the unavoidable guess introduced using a given Monte Carlo generator. Different generators may differ in the topology of the generated events and produce different acceptances once reconstructed. It is clear that, if two generated sets differ only in the shape of their distributions and not in the geometrical complexity (e.g.: topology, number of particles in the final state of the events, ...) the acceptance is not affected. It turns out that using different Monte Carlo, to correct the same set of data one has to deal with different shapes of the distributions and, if the complexity of the final state is different for the two Monte Carlo, with different acceptances. If the former effect can be easily handled by the unfolding, the latter is often unavoidable since the acceptance is supposed to be, for a given process, only an effect due to the geometry of the detector.

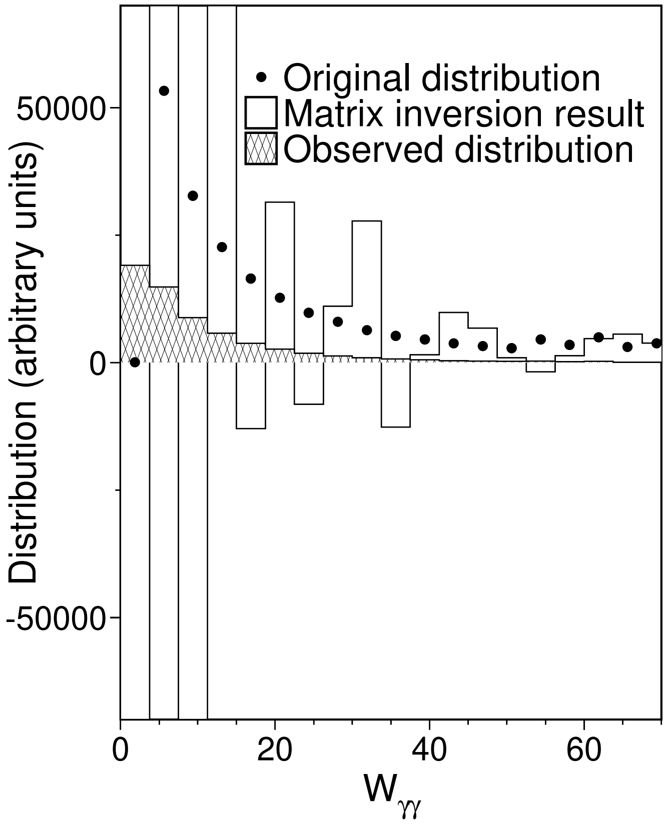

Figure 5.1: Example of an oscillating result obtained by applying the inverse of the response matrix to the observed distribution. The observed distribution and the generated one are also shown.

The best unfolded distribution, that one can hope to have, is the one which has the best agreement with the observations, once passed through the reconstruction, and which conserves an intrinsic physical meaning[1] i.e. satisfies a general "*a priori*". In other words two conditions must be fulfilled: the unfolded distribution must satisfy an a priori expectation and the bin-to-bin ratio, between the observed distribution and the reconstructed one, is a constant compatible with the unity within the statistical uncertainties.

5.2 Overview of Some Unfolding Algorithms

If the dominant effect of the detector is limited acceptance, the response matrix $\mathcal{A}$ is diagonal and the bin-by-bin correction often gives satisfactory results. When resolution effects are not negligible, applying the bin-by-bin correction will produces a biased result, with the danger of underestimating statistical and systematic errors.

A straightforward solution would be (e.g. in a discrete case with $\mathcal{A}$ a non-singular $n \times n$ matrix) to compute:

$$\vec{x} = \mathcal{A}^{-1}\vec{o}$$

however this *inversion* method often lead to disappointing results. An example is illustrated in Fig. 5.1, where the observed invariant mass distribution of the hadronic system produced by two-photon collision has been corrected by matrix inversion. This *inversion* method is clearly not acceptable since it would produce stable results only if the bin size is enlarged so as to make again the resolution corrections negligible.

Bayes' theorem[2] gives a tool [94] to solve the problem. The bayesian statistics is an important school of statistical theory, in which statistics is derived from probability theory through the use of Bayes theorem in the form [95]:

$$P(x \mid o) = P(o \mid x) \cdot P(x)/P(o)$$

[1] To the matrix inversion solution, corresponds exactly the observed distribution but can have no physical meaning

[2] The Bayes' theorem concerns conditional probabilities of the form $P(A \mid B)$ (read: "the probability of A, given B"):

$$P(A \mid B) \cdot P(B) = P(B \mid A) \cdot P(B)$$

where $P(B)$ and $P(A)$ are the unconditional (or a priori) probabilities of B and A respectively.

where x is an hypothesis and o is the experimental data. The bayesian meaning of different terms is:

$P(x \mid o)$	is the degree of belief in the hypothesis x, after the experiment which has produced data o.
$P(x)$	is the prior probability of x to be true.
$P(o \mid x)$	is the ordinary likelihood function.
$P(o)$	is the prior probability of obtaining data o

In this framework, the matrix $\mathcal{A}$ of Eq. 5.1 can be transformed into the smearing matrix $\mathcal{S}$ where $s_{ij} = \mathbf{P}(x_i \mid o_j)$ is the conditional probability that a generated quantity x_i $(i = 1, ..., n_x)$ will be reconstructed as o_j $(j = 1, ..., n_o)$. Since the generated distribution gives the probability $P(x_i)$ to generate x_i, one has [94]:

- $P(x_i \mid o_j) = \frac{P(o_j|x_i)P(x_j)}{\sum_{\xi=1}^{n_x} P(o_j|x_\xi)P(x_\xi)}$
- $\epsilon_i = \sum_{j=1}^{n_o} P(o_j \mid x_i)$ is the generalized efficiency

so the corrected distribution, will be given by (if $\epsilon_i > 0$):

$$N^{corr}(x_i) = \frac{1}{\epsilon_i} \sum_{\xi=1}^{n_o} N^{obs}(o_\xi) P(x_i \mid o_\xi). \tag{5.3}$$

At this stage one can clearly see that the result is strongly biased by the generated Monte Carlo distribution since one is forced to assume it a priori. Moreover the procedure may be instable due to statistical fluctuations. For some badly described physical process, different generators will give different sets of corrected data and this problem is generally solved by taking the differences between comparable sets of corrected data as the systematic error. To reduce the systematic uncertainties one has to minimize the influence of the generated distribution on the final result. To achieve this goal methods of "*regularised unfolding*" [94, 96, 92, 97] are used which give a robust estimation of the "*truth*". The fundamental idea is the following [98]: if the matrix $\mathcal{A}$ which describes the detector effects is singular, this means that

$Min \mid \mathcal{A}\vec{x} - \vec{o} \mid^2$ (minimizing the χ^2) could have a non unique solution[3]. Some information has been completely lost, i.e. applying the *kernel* $\mathcal{A}(x, y)$ to a function (as in Eq. 5.2) is generally a smoothing operation, so the unfolded solution, which requires inverting the operator, will be extremely sensitive to small changes or errors in the input. To overcome this problem, one can add λ times a non degenerate quadratic form $\mathcal{B}$ to the χ^2, which remove the former degeneracy yielding a one parameter family of solutions $x(\lambda)$, solution of $Min(\chi^2{+}\lambda\mathcal{B})$. As usual χ^2 is related to *a posteriori* knowledge of the solution while $\mathcal{B}$ is related to some *a priori* expectation of what the solution would be, and must clearly be as general as possible. The choice for the best value of λ ranges from the fairly objective (i.e. reduced $\chi^2 = 1$) to entirely subjective [92].

An elegant way to apply the above discussion, is to use the maximum entropy principle. Suppose that we have a discrete distribution $\vec{x} = (x_1, ..., x_N)$, the Shannon entropy is defined by [99, 100, 97]:

$$E = -\sum_{n=1}^{N} p_n log\ p_n, \text{ with } p_n = \frac{x_n}{\sum_{i=1}^{N} x_i}. \tag{5.4}$$

The unfolded solution can be obtained by minimizing the expression:

$$F = -\lambda E + \chi^2$$

i.e. the solution will be the one which maximizes the entropy and minimizes the χ^2. λ is a Lagrange multiplier determined by [101]:

$$Tr\left\{(\lambda E'' + E'E'^T)\left(1 - \frac{1}{2\lambda}CE''\right)^{-2} C\right\} = 0,$$

where E' is the gradient vector and E'' is the second derivative matrix of E with respect to x_n. C is the covariance matrix of the observed distribution. A variety of unfolding techniques are of common use in particle physics, among which the Blobel [92] and SVD [96] algorithms should be mentioned. The latter being a

[3]In that case the solution of eq. 5.3 can be unrealistic.

simplified version of the former. The Single Value Decomposition (SVD) is a loop-free algorithm (e.g. [98]) based on the homonym algebraic theorem[4]. The unfolded solution is selected solving with the help of the SVD theorem:

$$(\mathcal{A}\vec{x} - \vec{o})^T(\mathcal{A}\vec{x} - \vec{o}) + \tau \cdot (C\vec{x})^T C\vec{x} = min$$

Here C is a matrix which defines the *a priori* condition on the solution and the value of the regularization parameter τ determines the relative weight of this condition. It is possible to define the value of the parameter τ objectively [96] but the matrix C is not universal since it refers to the *a priori* condition. The Höcker and Kartvelishvili program [96], for instance, selects distributions which have the smallest possible curvature among the solutions satisfying the initial linear system in the least square sense. Regularization introduces some systematic bias into the unfolded distribution, so the method will lead to acceptable results only if the true solution is indeed in agreement with the regularization hypothesis.

5.3 The Aladino Algorithm

Most of our efforts to master unfolding techniques have been essentially done to determine the cross-section of hadron production in $\gamma\gamma$ collisions [91]. These techniques have also been an important tool to determine the leptonic structure functions of the photon. To do so, we have developed a dedicated unfolding algorithm. We approach the unfolding problem by a non-linear iterative procedure, leading asymptotically to the unfolded distribution. It must be mentioned also that this method does not require matrix inversion and the correlation matrix of each step of the iteration process is computed following the G.d'Agostini's formalism [94]. The convergence and the stability of the method has been tested on different real configurations.

5.3.1 The unfolding procedure

[4]The SVD decomposition of a real $m \times n$ matrix is its factorization of the form: $A = USV^T$ were U is an $m \times m$ orthogonal matrix, V is an nxn orthogonal matrix and S is an $m \times n$ diagonal matrix with non-negative diagonal elements.

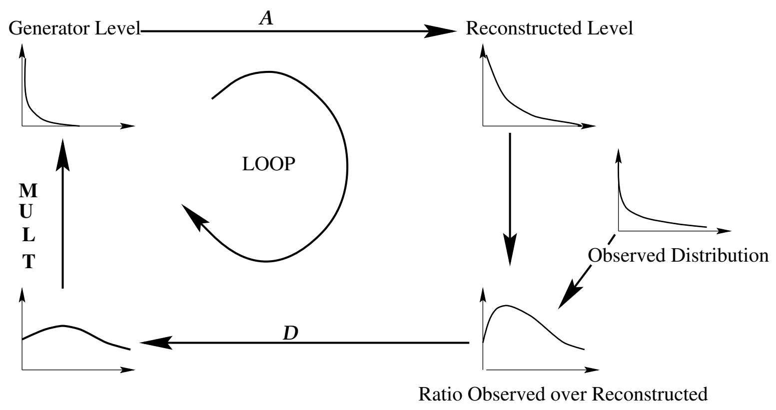

Figure 5.2: General schema of the unfolding procedure. One should continue the loop until the reconstructed distribution and the observed one reach the best agreement.

The unfolding procedure presented here, is based on the following idea: knowing the detector effects on a given measured distribution, through the matrix $\mathcal{A}$, the procedure compares the agreement between the observed and the reconstructed distributions. The distribution of the ratio between the observed and reconstructed distributions is stored as a set of correction factors and its image into the generator domain is computed by the help of a Matrix $\mathcal{D}$ which takes into account only the bin-to-bin migration (see Fig. 5.2). The initial generated distribution is modified by multiplying it by the correction factors and the loop is closed by applying again the matrix $\mathcal{A}$ to this new distribution yielding a new reconstructed one. The best solution is identified with the one obtained at the n^{th} step for which, the comparison between the corresponding reconstructed distribution and the observed data, gives the smallest χ^2 with the correction factor distribution in the reconstructed domain compatible with the unity. The regularization hypothesis is introduced assuming a smooth distribution of the correction factors.

The previous arguments can be formalized as follow:

- $\mathbf{A}$ is a $N_r \times N_g$ matrix with elements[5] $\mathbf{a}_{ij}$ containing the number of events generated in x_j and observed in o_i. The matrix $\mathcal{A}$ of elements a_{ij} is then

[5] Do not confuse $\mathbf{a}_{ij}$ with a_{ij}.

derived from $\mathbf{A}$:

$$a_{ij} = \frac{\mathbf{a}_{ij}}{x_j}$$

- N_g the number of generated cells (i.e. the number of bins in the generated distribution),
- N_r the number of reconstructed cells,
- $\vec{o}$ is the set of observed data (each component of the vector containing the occupancy of the corresponding bin in the distribution),
- $\vec{x}$ the generated distribution,
- $\vec{R}$ the reconstructed distribution satisfying:

$$\mathcal{A} \cdot \vec{x} = \vec{R}$$

- $\mathcal{D}$ the matrix allowing to pass the correction factors from the reconstructed domain back to the generated domain, and defined by:

$$\begin{aligned} h_{ij} &= \frac{\mathbf{a}_{ij}}{\sum_{\xi=1}^{N_r} \mathbf{a}_{i\xi}} \\ \mathcal{D} &= (H)^T, \quad \mathcal{D} \text{ is a matrix with elements } d_{ji} \end{aligned}$$

- $\vec{c}$ the correction factors in the reconstructed domain,
- $\vec{c}_g$ correction factors in the generator domain.

Obviously $\mathcal{A}$ is a $N_r \times N_g$ matrix while the dimension of $\mathcal{D}$ is $N_g \times N_r$ and the equations can then be written as follow:

$$R^i = \sum_{j=1}^{N_g} a_{ij} x_j \tag{5.5}$$

$$c^i = \frac{o_i}{R^i} = \frac{o_i}{\sum_{j=1}^{N_g} a_{ij} x_j} \tag{5.6}$$

$$c_g^j = \frac{\sum_{i=1}^{N_r} d_{ji} o_i}{\sum_{j=1}^{N_g} a_{ij} x_j} \tag{5.7}$$

If x_n^j is the j^{th} component of the unfolded distribution at the n^{th} step, the unfolded distribution corresponding to the $(n+1)^{th}$ step is given by:

$$x_{n+1}^j = \frac{\sum_{i=1}^{N_r} d_{ji} o_i}{\sum_{\xi=1}^{N_g} a_{i\xi} x_n^\xi} \cdot x_n^j = \sum_{i=1}^{N_r} u_{ji} o_i \tag{5.8}$$

where u_{ji} is the element of the $N_g \times N_r$ unfolding matrix $\mathcal{U}$ which can be written as:

$$u_{ji} = \frac{d_{ji} x_n^j}{\sum_{\xi=1}^{N_g} a_{i\xi} x_n^\xi} \tag{5.9}$$

For each iteration the χ^2 between $\vec{R}_n$ and $\vec{o}$ is computed as well as the mean value and the standard deviation of the c_i distribution. The best step is chosen by imposing the smallest χ^2 and verifying that the corresponding c_i distribution is compatible with a constant equal to 1.

The accuracy on the determination of the parameters c_i depends principally from the statistical error of the data distribution (one can always generate more Monte Carlo events to reduce the statistical error on the generated quantities). Therefore, some elements in the c_i distribution may be determined with an extremely poor accuracy and may produce undesirable effects on the final result. To overcome this problem, one can smooth the c_i's by applying a weighted fit to a polynomial. Usually a 3^{rd} degree polynomial is sufficient but it may be tuned accordingly to the process studied (one cannot treat in the same way all the problems). The smoothing is compatible with the unfolding since it contains the "*a priori guess*" needed to treat the information lost (see 5.1). A method of particular interest which can be used to smooth the coefficients c_i is summarized in the next section.

5.4 The Savitzky-Golay Method of Smoothing

It is sometimes useful to smooth the c distribution avoiding a bias introduced by the polynomial fit. Therefore it is interesting to test also results coming from the application of digital filters. The oscillations of nearby points of a given distribution, induced by the statistical fluctuations and measurement errors, can be seen as an high-frequency noise affecting the underlying measured physical distribution. Therefore it can be useful to apply a numerical method which filters by local averaging the spurious oscillations without affecting the underlying distribution. Savitzky-Golay method allows to build a numerical filter which plays a role equivalent to the *low-pass* filters in electronics. Usually the c distribution is both slowly varying and corrupted by statistical fluctuations. The premises of data smoothing by application of *low-pass* filters are thus satisfied. Since nearby points measure very nearly the same underlying value, averaging can reduce the influence of statistical fluctuations without biasing the final value. In most of the numerical *low-pass* filters [98], properties are defined in the Fourier domain and must be translated to the *direct* domain[6] (or *time domain*). This can add some difficulties due to the data sampling.

Savitzky-Golay filters [102] are of particular interest since they derive directly from a particular formulation of the data smoothing problem in the time domain. Usually they are used to render visible the relative widths and heights of spectral lines in noisy spectrometric data [98]. Their utility in the regularization for the unfolding problem is straightforward.

Note that usually standard *low pass* filters, preserve the area subtended by the original distribution (zeroth moment) and the location of its maximums (first moment) but violate the second moment, equivalent to the line width. Therefore they are not suitable to smooth distributions used, e.g., to determine a decay width.

The idea of Savitzky-Golay filtering is to find filter coefficients f_n that preserve higher moments. This is done by building a moving window centered on the point c_i over which the underlying distribution is approximated by a polynomial of higher order, typically quadratic or quartic. For each point c_i a least-square fit to a polynomial over the $n_L + n_R + 1$ points (n_L is the number of points on the left hand side of c_i lying inside the moving window; n_R is the number of points on the right hand side) in the moving window is performed; g_i (the smoothed value) is then set

[6] Since those methods are usually related to time dependent measurements, the observed distributions are usually referred to the time domain, while their Fourier transformations are referred to the frequency domain.

to be the value of that polynomial at the point i. By centering the window on the point c_{i+1} the whole least-square fitting is repeated. Fortunately, since the process of least-square fitting involves only a linear matrix inversion, the coefficients of a fitted polynomial are themselves linear in the values of the data [98]. It can be proven that there are particular sets of filter coefficients f_n for which the equation:

$$g_i = \sum_{n=n_L}^{n_R} f_n c_{i+n}$$

automatically accomplishes the process of polynomial least-square fitting inside a moving window. The are defined by:

$$\mathcal{B} = \text{ Matrix of components } b_{ij} \text{ with:}$$
$$b_{ij} = i^j \qquad i = -n_L, ..., n_R, \qquad j = 0, ..., M$$

Were M is the order of the polynomial and:

$$f_n = \sum_{m=0}^{M} \{(B^T \cdot B)^{-1}\}_{0m} n^m$$

It is clear that the dimensions of the moving window correspond to a correlation length in the smoothed result and therefore must be adapted to the studied problem.

5.5 The Covariance Matrix

Once the unfolding has been performed, one cannot just take the uncertainties from the Poisson's errors in the final distributions. The bin-to-bin migration causes a correlation between the observed data (indeed distributed according to a Poisson distribution) and the unfolded result. The covariance matrix $\mathcal{V}$ has then two contributions: one coming from the measured distribution and one coming from the effect of the unfolding matrix $\mathcal{U}$ and his elements can be written as [94]:

$$v_{kl} = v_{kl}(\vec{o}) + v_{kl}(\mathcal{U})$$

A rigorous calculation of the covariance matrix $\mathcal{V}$ in this framework is given in [94] and we have applied this formalism to our equations.

5.6 Results

5.6.1 The program *Aladino*

The method described above has been implemented in a Fortran code. It is divided into three sections:

- A) Input: one must enter through a dedicated subroutine the matrix $\mathbf{A}$ in number of events, the generated distribution $\vec{x}_0$ and the observed distribution $\vec{o}$. The number of bins in the generated distribution (resp. observed one) must be entered in the parameter nx (resp. nb). The number of bins in the Monte Carlo and in the data should be optimized by using the covariance matrix in order to obtain the less correlated results.

- B) Transform $\mathbf{A}$ into the probability density matrix $\mathcal{A}$ and deduce the matrix $\mathcal{D}$.

- C) Start the loop. At each step, the correction factors c_i are determined, their distribution is smoothed (if needed) and the corresponding factors c_g^i are computed. The c_g^i's are then applied to the original Monte Carlo generated distribution and the loop is closed. At each step, the covariance matrix is computed.

5.6.2 Examples

We have applied our algorithm to two different cases which differ in the structure of the smearing matrix $\mathcal{A}$. In the first case the matrix is not diagonal while, in the second case the matrix is diagonal with some non-vanishing off-diagonal elements.

It must be noted that in the following examples the Monte Carlo and data distributions are not normalized to the luminosity so that the number of events of the unfolded result is directly related to the luminosity of the data.

Example 1: Formal test on a pure Monte Carlo sample

In this example, the the observed invariant mass of the hadronic final state in two-photon events is smaller than the *real* or generated one. This implies that the matrix $\mathcal{A}$ is not diagonal (Fig. 5.3). A standard bin-to-bin correction cannot be applied since in this case it is impossible to determine a correction factor for $W_{\gamma\gamma} \geq 20$ GeV. Moreover the matrix inversion method gives unrealistic results, as shown in Fig. 5.1. Unrealistic means that we do not believe in the oscillating solution and we need to obtain a solution which is at the same time in agreement (statistically) with the obseved data and in agreement with our a priori knowledge of the physical process (i.e. a smooth solution). Therefore we need to apply an unfolding algorithm. In this example we analyse the dependence of the unfolded result on an a priori hypothesis.

We take two Monte Carlo programs generating the same physics process but with different methods. We would like to test the following: if we apply the unfolding method based on the first Monte Carlo to the reconstructed distribution obtained with the second one, is the unfolded solution compatible with the generated distribution of the second Monte Carlo?

To do this, the process $\gamma\gamma \longrightarrow$ hadrons has been generated and the visible invariant mass $W_{\gamma\gamma}$ of the $\gamma\gamma$ system has been reconstructed.

The two generators used are PHOJET [103] and PYTHIA [104]. The L3 detector [5] effects are simulated and the analysis program is then applied. The two sets differs in the number of generated events and the acceptance obtained from the two Monte Carlo slightly differs in the low mass bins. Moreover with PYTHIA we have produced events with $W_{\gamma\gamma} \geq 5$ GeV, while with PHOJET, events have been produced with $W_{\gamma\gamma} \geq 3$ GeV.

The differences in the acceptance are located in the matrix $\mathcal{A}_{PHOJET}$ and $\mathcal{A}_{PYTHIA}$ and there is clearly no way to eliminate the effect only by unfolding the one dimension invariant mass distribution. This effect is clearly visible in Fig. 5.4 and must be taken as systematic error.

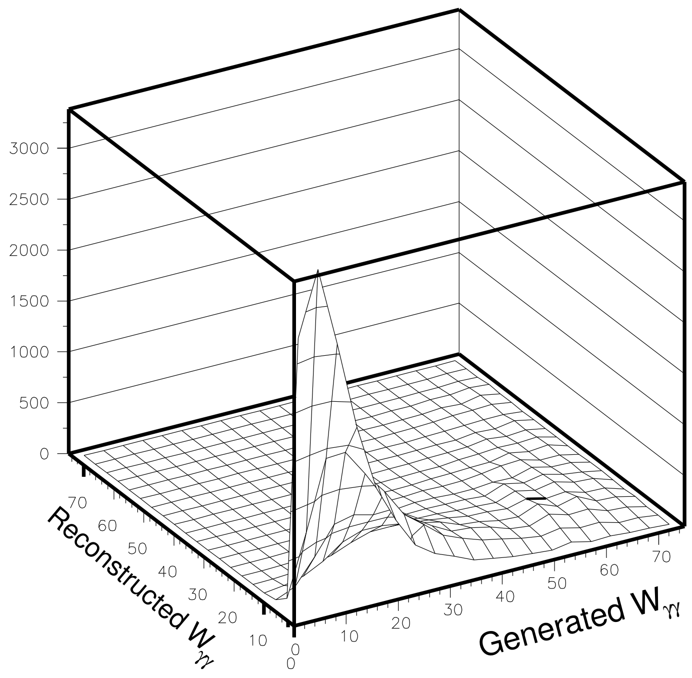

Figure 5.3: Correlation matrix A relating to number of reconstructed events to the number of generated events.

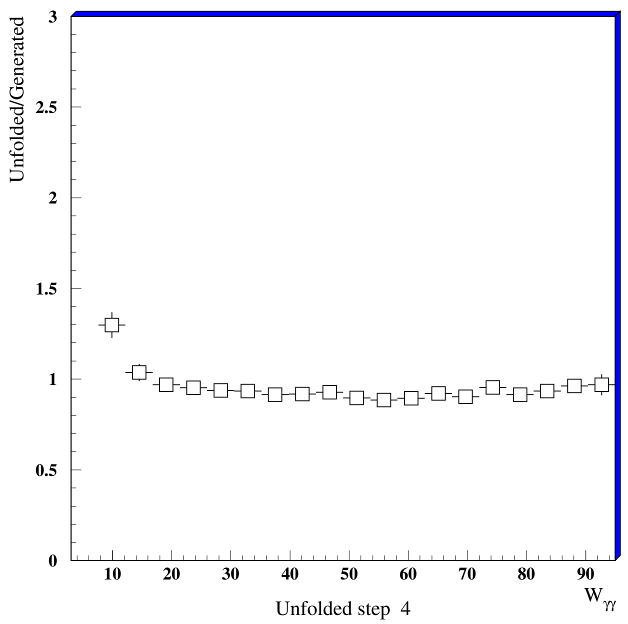

Figure 5.4: Bin-to-bin ratio between the unfolded distribution obtained with PHOJET and the PYTHIA generated distribution which has been used to construct the input vector $\vec{o}$ for the unfolding procedure. One can see that the PYTHIA distribution is correctly reconstructed except for the low mass bins where the acceptance between the two generators is different.

5.6.3 Example 2: Unfolding the azimuthal correlation in $\gamma\gamma$ collisions

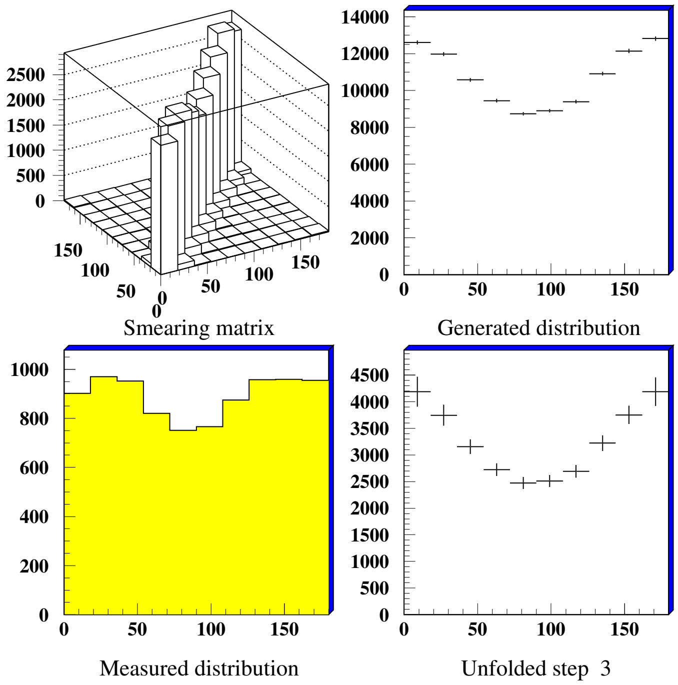

Figure 5.5: The first (top-left) plot shows the smearing matrix obtained while the second (top-right) shows the corresponding generated distribution. The third plot (bottom-left) shows the observed distribution to be unfolded. The fourth plot shows the result of the unfolding.The numer of events is reported in the vertical axis of the four plots

We have applied the above algorithm to the study of the $\gamma\gamma$ structure functions done with the L3 detector. In particular we give here as an example the unfolding procedure applied to the study of azimuthal correlations between the scattering plane of the tagged electron and the di-lepton production plan [105, 80]. In this case we are in a pure QED framework and, since the underlying physics is known, one can apply equation 5.3 to solve the problem. Nevertheless the limited statistics in Monte Carlo causes some instabilities in the solution and to cross-check the result, our unfolding method has been applied. The results are shown in Fig. 5.5. The errors for the unfolded distribution are the square-root of the diagonal elements of the covariance matrix.

5.7 Conclusion

We have developed a very simple and self-contained algorithm which allows to unfold the detector effects from the observed data. Our aim was to minimize the influence of the generated distribution in the final result.

The main idea is based on the fact that, if we know the detector response for a given process, we should be able to reconstruct the original quantity out of the observed one by imposing that the image of the unfolded distribution in the observable domain should have the best agreement with the observed one. The algorithm has been found to converge rapidly and can be applied to a wide range of physical processes. The generalization to a two-dimensional unfolding is easy to achieve by adding the corresponding component to the input quantities. The formalism of G.d'Agostini [94] has been used to compute the covariance matrix. Several successful tests have been made and some of them are reported above.

"Nec tamen hic oculos falli concedimus hilum. nam quocumque loco sit lux atque umbra tueri illorum est."
Lucrezio, De Rerum Natura, IV 385.

Chapter 6

Data Analysis

6.1 Introduction

In this chapter we describe the method applied to extract the sample of di-electron and di-muon events, originating from tagged $\gamma\gamma$ collisions, using the data collected by the L3 experiment at the Z peak from 1992 to 1994 and corresponding to an integrated luminosity of 93.7 pb^{-1}.

As described in Chap. 2 and Chap. 3, the first step in producing a Monte Carlo sample consists in generating events according to the studied process. Afterwards, an additional Monte Carlo program simulates the response of the various sub-detectors to the generated particle configuration. Consequently, the raw data from the simulated detector channels are transformed into fewer higher level objects. At this stage Monte Carlo distributions are directly comparable to the data distributions and thus, the best strategy to isolate most of the interesting events can be identified and tested.

6.2 Event Selection

This analysis is based on the information provided by the central tracker, the BGO electromagnetic calorimeter (EM) and the hadron calorimeter. The luminosity monitors, situated at $\simeq 2.7$ m away from the interaction point, allow electron tagging in the region $1.4^o \leq \theta \leq 3.9^o$ and $176.1^o \leq \theta \leq 178.6^o$. For the reaction $\gamma\gamma \longrightarrow \mu^+\mu^-$, the muons are predominantly produced at low energy, therefore only a limited fraction of them is able to reach the muon spectrometer. Consequently this detector is not used for the analysis and the muon discrimination is only based on calorimetric information.

6.2.1 The Triggers

Two-photon candidates, with a tagged electron detected in the luminosity monitors, are mainly collected by the energy trigger requiring an energy deposit greater than 30 GeV in the luminosity monitor and at least one track in the central tracking chamber with a transverse momentum $p_t > 0.1$ GeV. Other triggers [5, 106] can be activated by the same events (Chap. 3) and allow the triggering efficiency to be measured (Tab. 6.1). The trigger multiplicity for the $\gamma\gamma \longrightarrow e^+e^-$ and $\gamma\gamma \longrightarrow \mu^+\mu^-$ events is shown, respectively, in Fig. 6.1 and Fig. 6.2. The corresponding box diagrams show the distribution of triggers which contribute to a given trigger multiplicity (the relation between the code used in the vertical axis of the box diagrams and the corresponding trigger is given in Tab. 6.1). Note that, as explained in Chap. 3, the Level-1 triggers contribution must be suppressed from the multiplicity to avoid double counting. It is also interesting to note that even though the kinematical configuration of both processes studied is identical, the trigger response can be very different.

The periods in which some detector and trigger instabilities were evident have been excluded from the data sample . A mean inefficiency of 1.3% for the electron channel and 2.7% for the muon channel has been found.

6.2.2 Two-Photon Preselection

The total amount of data accepted by the L3 triggers is too large to be efficiently analyzed as a whole. A standard procedure subdivides the data in a number of "physics streams" (Fig. 3.22). In this preselection, various physics event selection

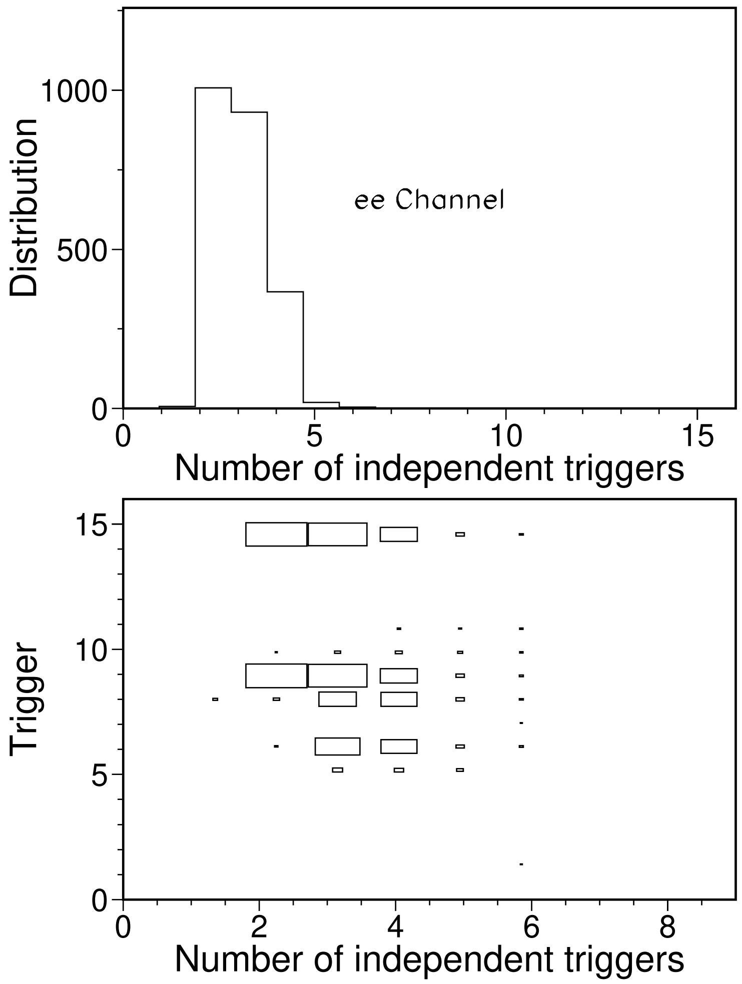

Figure 6.1: Trigger multiplicity for the $\gamma\gamma \longrightarrow e^+e^-$ channel. The lower box diagram depicts the most frequent triggers contributing to a given multiplicity. On the vertical axis, triggers are indentified by their code as defined in Tab. 6.1. The surface of rectangles is proportional to the occurrence of the corresponding trigger.

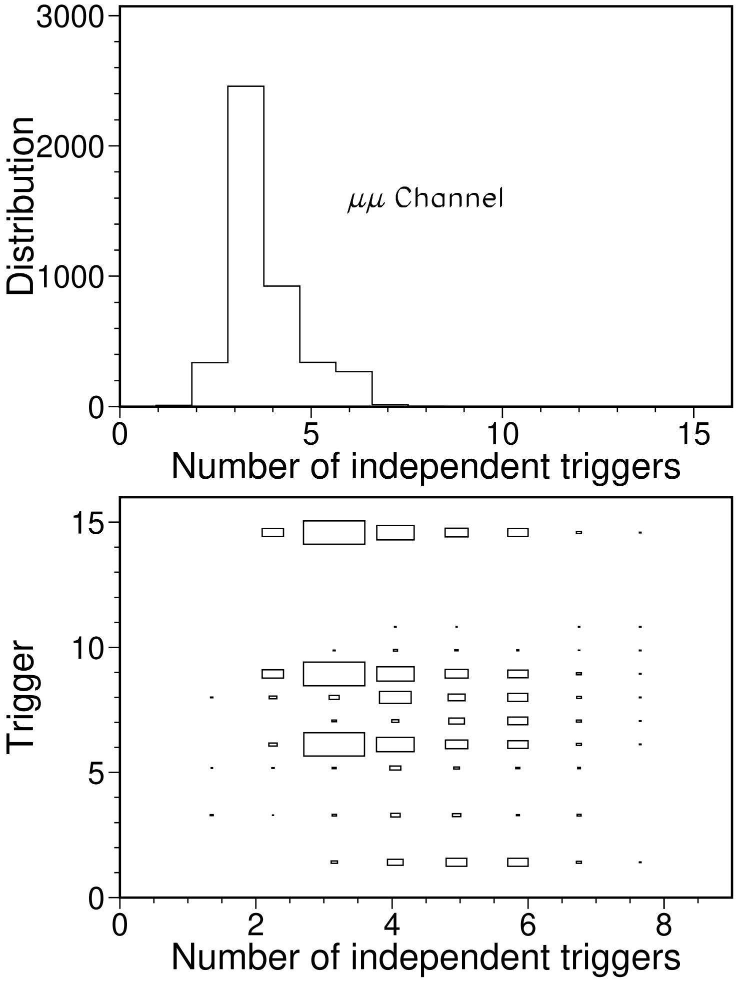

Figure 6.2: Trigger multiplicity for the $\gamma\gamma \longrightarrow \mu^+\mu^-$ channel.

Code	Trigger
1	Level-1 muon trigger
3	Forward-backward muon trigger
5	Prescaled single-tag (no tracks detected by the TEC)
6	Scintillator counters trigger
7	Muon trigger
8	TEC trigger
9	Level-1 energy trigger
10	Fast lumi trigger, flagging only
15	Energy Trigger

Table 6.1: L3 trigger mask.

Channel	Trigger code.						
	3	5	6	7	8	10	15
$e^+e^- \longrightarrow e^+e^-e^+e^-$	—	2.82	37.9	—	35.3	1.50	99.2
$e^+e^- \longrightarrow e^+e^-\mu^+\mu^-$	2.75	3.14	94.3	1.24	31.3	0.50	98.7

Table 6.2: Fraction in % of events collected by different triggers of L3.

algorithms are applied to the incoming data and different data streams are thus created, each containing events selected by the corresponding algorithm. At this stage only loose cuts are applied. The two-photon stream, called "gg stream", contains the sub-sample of data which can be further used to investigate processes like:

- Lepton production by two-photon collisions (tagged and untagged),
- $e^+e^- \longrightarrow e^+e^-n(\pi)$ for the study of low multiplicity hadronic states (resonances),
- $e^+e^- \longrightarrow e^+e^-q\overline{q}$ e.g. for the total hadronic cross-section measurement or for the determination of the hadronic structure functions of the photon.

Candidates for tagged $e^+e^- \longrightarrow e^+e^-l^+l^-$ reactions (where l can be any charged lepton) are preselected by:

- An energy deposit greater than 30 GeV in the luminosity monitors or at least an energy deposit of 10 GeV in the electromagnetic calorimeter end caps.
- An activity in the forward calorimeters must be accompanied by at least two tracks detected by the TEC and/or by some calorimetric activity. Moreover a track must satisfy the following conditions to be considered: at least 5 hits, a distance of closest approach to the nominal vertex smaller than 10 mm and a transverse momentum greater than 100 MeV.

Even tough these selection criteria are very loose, about 90% of the events collected by the L3 triggers are rejected at this stage.

6.2.3 Event Selection

Events collected in the gg stream preselection are further analyzed. Only events with a total energy deposit in the calorimeters smaller than 60 GeV are considered in order to eliminate events from Z^o decays.

Lepton pair candidates are selected by requiring two well-measured tracks with opposite charges. Tracks are required to lie inside a fiducial region defined by $28° \leq \theta \leq 152°$. Moreover, TEC tracks must be associated with a corresponding calorimetric signal. The matching between tracks and calorimeters is performed in the $x-y$ plane and must satisfy the following azimuthal condition: $\mid \phi_{TEC} - \phi_{BGO} \mid \leq 300$ mrad. The same procedure is then repeated to associate the energy deposits in the electromagnetic calorimeter to the energy deposits in the hadron calorimeter. In absence of electromagnetic activity, the matching procedure is then directly performed between tracks and hadron calorimeter signals.

In the luminosity monitors the tag condition is defined as a single shower energy deposit $E_{EM} \geq 0.75 \cdot E_{beam}$ lying inside the fiducial region $1.55^o \leq \theta \leq 3.67^o$ and $176.33^o \leq \theta \leq 178.45^o$ which excludes the innermost and outermost crystals of the detector. Single-tag events are selected by imposing that no other electron with $E_{EM} \geq 0.75 \cdot E_{beam}$ is seen in the whole L3 detector.

Finally, to eliminate radiative Z decays, only events with a total transverse momentum squared p_T^2, of the detected three body final system, greater than 0.015 GeV^2 are selected.

6.2.4 Particle Identification

Electrons and muons above 1 GeVinteract with matter principally through bremsstrahlung. Since muons are much heavier, the bremsstrahlung emission probability is strongly reduced resulting in a much lower energy loss in the traversed medium. Showers initiated by strongly interacting particles are very complex with about half of the energy going into multiparticle production and half carried by few high energy leading particles [27]. The different behavior between showers initiated by strongly interacting particles and muons energy deposit, in the energy range concerned by our analysis renders possible their separation (Fig. 6.5 and 6.6).

The total containment of electromagnetic showers in the BGO calorimeter allow for a clean electron identification. Since the electron deposits all its energy in the BGO calorimeter (it rarely reaches the hadron calorimeter), it can be identified by comparing the momentum measured by the TEC with the energy measured by the electromagnetic calorimeter (Fig. 6.3 and 6.4). Therefore, the ratio:

$$R = \frac{E_{BGO} \cdot \sin\theta_{BGO}}{P_{TEC}}$$

is used to identify electrons. For electrons, the R distribution has a Gaussian shape centered on 1 (Fig. 6.7).

To identify electrons we require:

- in the barrel region of the electromagnetic calorimeter, $44^\circ \leq \theta \leq 136^\circ$, the ratio R must be greater than 0.8 and the energy deposit $E_{BGO} \geq 0.5$ GeV
- in the end cap regions, $11.6^o \leq \theta \leq 38^o$ and $142^o \leq \theta \leq 168.4^o$, R must be greater than 0.7 and $E_{BGO} \geq 0.6$ GeV.

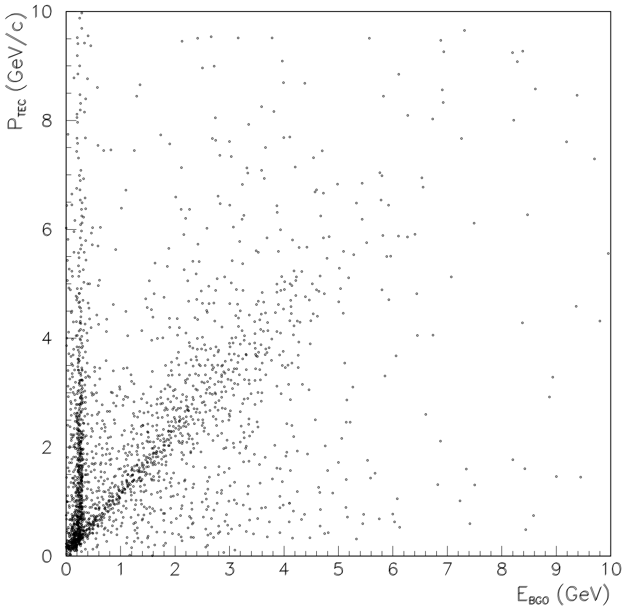

Figure 6.3: Correlation between the momentum measured in the TEC and the energy released in the electromagnetic calorimeter for tagged events

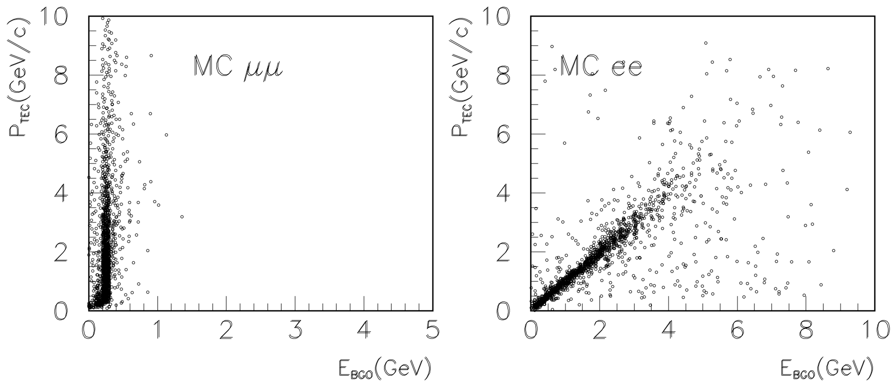

Figure 6.4: Correlation between the momentum measured in the TEC and the energy released in the electromagnetic calorimeter for Monte Carlo muons (left) and electrons (right).

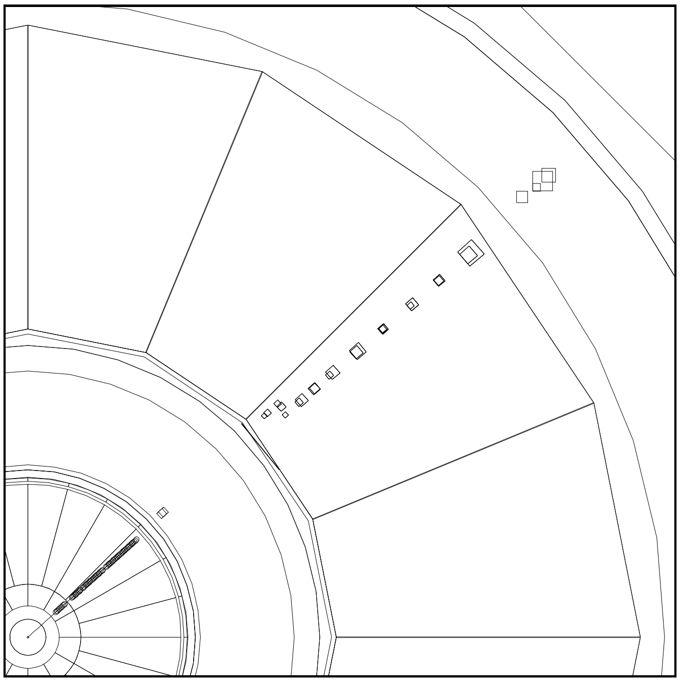

Figure 6.5: Signals of a muon. The released signal in the TEC, BGO and hadron calorimeter are visible.

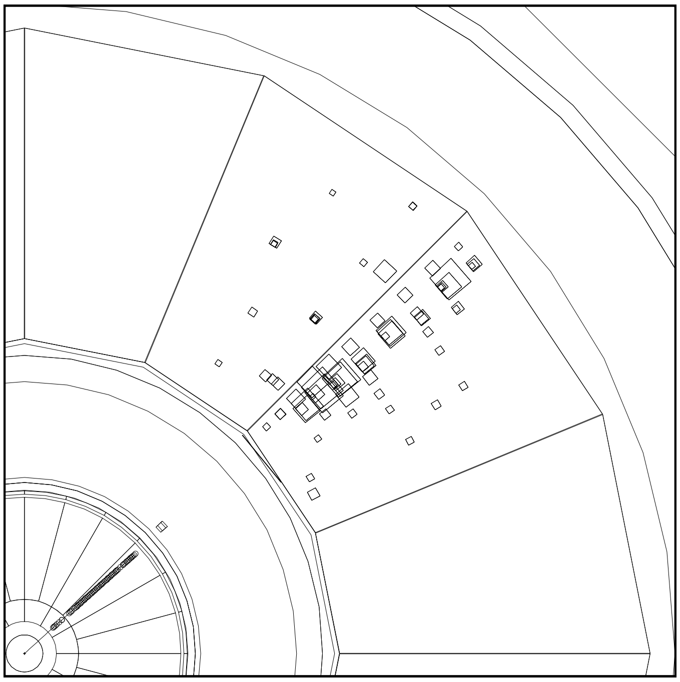

Figure 6.6: A pion generates a much wider shower in the hadronic calorimeter due to much complex structure of hadronic showers.

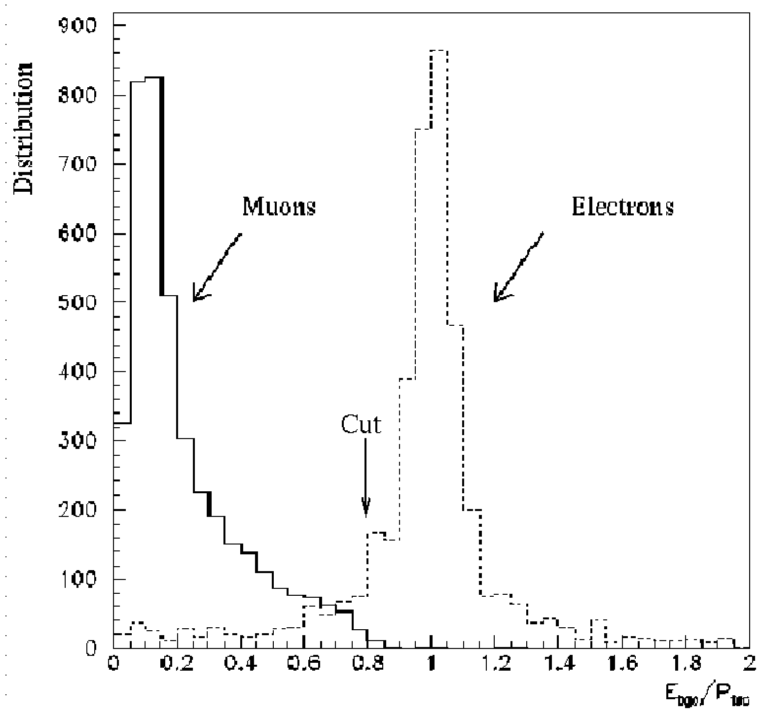

Figure 6.7: Ratio of the energy measured by the BGO to the momentum measured by the TEC obtained using Monte Carlo data. The clear separation between muons and electrons is shown.

The difference between the cuts is due to the less accurate measurements in the end cap regions.

To identify muons we require:

- an energy deposit of less than 0.40 GeV in the electromagnetic calorimeter, the signal of a minimum ionizing particle being on average 0.22 GeV. Moreover more than 95 % of the measured energy must be contained in at most 6 BGO crystals.

- some energy deposit in the hadronic calorimeter associated with the selected track. The number of hits (normalised to the number of hits expected for a minimum ionizing particle) in the hadron calorimeter, must be greater than

0.5.

For both e^+e^- and $\mu^+\mu^-$ pairs only one well identified particle is required, in order to cover uniformly the angular range defined by the tracks. In the e^+e^- sample both electrons are identified in 76% of the events. In the $\mu^+\mu^-$ sample both muons reach the hadron calorimeter in 40 % of the events and in 80% of the events both particles give a signal consistent with a minimum ionizing particle. The effective mass of the lepton pair is required to be $W_{\gamma\gamma} \geq 0.5$ GeV.

Process	Selected Events	Expected from MC	Ratio	Background Estimation (%)
$ee\mu\mu$	7288 ± 85	7119 ± 84	1.024	1.8
$eeee$	3835 ± 63	3842 ± 62	0.998	0.9

Table 6.3: Selection results compared to the MC expectations. The last column gives the estimation of the background contribution to the number of selected events.

The selection criteria were applied to the data collected from 1991 to 1994 corresponding to a total integrated luminosity of 93.7 pb^{-1}. The number of selected events, for both channels, after background subtraction (see below), is reported in Tab. 6.3 together with the Monte Carlo expectations.

The selection efficiency and acceptance, obtained by comparing the distributions of selected Monte Carlo events to the generated ones, are shown in Fig.6.8 as function of Q^2. They are uniform over the measured Q^2 range. In average they amount to 0.53 for the $\mu^+\mu^-$ channel and to 0.28 for the e^+e^- channel. The difference between the $\mu\mu$ channel and the ee channel efficiencies is explained by the fact that, for both channels, the E_{BGO} distributions are peaked in the low energy region. Therefore the $E_{BGO} > 0.5$ GeVcut used to minimize the contamination from minimum ionizing particles on the electron sample is much more severe than the cuts used to isolate muon pairs. Moreover, at the generator level, the muon sample as been generated with no particular requirements on the invariant mass of the produced di-muon system while, electrons have been produced by requiring $W_{\gamma\gamma} > 300$ MeV.

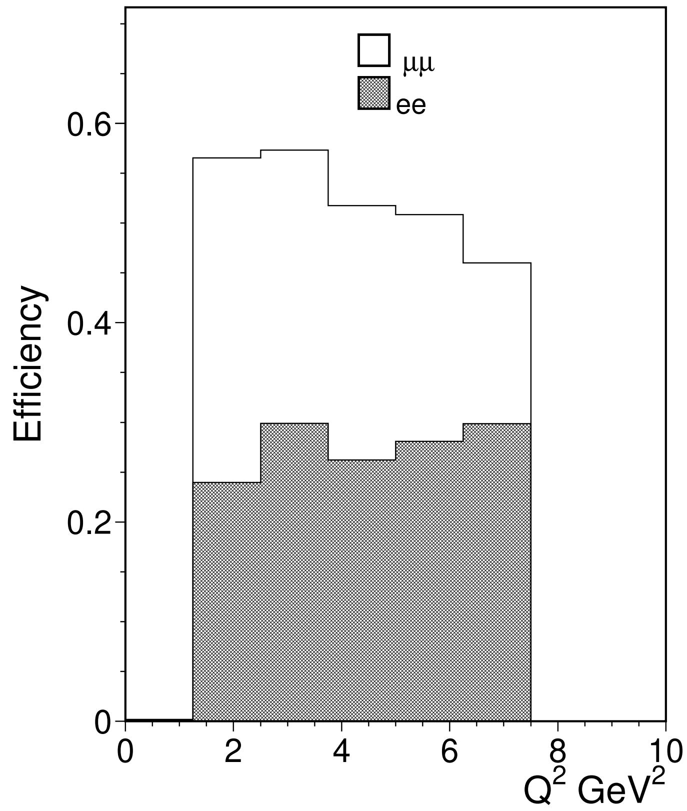

Figure 6.8: Selection efficiencies as function of Q^2 for the ee and $\mu\mu$ channels.

In Fig. 6.9 we show the experimental distributions of the polar angle of the leptons and the effective mass $W_{\gamma\gamma}$ for the electron and muon pairs. The shape of all distributions is in a very good agreement with the Monte Carlo expectations.

6.3 Background Estimation

The topology of the events and the selection criteria limit the contribution of potential backgrounds. Nevertheless, in some cases, particles misidentification could give rise to a a non negligible background contribution. We have analyzed, with Monte Carlo simulations, different reactions which could fake the final configuration

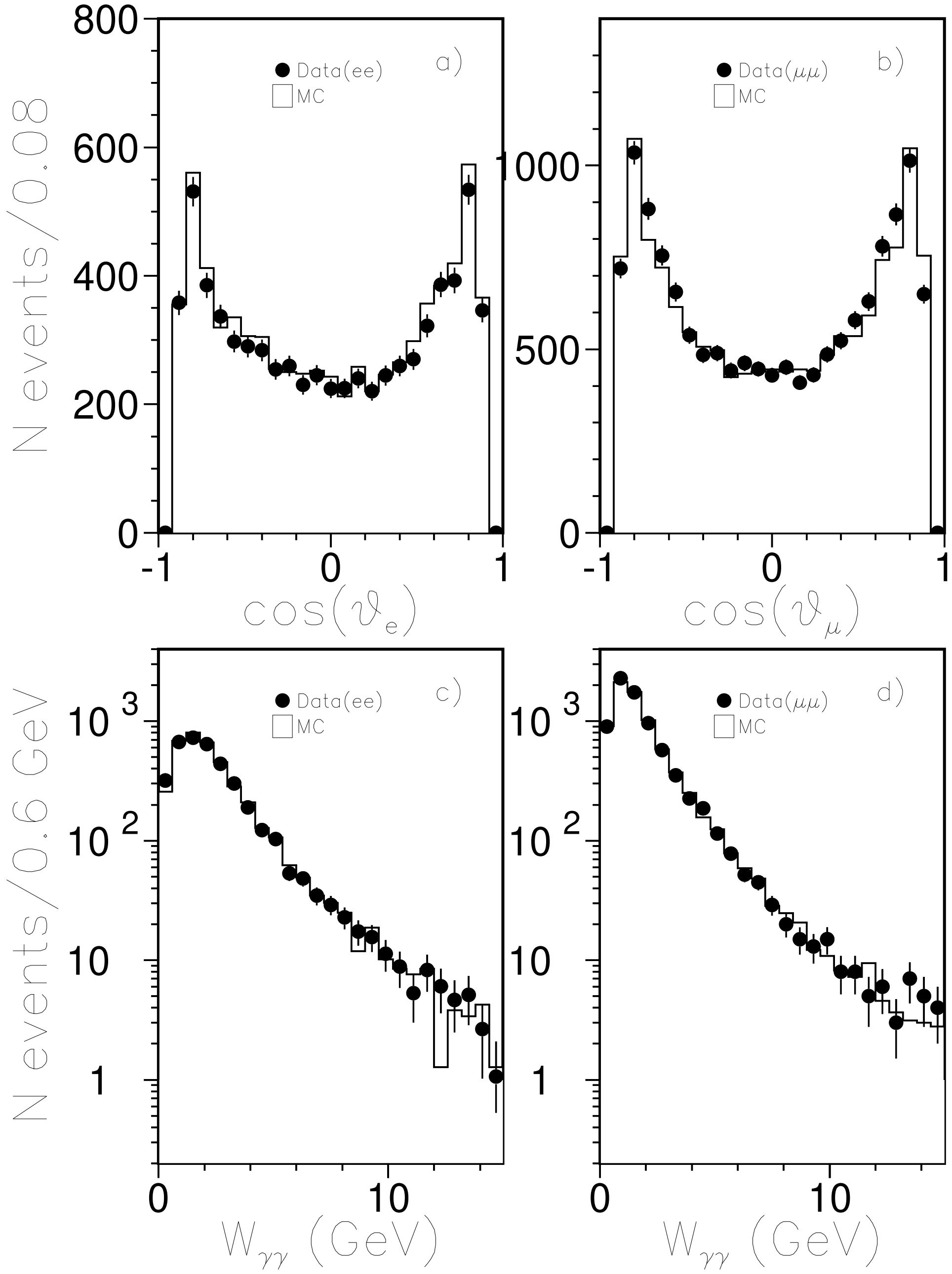

Figure 6.9: Data and Monte Carlo distributions. a) polar angle $\cos\theta$ distribution for the electrons, b) polar angle $cos\theta$ distribution for the muons, c) invariant mass distribution for the electron pairs and d) invariant mass distribution for the muon pairs.

of the $e^+e^- \longrightarrow e^+e^-e^+e^-$ and $e^+e^- \longrightarrow e^+e^-\mu^+\mu^-$ two-photon processes. The main background channels can be summarized as follow:

1. $e^+e^- \longrightarrow e^+e^-l^+l^-$ $(l = e, \mu)$ processes originating from bremsstrahlung, annihilation and conversion.

2. $Z^o \longrightarrow l^+l^-(\gamma)$.

3. $Z^o \longrightarrow q\overline{q} \longrightarrow hadrons$.

4. $e^+e^- \longrightarrow e^+e^-q\overline{q}$.

5. $e^+e^- \longrightarrow e^+e\mu^+\mu^-$ for e^+e^- channel.

6. $e^+e^- \longrightarrow e^+e^-e^+e^-$ for $\mu^+\mu^-$ channel.

7. $e^+e^- \longrightarrow e^+e^-\tau^+\tau^-$

Different dedicated Monte Carlo have been used to investigate the relative importance of the quoted reactions on the final selected data samples.

The tag conditions highly suppress the background originating from bremsstrahlung, annihilation and conversion as shown in Tab. 6.4.

Main Cuts	Channel	$\sigma_{multiper.}$(nb)	$\sigma_{ann.}$(nb)	$\sigma_{brem.}$(nb)	$\sigma_{conv.}$(nb)
$\theta_{tag} > 24$ mrad	eeee	0.42 ± 0.002			
$\theta_\mu > 25^o$			$< 10^{-4}$	$0.13 \cdot 10^{-2} \pm 0.03 \cdot 10^{-2}$	$< 10^{-3}$
$W_{\gamma\gamma} > 0.5$ GeV	$ee\mu\mu$	0.21 ± 0.002			

Table 6.4: Cross-sections for QED processes contributing to the reaction $e^+e^- \longrightarrow e^+e^-\mu^+\mu^-$ in a single tag configuration.

The background from radiative Z decays, where an emitted photon can fake the tagged electron, is found to be negligible. Even though in 30% of the radiative Z decays a photon is emitted inside the luminosity monitors acceptance, less than 1% have an energy greater than 30 GeV.

The background from other $\gamma\gamma$ interactions is 1.3 % for the electron channel, from $\tau^+\tau^-$ production (0.89%) and from misidentified muons (0.41 %). It is 1.8 % for the muon channel due to misidentified electrons (0.78 %), $\tau^+\tau^-$ production (0.71 %) and $q\bar{q}$ production (0.32 %). The various background contributions are summarized in Tab. 6.5.

Background	Channel	
	$\gamma\gamma \longrightarrow e^+e^-$	$\gamma\gamma \longrightarrow \mu^+\mu^-$
Bremsstrahlung Annihilation Conversion	—	—
Radiative Z^o decay	—	—
$\gamma\gamma \longrightarrow e^+e^-$	—	0.78 ± 0.03
$\gamma\gamma \longrightarrow \mu^+\mu^-$	0.41 ± 0.04	—
$\gamma\gamma \longrightarrow \tau^+\tau^-$	0.89 ± 0.02	0.71 ± 0.02
$\gamma\gamma \longrightarrow q\bar{q}$	—	0.32 ± 0.005
Total	1.30 ± 0.04	1.81 ± 0.04

Table 6.5: Expected background contributions in %.

6.4 Systematic Errors

The accuracy of the estimation of the cross-section for the selected events is dependent on how well we can control or compensate for systematic errors. As a general definition, a systematic error can be defined as the errors that will make our results different from the true values with reproducible discrepancies [78]. Generally these errors are not easy to detect and not easily quantified by statistical methods. They must be deduced by an analysis of experimental conditions and techniques.

The prominent sources contributing to the systematic error in our analysis have been classified as follow:

1. selection criteria,

2. trigger efficiency,

3. background subtractions,

4. luminosity measurement.

The error on the luminosity measurement [38] has been estimated to be 0.6% and must be considered as a contribution to the systematic error. The statistical error on the number of estimated background events leads to a systematic error on the number of selected signal events, after background subtraction. Therefore, the contribution to the systematic error due to the background subtraction, is estimated to be 0.04% for both the di-electron and the di-muon channel (Tab. 6.5).

A conservative estimate, of the contribution to the systematic error of the trigger efficiency, is the estimated trigger inefficiency itself.

The errors originating from the selection criteria are described below.

The selection criteria

The variation of a measured value, observed by varying the selection cuts, can be used to identify a systematic error associated with the selection procedure. To estimate the systematic error associated with a given cut, we have studied the relative variation of the ratio $\rho = (N^{data}/N^{MC})_{selected}$ as a function of the value of a given selection cut. If ρ_0 is the value of the ratio at the nominal cut, and N_0 the corresponding number of selected events, one has:

$$\frac{\Delta\rho}{\rho_0} \pm \delta\left(\frac{\Delta\rho}{\rho_0}\right) = \frac{\rho_i - \rho_0}{\rho_0} \pm \delta\left(\frac{\Delta\rho}{\rho_0}\right) \tag{6.1}$$

where

$$\delta\left(\frac{\Delta\rho}{\rho_0}\right) = \frac{\sqrt{\mid N_0 - N_i \mid}}{N_0}$$

and the subscript i indicates the new values obtained by moving a single cut to a different value. If no systematic error emanates from a given cut the relative variation of $\Delta\rho$ should be zero within statistical errors. To investigate the systematic errors induced by the selection criteria, we have moved the leading cuts by $\pm 5\%$ around their nominal value. In figures 6.10, 6.11, 6.12, 6.13, 6.14, 6.15 we show the variation of the total number of selected events by moving the lowest energy required for a tag, the ratio E_{BGO}/p_{TEC}, the minimum/maximum BGO energy deposit for e/μ identification and the Σp_T^2. For a given cut, we assign a systematic uncertainty equal to the maximum deviation observed in the $\Delta\rho/\rho_0$ distribution. These uncertainties are then summed quadratically to obtain the overall systematic error induced by the selection criteria. This results in a systematic error estimation of 1.25% for the $e^+e^- \longrightarrow e^+e^-e^+e^-$ channel and of 1.61% for the $e^+e^- \longrightarrow e^+e^-\mu^+\mu^-$ channel.

6.4.1 Summary

Once all the contributions to the systematic errors have been estimated, it is possible to identify the total systematic error as the quadratic sum of the individual contributions. The results are summarized in Tab. 6.6. Additional systematic errors related to the determination of the azimuthal correlations will be discussed in Chap. 8.

Source	Error in [%] for $e^+e^- \longrightarrow e^+e^-e^+e^-$	Error in [%] for $e^+e^- \longrightarrow e^+e^-\mu^+\mu^-$
Selection criteria	1.25	1.61
Background corrections	0.04	0.04
Trigger Efficiency	1.30	2.70
Luminosity	0.60	0.60
Total systematic error	1.90	3.20

Table 6.6: Summary table of the different contributions to the total systematic error.

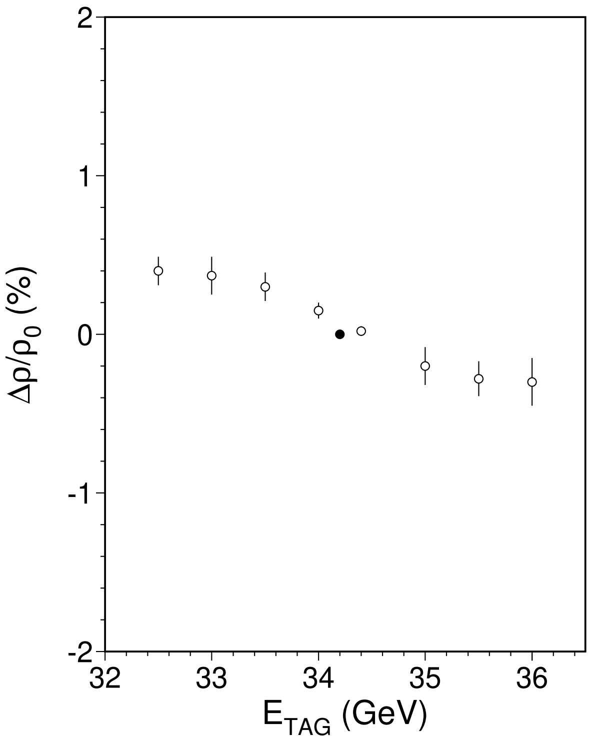

Figure 6.10: The influence on the selected number of events when moving the minimum energy required for a tag.

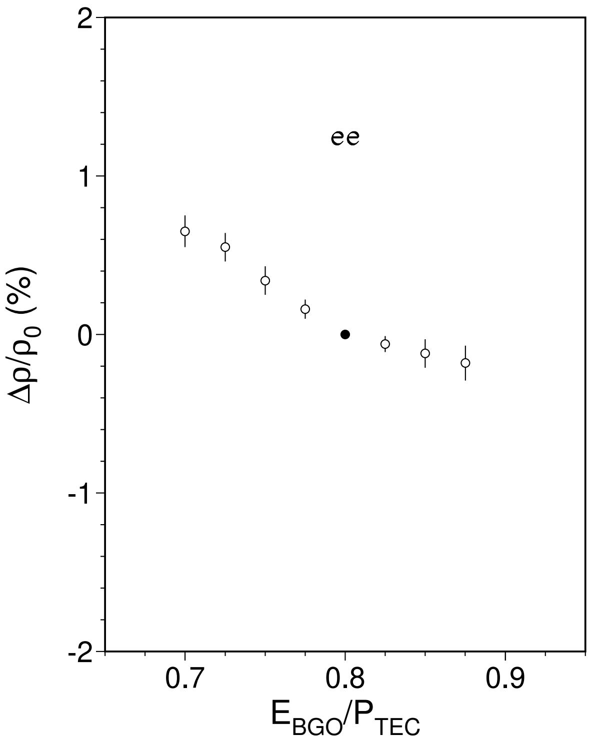

Figure 6.11: The influence on the selected number of events when moving the E_{BGO}/P_{TEC} for the electron channel.

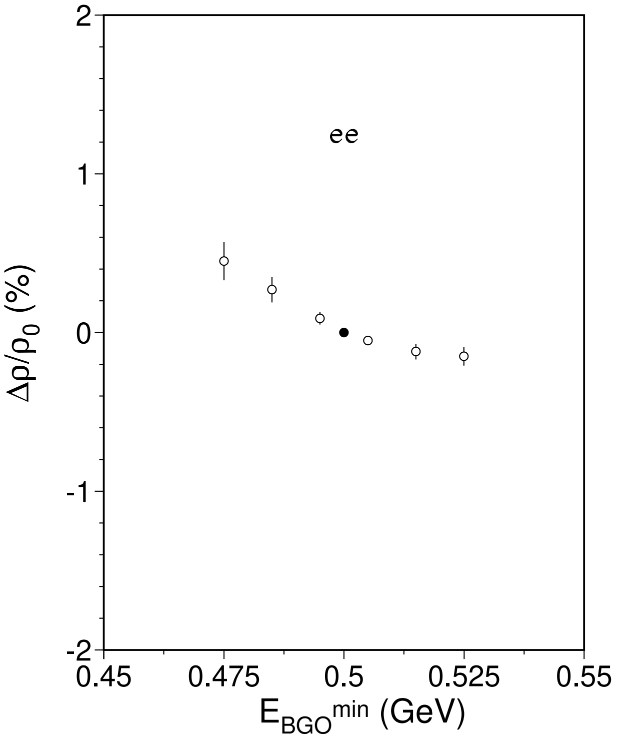

Figure 6.12: The influence on the selected number of events when moving the minimum energy required in the BGO to select electrons.

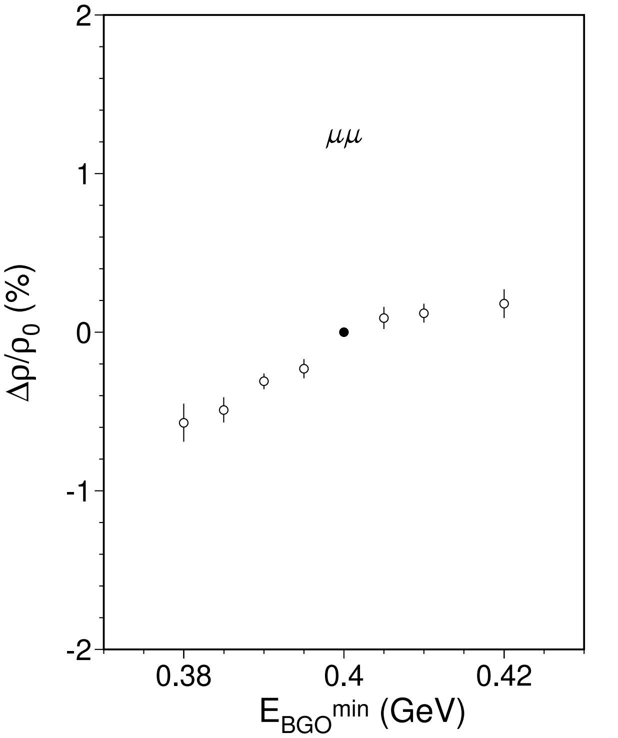

Figure 6.13: The influence on the selected number of events when moving the maximum energy deposit in the BGO to select muons.

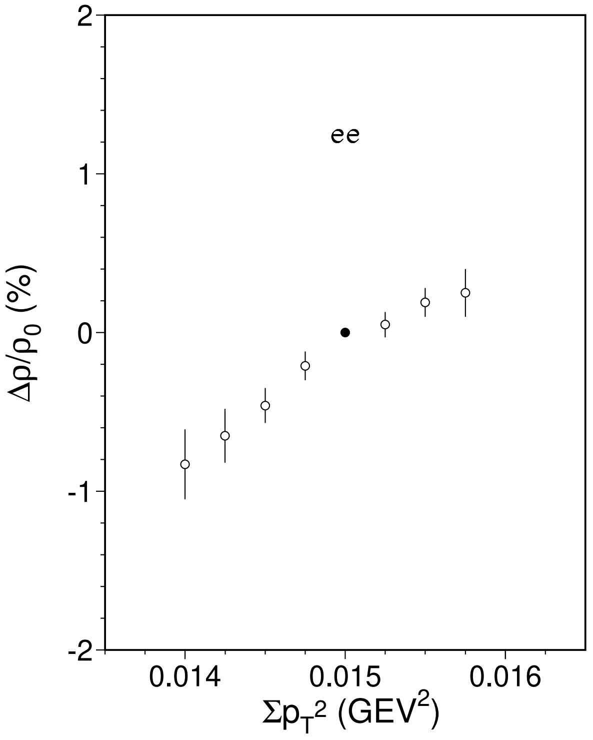

Figure 6.14: The influence on the selected number of events when moving the Σp_T^2 cut for electrons.

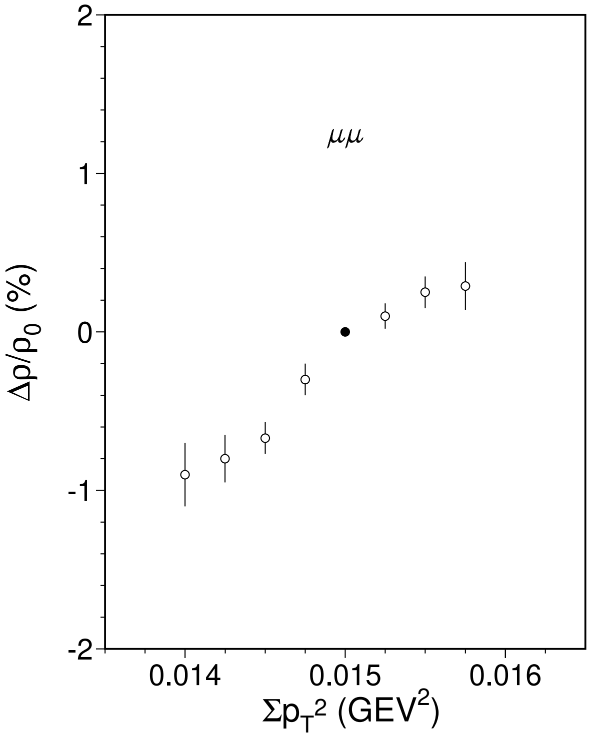

Figure 6.15: The influence on the selected number of events when moving the Σp_T^2 cut for muons.

"nam nil aegrius est quam res secernere apertas ab dubiis, animus quas ab se protinus addit."
Lucrezio, De Rerum Natura, IV 465.

Chapter 7

Analysis Results

7.1 Introduction

The physics topic to which we have devoted most of our efforts is the determination of the leptonic structure functions of the photon related to the different helicity states of the colliding $\gamma\gamma$ system. Since in our framework we are dealing with quantities which can be predicted by QED, it is possible to maximize the use of analytical predictions to compare the experimental results with the theoretical expectations. The results presented here have been collected during the LEP running at the energy of the Z^o resonance and correspond to a total integrated luminosity of 93.7 pb^{-1}.

7.2 Differential Cross-sections $d\sigma/dQ^2$.

Since the very beginning in the early 70's [60], a number of experiments, e.g. [71, 77, 107, 108, 109], have measured the cross-section of di-lepton production in tagged $\gamma\gamma$ collision over a wide range of Q^2. This measurement being essential to define the quality of the selection procedures and detector corrections can be seen as the "*line shape*" of two-photon physics.

After background subtraction, the data are corrected for acceptance and efficiency, in order to calculate the cross sections, and normalized to the total experimental luminosity as follows:

$$\frac{d\sigma}{dQ^2} = \frac{N_{data}}{\Delta Q^2 \cdot \mathcal{A} \cdot \varepsilon \cdot \mathcal{L}} \tag{7.1}$$

where:

$\mathcal{A}$ is the geometrical acceptance defined by the ratio between the Monte Carlo generated distribution and the distribution of Monte Carlo events selected by the selection criteria.

ε is the detector and selection efficiencies defined by the ratio between the distribution of the Monte Carlo with full detector simulation selected events and the same distribution at the generator level (i.e. without detector simulation)

$\mathcal{L}$ the integrated luminosity of the sample.

The acceptance and efficiency are rather uniform as function of Q^2 as shown on Fig. 6.8. The differential cross-sections $d\sigma/dQ^2$ are shown in Fig. 7.1 for $1.4 < Q^2 < 7.6$ GeV^2 and $W_{\gamma\gamma} > 0.5$ GeV, together with the analytical curves obtained from Eq. 4.1 using the Weizsäcker-Williams approximation (Eq. 4.2) for the target photon flux [50].

Notice that in this Q^2 and mass range the e^+e^- and $\mu^+\mu^-$ cross-sections are of the same order of magnitude. The excellent agreement between the analytical curves and the experimental data points is obtained with a mean four-momentum squared of the target photon of $< t^2 >= 0.033$ GeV^2. The virtuality of the target photon is discussed in the next section.

7.3 Determination of F_2^γ

We have applied the following analysis only to the $\gamma\gamma \longrightarrow \mu^+\mu^-$ events.

As shown in Chap. 4, the measured cross-section is proportional to the structure function F_2^γ. Neglecting terms in y^2 in Eq. 4.1 the relation

$$F_2^\gamma(x, Q^2) = \frac{1}{\overline{K}(x, Q^2)} \cdot \frac{d^2\sigma}{dx dQ^2}$$

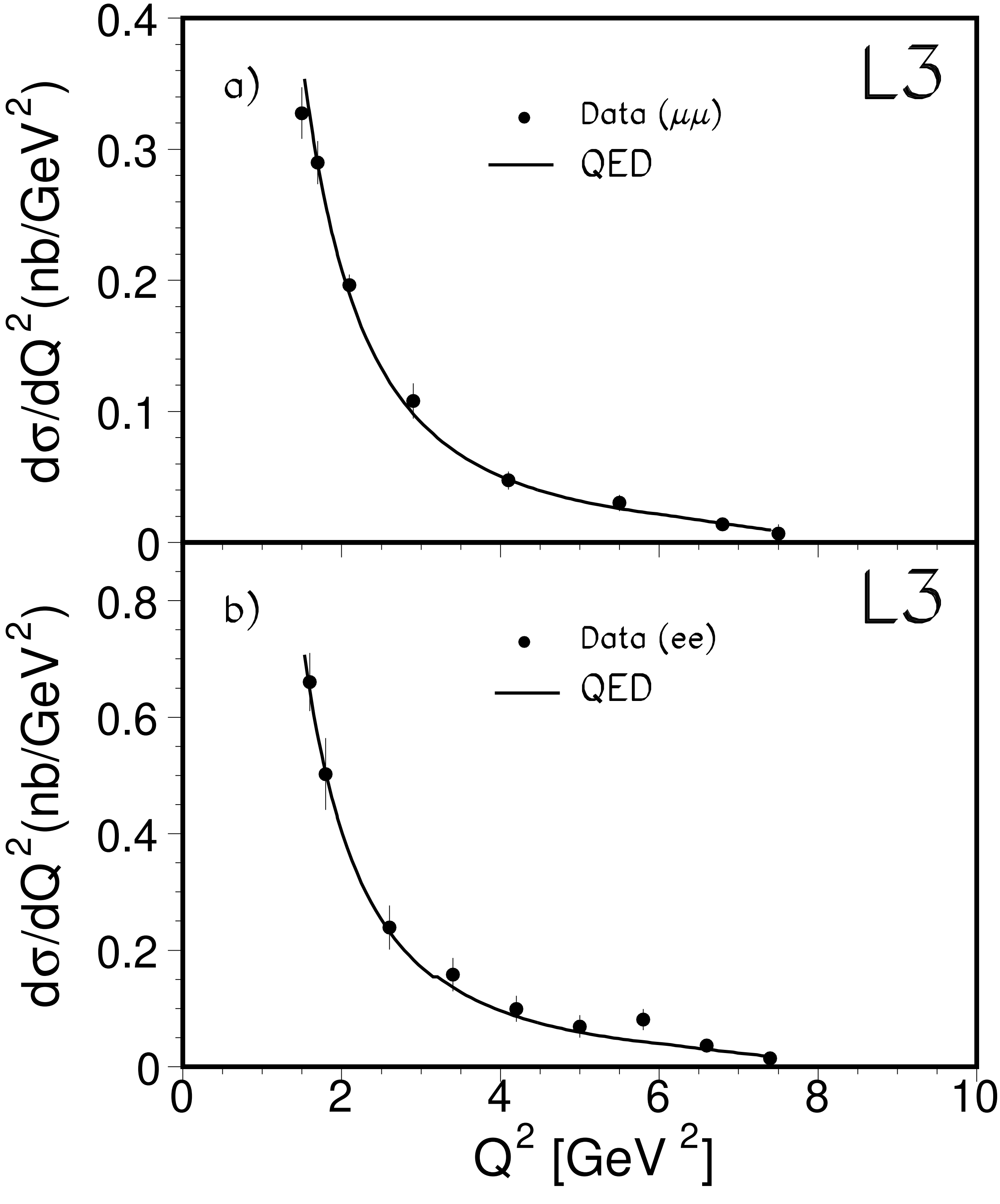

Figure 7.1: Cross sections as a function of Q^2 for $W_{\gamma\gamma} \geq 0.5$ GeV. a) the $e^+e^- \longrightarrow e^+e^-\mu^+\mu^-$ channel b)the $e^+e^- \longrightarrow e^+e^-e^+e^-$ channel . The QED curves have been obtained from Eq.4.1 and 4.3 with a mean virtuality $t^2 = 0.033$ GeV^2 for the target photon.

holds, with

$$K(x,Q^2) = \frac{\pi\alpha^2}{E^2_{beam}Q^4x}\int_{x_2^{min}}^{x_2^{max}}(1-\frac{W^2+Q^2(1-x_2)}{4E^2_{beam}x_2})\frac{dn(x_2)}{dx_2}dx_2. \qquad (7.2)$$

The average correction factor $\overline{K}(x,Q^2)$ is calculated for each bin of x and Q^2, as shown in Chap. 4, using Monte Carlo events to perform the integral of Eq. 7.2.

The value of F_2^γ thus obtained for the $\gamma\gamma \to \mu^+\mu^-$ channel is shown in Fig.7.2. If the target photon is assumed to be real ($t^2 = 0$ GeV^2) the QED prediction for F_2^γ is significantly higher than the measured values. By fitting the data with Eq.4.3 we obtain a mean value for the virtuality t^2 of the target photon of 0.033 ± 0.005 GeV^2 which is in agreement with the value of 0.034 ± 0.002 GeV^2 calculated by the Berends-Kleiss Monte Carlo program including radiative corrections [82], while, without radiative corrections the expected mean virtuality of the target photon is 0.024 ± 0.003. The analytical QED curves of Fig. 7.1 have been obtained by taking into account the mean target photon virtuality deduced from the F_2^γ measurement.

These results should be taken into account in studying the hadronic structure functions of the photon [110].

7.3.1 Azimuthal Correlations

The angular distributions of the μ^- in the $\gamma\gamma$ center-of-mass system are measured, by taking the beam axis as the target photon direction [1]. The physical distribution increases rapidly towards $z = \cos\theta^* = \pm 1$ where the detection efficiency is very small, as shown in Fig. 7.3.

Moreover the central region is most sensitive to the interference of the transverse and longitudinal photon amplitudes [73]. We therefore restrict our analysis to $\mid z \mid \leq 0.7$. The raw distribution of the azimuthal angle χ is shown in Fig.7.4.

The angular distributions are well reproduced by the Monte Carlo simulations. The data are then corrected for acceptance and efficiency in a two-dimensional grid $z-\chi$. Since the extraction of the azimuthal distributions is affected by the detector

[1] This hypothesis has been tested with Monte Carlo and no systematic effects have been noticed.

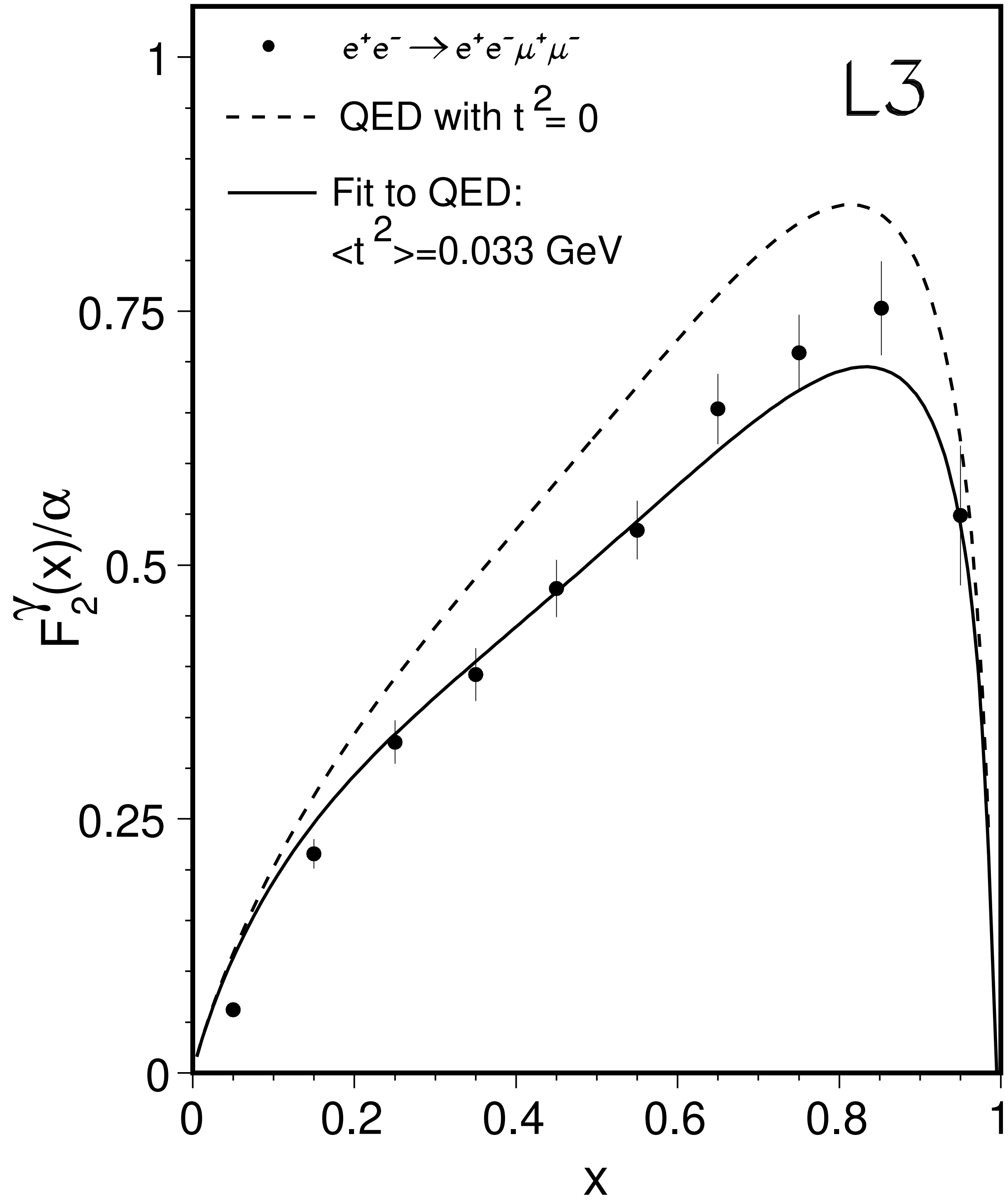

Figure 7.2: F_2^γ measured in the range 1.4 $\mathrm{GeV}^2 \leq Q^2 \leq 7.6$ GeV^2. The upper curve corresponds to $t^2 = 0$ GeV^2 while the lower curve is obtained by fitting the mean virtuality of the target photon to the data.

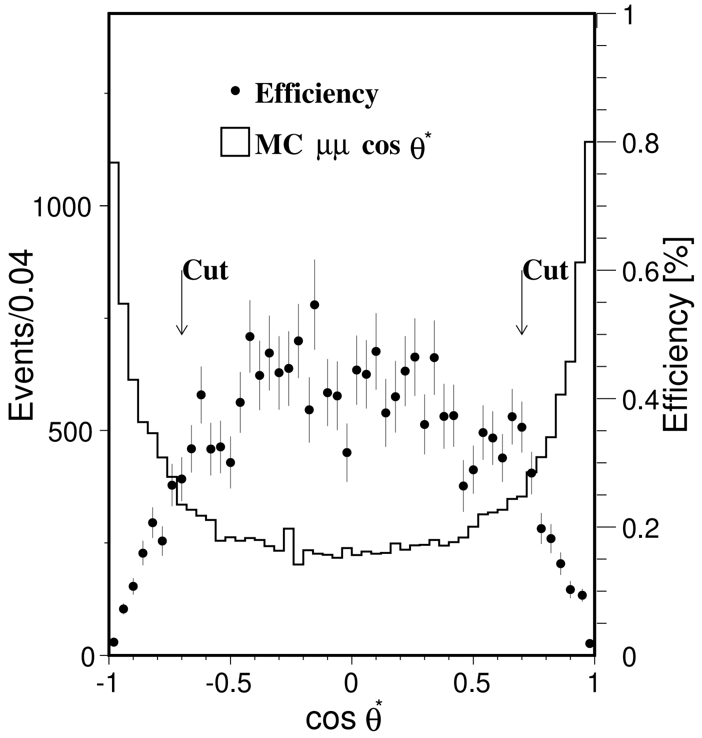

Figure 7.3: The MC distribution of z (left scale) compared to the detection efficiency (right scale). The cuts in this variable select regions with an almost uniform efficiency.

acceptance and resolution, we have used different independent correction methods: a bin-to-bin correction from the ratio of reconstructed over generated events and different procedures using unfolding algorithms. Our unfolding algorithm (Chap. 5 and [111]) has been used in parallel with algorithms recently developed by D'Agostini [94] and by Hocker and Kartvelishvili[96] to test the consistency of the results. Note that in this case the final state is entirely observed (only the untagged electron is undetected), therefore the unfolding methods only helps to take into account correctly the detector effects. All the corrected results are consistent within the statistical errors. Nevertheless, the mean deviation between the results of the different correction methods is considered as a systematic error. The result of the Aladino unfolding method, is used in the analysis; the other methods are used to estimate the system-

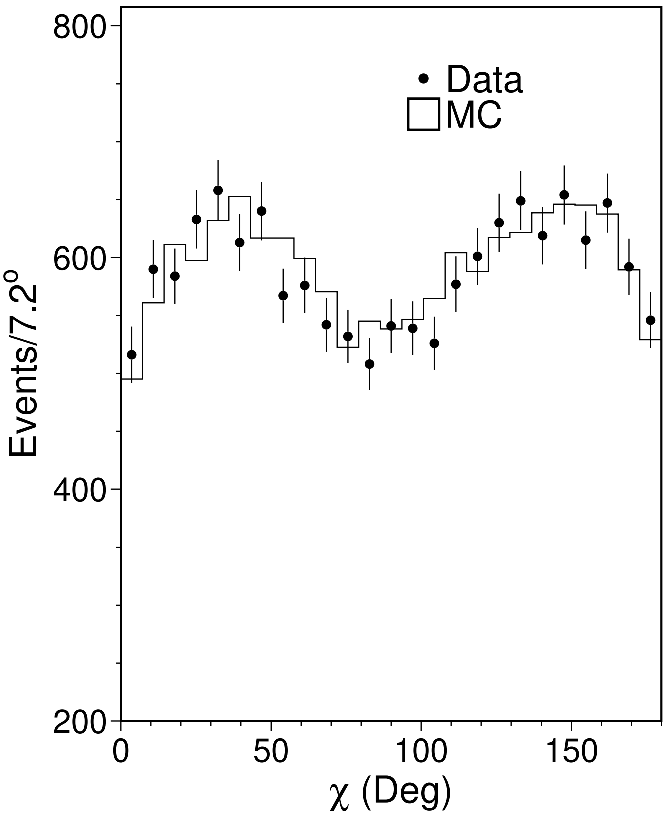

Figure 7.4: The raw azimuthal angle distribution of the μ^-.

atic errors. The χ distributions have been fitted using a function of the form:

$$\frac{dN}{d\chi} = C \cdot [1 + R_\chi \cos\chi + R_{2\chi} \cos 2\chi] \tag{7.3}$$

with R_χ, $R_{2\chi}$ and C as free parameters. From Eq. 4.5 and 4.6 it follows: $C \propto F_2^\gamma$, $R_\chi \propto F_A^\gamma / F_2^\gamma$ and $R_{2\chi} \propto F_B^\gamma / F_2^\gamma$. To analyze the x dependence of R_χ and $R_{2\chi}$ we have subdivided the x range in four intervals. Since F_A^γ is antisymmetric in z, we have studied the x dependence of R_χ in two different ranges of z: $-0.7 < z < 0.0$ and $0.0 < z < 0.7$. In Fig. 7.7 the $z < 0$ sample has been added to the $z > 0$ sample using the transformation $\chi \longrightarrow \pi - \chi$. To determine the x dependence of $R_{2\chi}$, which is symmetric in z, we have used the full range $-0.7 < z < 0.7$, in this case R_χ vanishes (Fig.7.8).

Δx	Δz	$R_\chi \pm$ stat $\pm$ syst	C_{R_χ}
0 – 0.25	0 – 0.7	$0.30 \pm 0.06 \pm 0.06$	0.6118
0.25 – 0.5	0 – 0.7	$0.10 \pm 0.07 \pm 0.05$	1.0185
0.5 – 0.75	0 – 0.7	$-0.21 \pm 0.09 \pm 0.04$	1.1368
0.75 – 1	0 – 0.7	$-0.20 \pm 0.07 \pm 0.05$	1.2089
0 – 0.25	-0.7 – 0	$-0.22 \pm 0.07 \pm 0.05$	0.6118
0.25 – 0.5	-0.7 – 0	$-0.07 \pm 0.07 \pm 0.06$	1.0185
0.5 – 0.75	-0.7 – 0	$0.16 \pm 0.09 \pm 0.06$	1.1368
0.75 – 1	-0.7 – 0	$0.19 \pm 0.08 \pm 0.08$	1.2089
Δx	Δz	$R_{2\chi} \pm$ stat $\pm$ syst	$C_{R_{2\chi}}$
0 – 0.25	-0.7 – 0.7	$0.24 \pm 0.06 \pm 0.06$	0.1933
0.25 – 0.5	-0.7 – 0.7	$0.35 \pm 0.06 \pm 0.12$	0.3184
0.5 – 0.75	-0.7 – 0.7	$0.38 \pm 0.07 \pm 0.13$	0.3715
0.75 – 1	-0.7 – 0.7	$0.16 \pm 0.05 \pm 0.08$	0.3812

Table 7.1: Azimuthal correlations: the parameters R_χ and $R_{2\chi}$, obtained by a fit to the $\cos\chi$ distributions with the function of Eq.7.3, are given for the different x ranges together with statistical and systematic errors. The correction factors C_i, used to extrapolate R_χ and $R_{2\chi}$ to the full z range, are also given.

Additional sources of systematic errors complementing those already mentioned in Chap. 6 have been taken into account. We have tested the effects of the resolution on Q^2, x, z and χ on the fitted parameters R_χ and $R_{2\chi}$ by varying the shape of the distribution of each variable in turn, according to its resolution, in the Monte Carlo. In Fig. 7.5 the different resolutions are shown. A 8.2% relative deviation of R_χ and $R_{2\chi}$ has been observed and taken as systematic error. The transverse muon momentum resolution defined by [47]:

$$\frac{\sigma_{p_T}}{p_T} = 0.018 p_T(\mathrm{GeV}) + 0.02$$

produce a systematic deviation[2] on the ratios R_χ and $R_{2\chi}$ of $\pm 12\%$. A $\pm 4\%$ effect

[2]Note that in 1994 the Silicon Microvertex Detector become operational. The resulting improvement of the muon momentum resolution for the 1994 implies that the systematic effect quoted here is very conservative.

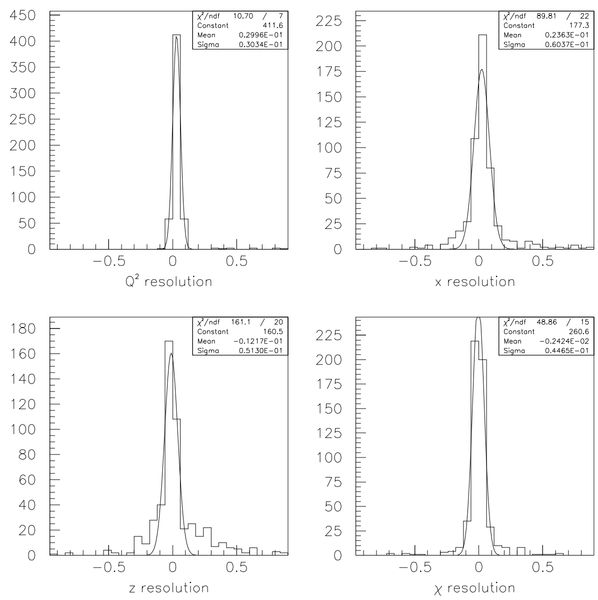

Figure 7.5: The Q^2, x, z and χ resolutions.

is due to radiative corrections. The effects of cuts on z and x have been found to contribute less than 3%. From the average deviation between the two correction methods, we deduce a systematic error of $< 1\%$ for R_χ and 13% for $R_{2\chi}$.

The experimental values of R_χ and $R_{2\chi}$ are given in Tab. 7.1 with statistical and systematic errors. The comparison with the QED predictions is shown in Fig.7.9. The measured values of R_χ and $R_{2\chi}$ are significantly different from zero and well compatible with the theoretical expectations. The dependence of the ratio $R_{2\chi}$ on the scaling variable x has already been measured by the OPAL [77] collaboration in a wider range of z, nevertheless since $R_{2\chi}$ depends on the cut applied on z, a correction factor is needed to compare these two measurements.

To extract the structure functions F_A and F_B from the measured values of R_χ, $R_{2\chi}$ and F_2^γ we have to extrapolate the measurement to the full z interval. A set of correction factors C_{R_χ} and $C_{R_{2\chi}}$ have been computed by numerical integration, they are also reported in Tab.7.1. The correction functions are shown in Fig. 7.6; the correction factors are the mean values of these functions inside the different x intervals.

The structure functions F_A and F_B are then extracted as:

$$F_A = \frac{1}{2} C_{R_\chi} R_\chi F_2^\gamma \qquad F_B = 2 C_{R_{2\chi}} R_{2\chi} F_2^\gamma. \tag{7.4}$$

The dependence of the structure functions F_A and F_B on the scaling variable x together with the QED expectations are reported in Fig.7.10. The value and x-dependence of the interference term of the longitudinal photon, measured by the structure function F_A, could be measured.

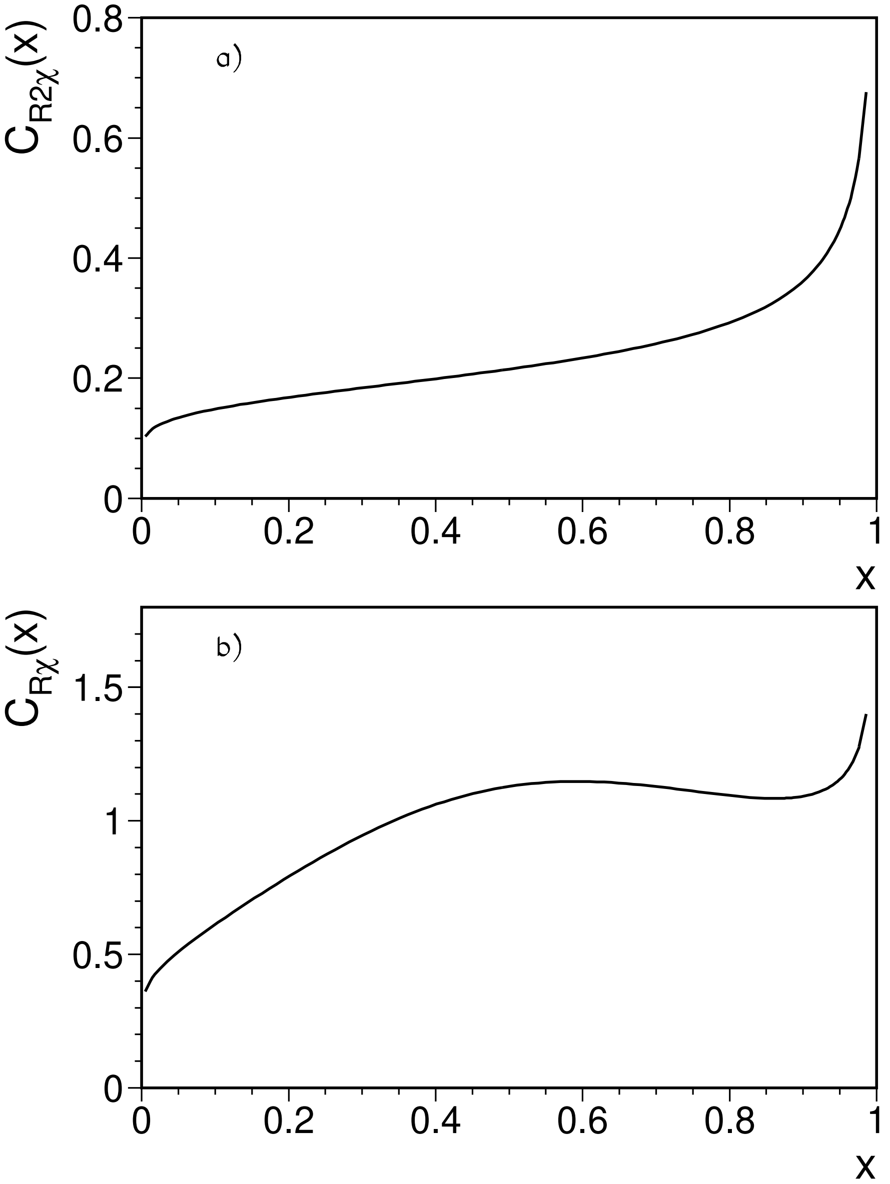

Figure 7.6: a) Correction function for $R_{2\chi}$; b) Correction function for $1/R_\chi$.

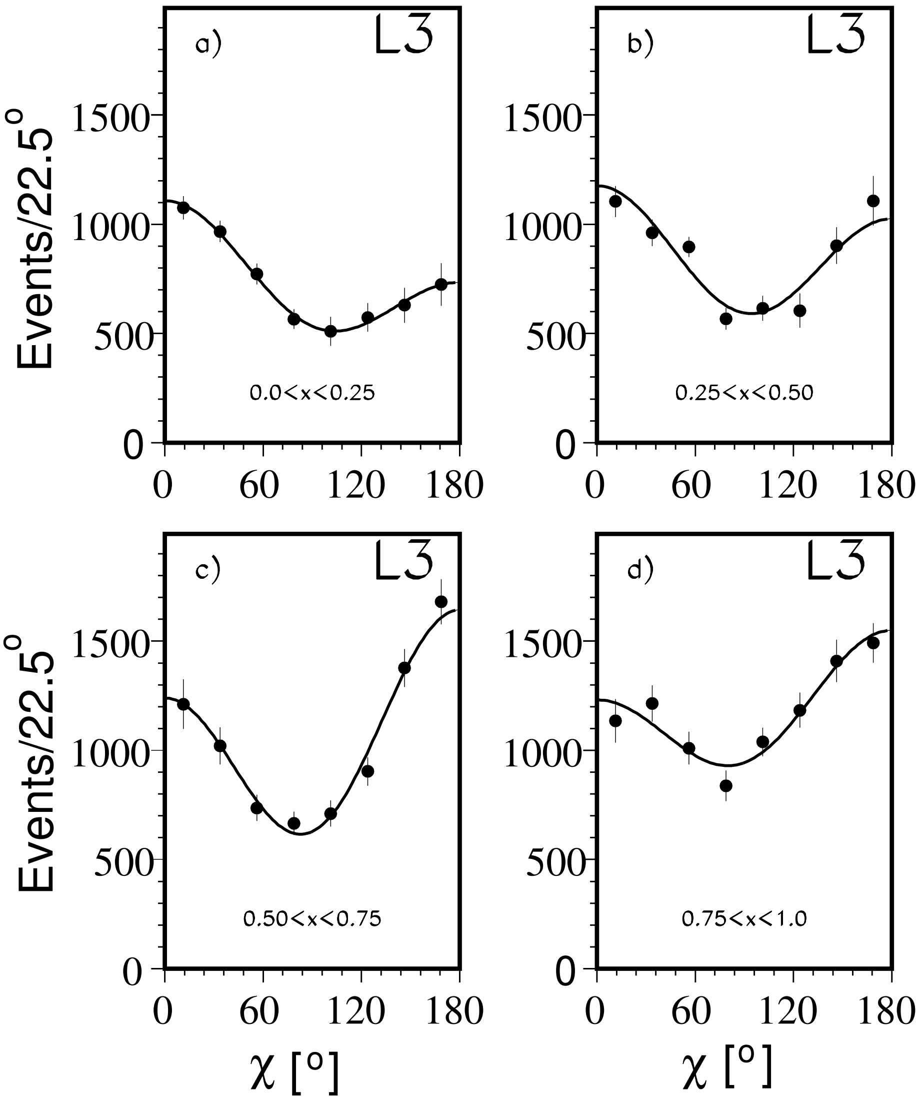

Figure 7.7: The acceptance corrected μ^- azimuthal distribution for $0.0 \leq z \leq 0.7$. The $z < 0$ sample has been added to the $z > 0$ sample using the transformation $\chi \longrightarrow \pi - \chi$. The fit of Eq. 7.3, which determines the value of R_χ in each x interval, is superimposed on the data.

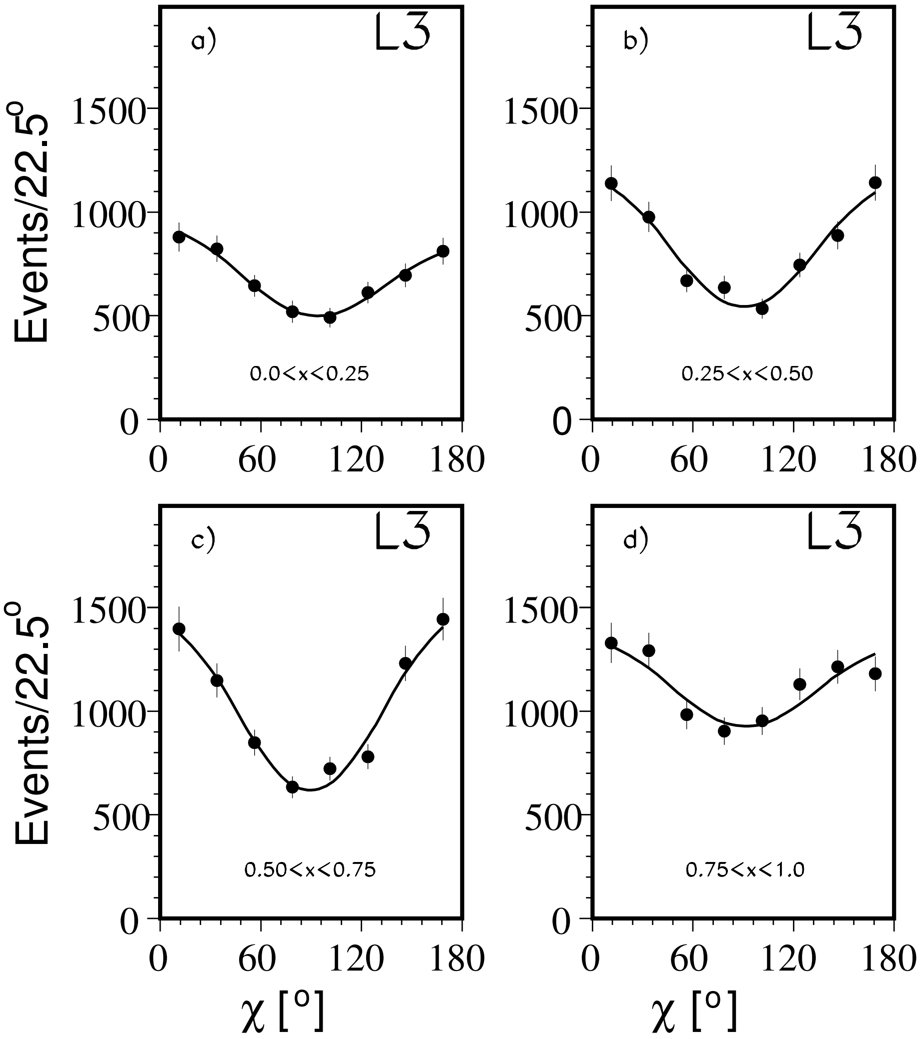

Figure 7.8: The acceptance corrected μ^- azimuthal distribution for $\mid z \mid < 0.7$. The fit of Eq.7.3, which determines the value of $R_{2\chi}$ in each x interval, is superimposed on the data.

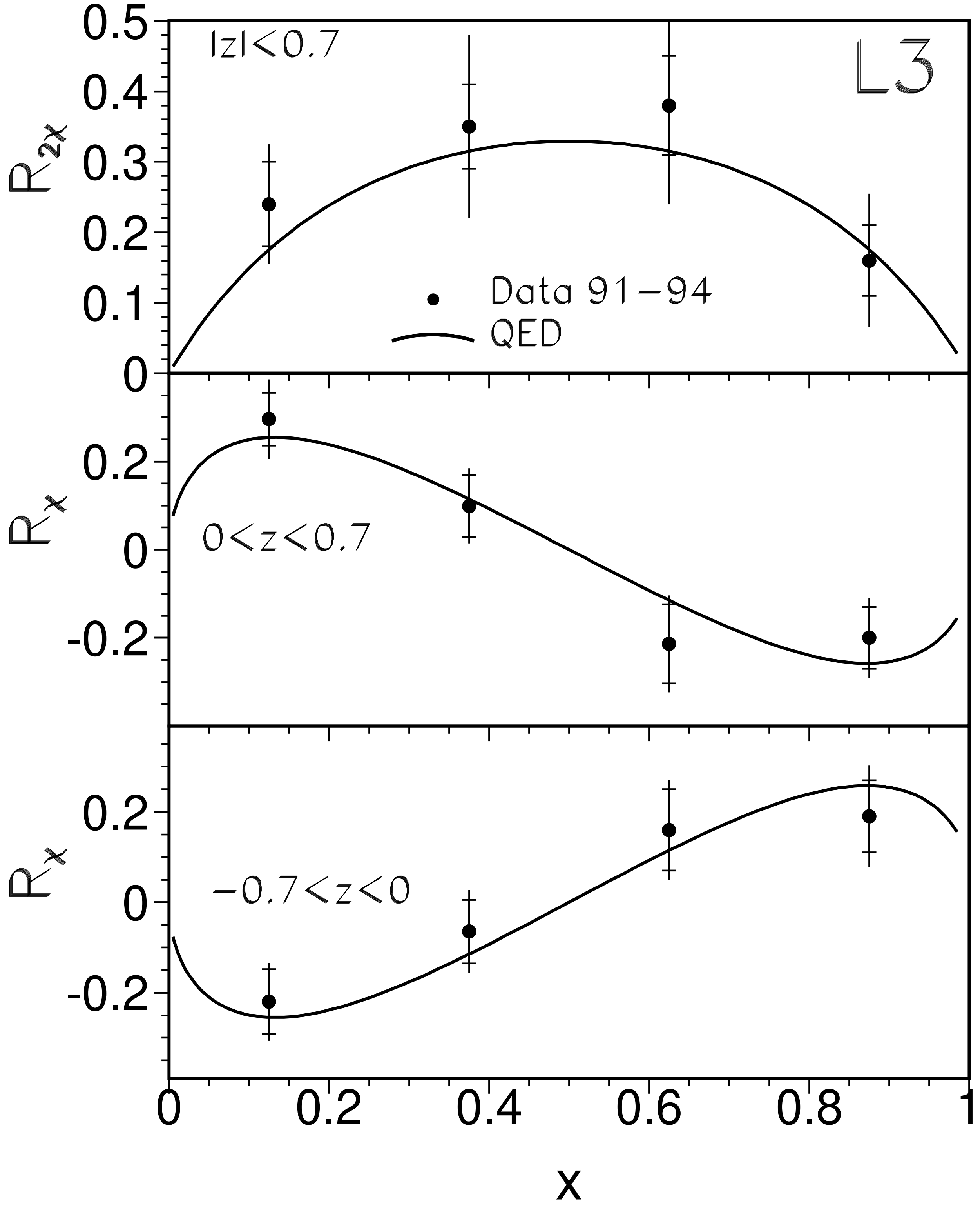

Figure 7.9: The values of R_χ and $R_{2\chi}$, measured in four x bins, are compared to the theoretical QED expectations. The outer error bars represents the sum, in quadrature, of the systematic and statistical (inner error bars) errors.

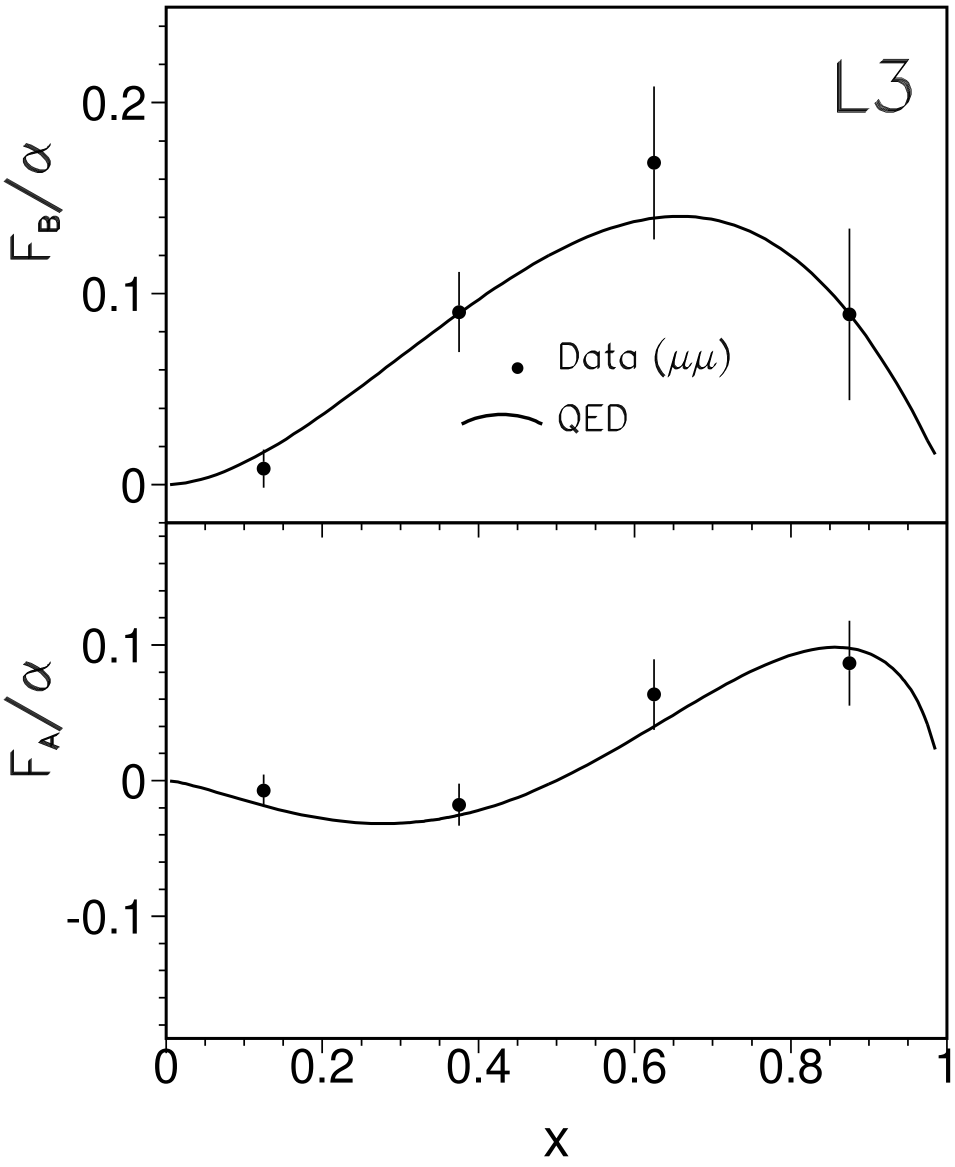

Figure 7.10: The structure functions F_B and F_A as extracted from the R_χ, $R_{2\chi}$ and F_2^γ measurements. The structure function F_A is the mean value between $F_A(z > 0)$ and $-F_A(z < 0)$. The errors are statistical and systematic added in quadrature.

Chapter 8

Conclusions

We have analyzed the cross sections of the tagged two-photon reaction $e^+e^- \longrightarrow e^+e^-l^+l^-$ $(l = e, \mu)$ at $\sqrt{s} \simeq 91$ GeV, using data collected by the L3 detector during the years 1991 to 1994 at LEP1.

In the channel $e^+e^- \longrightarrow e^+e^-\mu^+\mu^-$, by measuring the differential cross-sections $d\sigma/dxdQ^2$ in the Q^2 range $1.4 < Q^2 < 7.6$ GeV^2, we have extracted the leptonic structure function F_2^γ. The distribution of $F_2^\gamma(x)$ is significantly different from the analytical QED expectations if one neglects the virtuality of the target photon. By fitting the experimental data, the mean value of the target photon virtuality is found to be $t^2 = 0.033 \pm 0.005$ GeV^2. This result should be taken into account in studying the hadronic structure functions of the photon, the theoretical parameterizations of the photon parton density functions should take properly into account also the virtuality of the target photon. At LEP, the leptonic structure function F_2^γ has also been measured by OPAL [75] and DELPHI [76]. In particular, for a single tag configuration, DELPHI has studied the influence of the target photon virtuality on the determination on the structure function of the photon in a Generalized Vector Meson Dominance (GVDM) framework. They have estimated the effect to be at the 10% level. A compilation of the different F_2^γ leptonic structure function measurements [112] is shown in Fig. 8.1

The study of the azimuthal angle distributions of the μ^- in the $\gamma\gamma$ center-of-mass system has enabled the first measurement of the F_A and F_B structure functions.

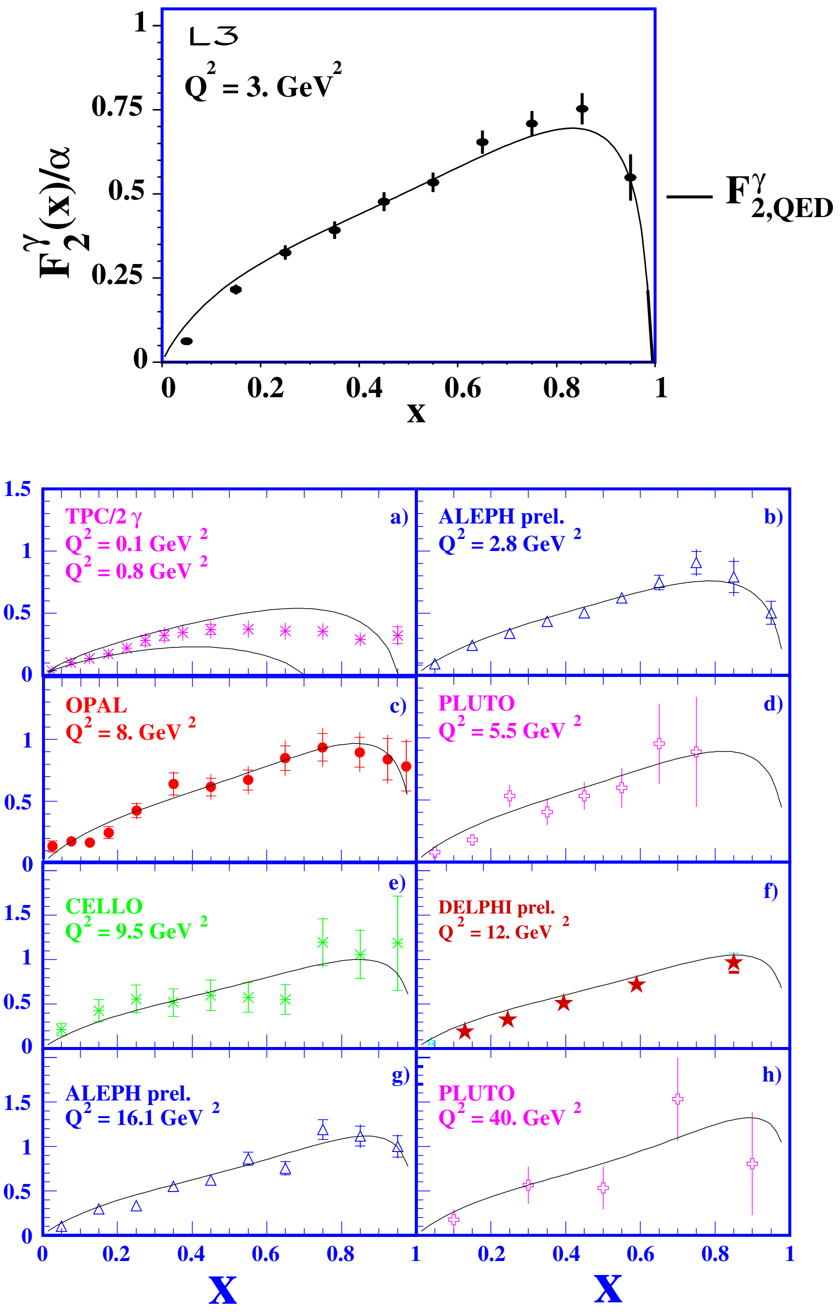

Figure 8.1: Compilation of the $F_2^\gamma(x)$ measurements in different ranges of Q^2. All results are according to expectations from QED.

Both originate from interference terms of the scattering amplitudes, F_A in particular is due to the interference between longitudinal-transverse and transverse-transverse photon amplitudes. From this measurement we can establish that the longitudinal photon structure function is significantly non-zero. The characteristic x dependence of the interference terms, predicted by QED, is well verified by the data. The good agreement obtained indicates that the tagging method and the strategies adopted to extract the structure functions of the photon are understood well enough to be used for QCD photon structure functions measurement at L3. At LEP, OPAL has also analysed the azimuthal correlations, extracting only the ratio $R_{2\chi} = F_B^\gamma/F_2^\gamma$. The corrected values of $R_{2\chi}$ are compared to OPAL results [77] in Fig 8.2. The luminosity and the high energy available at LEP2 make it possible to undertake quantitative tests of QCD. Especially, measurements of the real-photon structure function $F_2^\gamma(x)$ can be done down to $x \simeq 10^{-3}$ allowing to test the universality of the rise of the proton structure function $F_2^p(x)$ at small x observed at HERA [113, 114]. Moreover the measurement of $F_2^\gamma(x)$ at small x will help to provide valuable constraints on the parton densities of the photon in a region where they are dominated by their hadronic component (Vector Meson Dominance). In this kinematical region, precise measurements will help to discriminate between the various parameterizations of the photon structure suggested so far (e.g. Levy-Abramowicz-Charchula (LAC1) [115], Duke-Owens (DO) [116], etc.). Few experiments have already produced some results in this domain [117, 118, 119, 120, 121]. Nevertheless, those results are affected by large systematic errors and new independent measurements with improved statistics and systematic will help to discriminate between the different parameterizations.

Even though there is no prospect to measure the longitudinal structure function of the photon at LEP2, we have shown that related structure functions can be obtained from the study of azimuthal correlations. Our leptonic case can be generalized to an hadronic configuration by analyzing the angular correlations between the tagged electron and an outgoing inclusive hadron or jet. However, in the hadronic case, additional problems are brought by the fact that the hadronic final state must precisely be reconstructed which renders unfolding techniques unavoidable. Nevertheless, as shown in Fig. 8.3 , Monte Carlo simulations have shown that it seems hopeful that

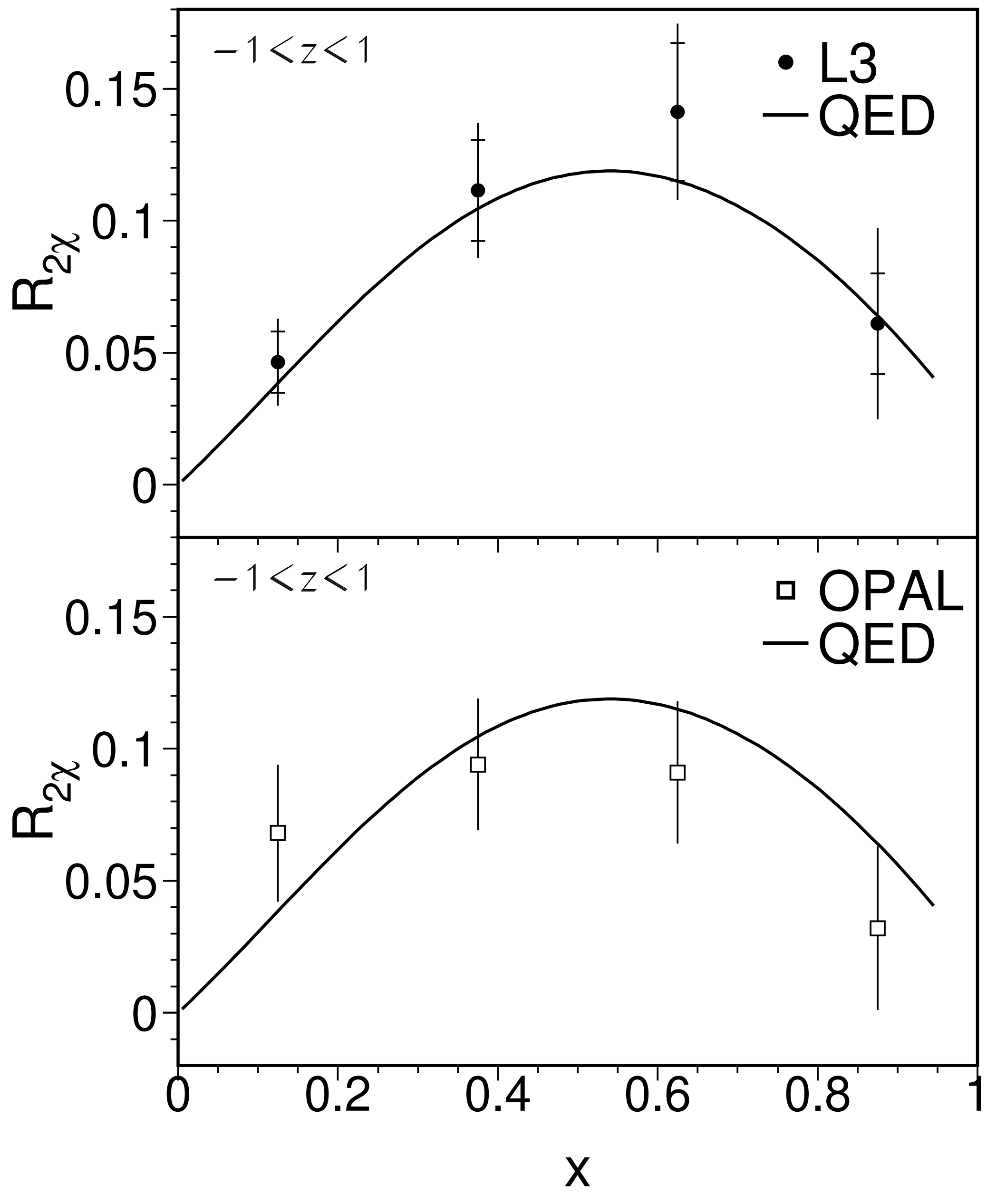

Figure 8.2: $R_{2\chi}$ corrected for the z cut (top) compared to the OPAL results (bottom).

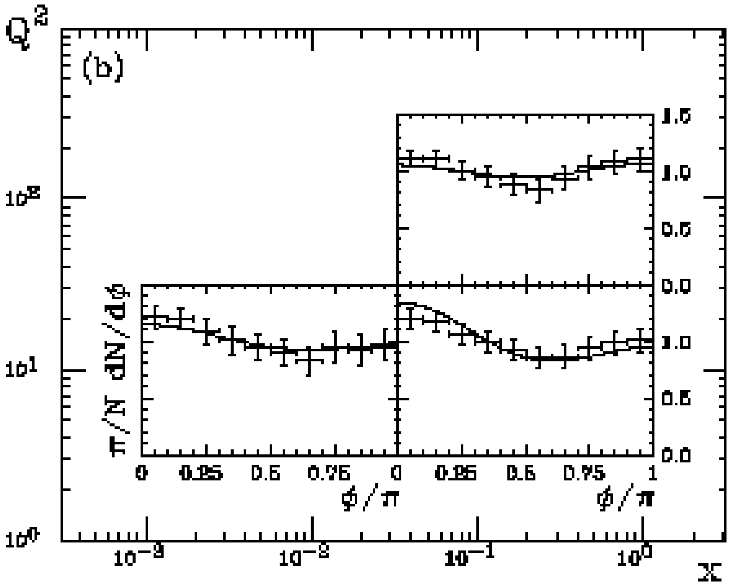

Figure 8.3: Distribution of azimuthal angle of the more forward jet in two-jet events. The figure depicts generator-level results in different x and Q^2 domains. They have been obtained assuming an integrated luminosity of 500 pb^{-1-1} at LEP2. Those results have been obtained from [10].

the measurement can be done at LEP2.

Finally, the low angle tagging capabilities of the L3 detector have been enlarged by the adjunction of a Very Small Angle Tagger (VSAT) and by equipping the Active Lead Rings detector with a dedicated trigger. This gives the possibility to study two-photon reaction over a wider range of momentum transfer Q^2 allowing to analyze in more details effects of a non-zero virtuality of the target photon.

In this thesis, we have developed and analyzed new methods to extract additional information on the structure of the photon. As well as being of interest in their own right, we hope that the results presented here and the improved unfolding methods will helps the investigation of the hadronic structure of the photon in the near future.

Appendix A

The ALR Upgrades: Technical Addendum

A.1 Introduction

The Active Lead Ring (ALR) calorimeter, which is a lead-scintillator sandwich, has been mainly used in the single-photon analysis, as a passive detector for vetoing purposes. The ALR detector cover the forward and backward region between 3.9^o and 8.67^o of the L3 detector, as described elsewhere [5, 40]. Originally the ALR where installed to protect the inner tracking chamber from stray background particles. Instrumenting the lead material with plastic scintillator allowed us to use them improving the hermeticity of the whole L3 detector. It should be mentioned that the electronics described here allows to make a trigger (analogous to the ALR one) also using logic signals coming from others detectors. This has been done for the Very Small Angle Tagger [122].

The present work has been done to use the ALR as an electron tagger and beam background monitor at LEP II by extending to the ALR, the existing triggering system of the Luminosity Monitor [123, 124].

A.2 The ALR Detector

A detailed description of the ALR detector (Fig. 3.19) can be found elsewhere [125, 40]. The ALR is a sampling calorimeter which consists of sandwiches of lead and plastic scintillators arranged in a tower module. Each tower consists in 5 BC408 [126] scintillator layers 10 mm thick alternatively placed behind lead converters (Fig. A.1). The thickens of each lead converter has been optimized to give the best electron/hadron (e/h) response. Three scintillator layers have a segmentation in the azimuthal angle ϕ (16 ϕ-scintillators) and the remaining two, placed near the expected electromagnetic shower maximum at 45 GeV, have a segmentation in the polar angle θ (5 θ-scintillators). This configuration allows an angular resolution of 0.45 degrees in theta and 2.7 degrees in phi (FWHM). The scintillators are read out at their outer edge by photo-diodes of dimension 10x20 mm^2.

The original feature of the ALR calorimeter is that the optical read-out of the scintillators is directly performed by silicon PIN photo-diodes [127, 128]. This is very useful in situations where severe space limitations and the existence of a magnetic field exclude the use of bulky devices as photomultiplier tubes. With this setup we obtain an energy resolution for electromagnetic showers of 15% at 45 GeV.

The rise time of released signal is largely determined by the scintillating time $\simeq 10$ ns [125, 40]. Since LEP II machine can operate with trains of closely spaced bunches, it is important, for noise rejection and to study the trigger efficiency for different bunches, to tag the bunch which produces the triggered event. Using the fast rising edge of the signal coming from scintillators we are able to perform this operation.

The triggering system has been implemented using the signal released by the ϕ-scintillators since their geometrical shape allows a large light yield (3000 e/MeV) reducing the influence of the electronic readout noise on the final trigger decision.

A.3 Physics Motivations

The main physics domain for which this trigger has been designed is the tagged two-photon collision where a scattered electron is detected in the ALR and the reaction products of the photon-photon collision are detected by the central detector (barrel and/or endcaps). An homogeneous acceptance in Q^2 of the L3 detector gives an important tool to measure the real Photon Structure Function (PSF) and much of our efforts go in that direction. The PSF, as well as being of considerable interest in its own right, as a test of perturbative QCD, is an important complement to the experimental measurement at HERA of the gluon structure function of the proton. During the LEP running period at the Z peak the ALR has been used as a passive detector leading to a hole (Fig. A.3) in the determination of the Q^2 distribution since, without a trigger, no reliable information can be extracted in the angular region covered by the ALR. Without a devoted trigger, tagged two-photon events in the ALR can only be recovered using the central tracker (TEC) trigger which requires back-to-back tracks within a cone of 40 degrees. The contribution of the TEC trigger on the whole sample of $\gamma\gamma \longrightarrow \mu^+\mu^-$ events with a tag in the Luminosity Monitors, where a tag trigger is operational, is shown in Fig. A.2. A uniform coverage can only be achieved with a total energy measurement in coincidence with a track detection.

Another important motivation to trigger on the ALR is given by the monitoring of TEC background at angles larger than currently provided by the Luminosity Monitor. The radiation damages induced on the ALR by the particle fluence during the filling operation of LEP being negligible, this detector, once equipped with a trigger electronics, can be used as a full time monitor of the beam conditions. To be able to monitor any change in the beam conditions as function of the number of bunches inside a bunch train, a time sensitive bunch tagging has been developed. Since the number of bunches inside a bunch train may vary, we have designed a flexible logic for the bunch tagging and at any time we are able to adapt our electronics to the LEP working configuration.

A.4 Simulations

The aim of the simulations was to check the detector response and to help to the design of the new trigger.

We used Geant version 3.15 [129] with the correct specification of gazes involved in the detector. As already said, this detector is made of seven layers of lead and five layers of scintillators (2 C_1,C_2 in θ and 3 S_1, S_2,S_3 in ϕ) for a total radiation length of 22 X_0. The ϕ layers are rotated by 7.5^o with respect to each other. The polar angle θ was simulated in the range (4.7^o,9.3^o) (which corresponds to the ALR detector position) whereas the whole azimuthal angle was simulated.

Focus has been put on the ϕ study and the simulations have been done with a uniform distribution in θ. As the system is symmetric, we only considered half the detector which corresponds to simulate the response of $3\times16 = 48$ channels.

A.4.1 Deposited energy and acceptance

The simulations consisted to decide how to sum the different channels in order to register the maximum of the deposited energy from the electromagnetic shower. The best result has been observed by a summation of two-by-two channels after summing 1/16 particular sector on the three layers.

Simulations of total deposited energies in the three ϕ layers of scintillators have been performed for electrons of different incident energies. Table A.1 shows the deposited energies as a function of the incident electrons energies with the corresponding resolutions.

To simulate the acceptance for the trigger, each channel is defined to be the sum of the three scintillators of a given sector and added to its neighbor to form a trigger channel. Figure A.4 shows the summation of two neighbor channels. This summation choice has been decided with the argument that almost the total electromagnetic jet is included in only two sectors. The top graphic in the figure A.5 shows for 60 GeV incident electrons, the deposited energy in the two first channels, and the bottom one proves that the lost of energy due to the rotation of layers is given back by the addition of two neighbor channel. With the same argument, one can easily see that taking into account the hole azimuthal angle (summing two by two the channels), at least one trigger channel contains the total energy of the shower affected only by a minimum likage.

We also studied the effect on the deposited energy due to finite acceptance of the detector in θ angle. The simulations have allowed us to study the detection acceptance at small or high θ angles as a function of the electron energy.

A.5 Trigger Functions

The basic idea has been to extend the triggering system existing for the Luminosity Monitor ([123, 124]) to the ALR. Our aim was to insure to the L3 detector an homogeneous polar angle coverage for tagging high energy electromagnetic showers without modifying the existing electromagnetic trigger. The triggers provided are on single high energy deposit (single tag), or a double high energy deposit (Bhabha) or at least one high energy deposit in the ALR in coincidence with a presence of a track in the central L3 track detector (Gamma-Gamma). The two former triggers will be mainly used to analyze the noise coming from physical background and to estimate random coincidences with the TEC track signals. Moreover, the recent LEP 1.5 running mode has shown different behavior from bunch to bunch inside a bunch train showing the importance of a bunch tagging capability.

Since a sizeable contribution to the trigger rate is due to the off-momentum electrons, we have analyzed the beam-gated events sample. By off-line simulation of the trigger output, the beam-gate events study shows that an 8-bit prescaler (i.e. maximum prescaling factor of 255) is sufficient to keep the trigger rate lower than 0.3 Hz which is a necessary condition to uphold the overall efficiency of the L3 data acquisition.

As said in the previous chapter, the expected response in the trigger chain has been simulated using GEANT including half detector (one side) with 7 lead layers, 5 scintillator layers (2 θ scintillators layers0 and 3 ϕ scintillator layers) and aluminium boxes surrounding the scintillators. Given the geometrical acceptance of the ALR, simulations and studies on real beam-gated events allow us to define the needed sensitivity of the trigger electronics to have a uniform trigger response on the angular gap covered by the ALR. Simulations have shown that even if the ϕ-scintillators do not cover completely the lead plates, events arising in the gap without ϕ-scintillators can be recovered from the produced shower (Fig. A.6).

The sensitivity on the the minimal polar angle for a given threshold has been studied. The dependence of the theta minimal on the incident electron energy, which is found to vary between 4^o to 4.5^o, is shown in Fig. A.7. At the LEP II energies scattered electrons in ALR can be observed down to 4 degrees thanks to the shower development which allows a signal detection in the lower edge of the scintillators located at a polar angle of 4.5 degrees.

Table A.2 shows the energy detection (MeV) in each ϕ-sector of the detector. In order to contain all the shower in a single trigger channel we operate as follows: for each sector the contribution of the three layers is analogically summed and the result is added to the analog sum of the adjacent sector. This lead to a system of 16 channels in each ALR allowing to concentrate in at least one trigger channel all the energy released by the event. In this way the edge effects at the interface of two sectors can be avoided and a good uniformity in the azimuthal angle acceptance restored.

During the upgrade of the ALR an additional very forward-backward detector has been added to L3.

The Very Small Angle tagger [122] (VSAT) is an electromagnetic calorimeter which covers the angular region: $4.6 \leq \theta \leq 10.2$ mrad. Thanks to the extreme versatility of our electronics we have been able to include the VSAT information in the trigger decision. This facility and the new trigger gives to the L3 detector a new powerful device to investigate the two-photon process.

A.6 Logic & Design

The former inspection of the signal yield drove our trigger design. The measured light yield of the ϕ-scintillators is of $\sim$ 3000 electrons/MeV and the charge preamplifiers connected to the photo-diode/scintillator system give $40 \cdot 10^{-3}$ μV/electron. Since a 20 GeV electron is measured to leave about 600 MeV in the ALR, the corresponding signal size is at least 72 mV ensuring a sufficient sensitivity for the trigger. Much of our efforts have been devoted to keep the quality (time scale and amplitude) of the analog signal at the charge preamplifiers output along the driving distance of 60 meters necessary to reach, from the ALR location, the nearest accessible zone where all the processing electronics is located. The receiving task is performed by a MAX436.

A.6.1 Level-1 upgrade and driver receiver modification

The electronic chain associated with the detector consists of PIN photo-diodes followed by charge amplifiers [130]. The typical rise-time of the charge-amplifiers is 20 ns. This feature, allowing the bunch tag, is conserved by our front-end electronics which has been designed using the new LM6181 [131], which is a high speed current feedback amplifier with a slew rate of 2 V/ns, a settling time of 50 ns for 0,1% and working within an interval fully compatible with our signals. The same amplifier is also used to perform the analog sum of the three consecutive scintillator layers and amplify the result by a factor of 7.2. To drive the signal, we have chosen the MAX435 [132] driver which is a wideband transconductance with true differential high-impedance inputs. The 800 V/μs slew rate, the bandwidth of 275 MHz and the 1% settling time of 18ns to a 0.5V step input make this device ideal for our purposes. The measured time needed to bring the signal from the input to the driver output is 15 ns and the signal's slope is totally conserved. It is also possible to amplify the signal at the driver output in order to take into account the attenuation of the 60 meters of cables used to bring the signal from the detector to the blockhouse.

A.6.2 The Trigger System

The trigger electronics is located in the blockhouse i.e. in the accessible zone nearest to the detector. Here 32 signals (16 from e^+ side, 16 from e^- side) are received and processed by the trigger electronics. The system has been build in CAMAC. We have 8 processing modules called RECEIVERS (4 modules for e^+ side channels and 4 for the e^- side) each one of them handles 4 input-channels. They are all connected in daisy-chain and the digitized data is then processed by the CONTROLLER module which generates the trigger signals and communicates with a multiplexer module which is a buffer insuring the communication between our subsystem and the LEVEL-2.

The Receiver Module

Each receiver module has three different tasks. The first one is to receive the signal and split it for the background monitoring and for the trigger himself. The incoming signal devoted to the trigger is then sent in parallel to the bunch tagging subsystem and to the integrators.

1. INTEGRATOR modules integrate the signal over a gate defined by the CONTROLLER (FIG. A.8). The gate length is 3.5 μs, 2.5 μs corresponding to the time duration of the signal and 1 μs which corresponds approximately to the length of a bunch train. The choice of such a gate makes the integrators output independent of bunch number. It allows also to eliminate, by time averaging, high frequency noise ($\nu_{noise} > 100\ kHz$). The integrator output is digitized by an 8-bit ADC working in a voltage window defined by two references V_- and V_+ set by the user. In this way we are able to subtract pedestals and to set the working range $V_+ - V_-$ equal for all the channels. We then sum adjacent channels (1+2, 2+3, ..., 16+1 and the same for the other side channels 17 to 32). The full integration time is 5.3 μs (Fig. A.8). After this delay the CONTROLLER module starts to send the first words to the multiplexer. Those results are then used for any monitoring task as well as for the fine tuning of

the trigger. Special pedestal runs are scheduled to implement in the initialization the value of V^- for all the ADC's while the value of V^+ has so far been defined by simulations and needs to be tuned during the first period of run.

2. The bunch tagging is performed with the help of discriminators. The rising edge of the discriminator output produces a pulse of tunable length. The use of discriminators imply that the arrival time of the pulse is strongly correlated with the amplitude of the signal. Moreover, the analog signal coming from the experiment is distorted by the 60 meters of cable needed to bring it to the blockhouse. To minimize all these effects the following procedure has been applied:

   To detect a bunch the closing edge of the discriminator's pulse must fall inside a 200 ns gate given by the controller and associated with a given bunch. In order to avoid multiple bunch tagging, we keep the discriminator blocked for 3.5 μs to eliminate fake tagging due to possible electronic noise when the signal crosses for the second time the discriminator threshold. After the 60 m of cables, the rise time of the signal pulse in the blockhouse is 130 ns. This requires a 200 ns long gate to detect the bunch. In Fig. A.9 we show an example of an event in the first bunch. S1 is the discriminator output. It produces the signal S2 of a tunable length. The coincidence between the closing edge of S2 and the bunch tag gate of the bunch pattern is the signature of a tagged bunch. The bunch number is given by the gate number inside the bunch pattern.

A.6.3 The Controller

All the INTEGRATOR results are mastered by the CONTROLLER which is a multiple function module. It contains the timing circuits allowing, from the T_0 (or bunch crossing signal), to set the gate for the integrators. It provides also the 4 time windows of the bunch pattern used for the bunch tagging as well as the strobe signal used to send data to a multiplexer insuring the communication with the whole L3 data acquisition. All the logic for the trigger is implemented in this module and finally the CONTROLLER insures the data transfer to the MMB's.

1. **The timing sequence**

   The timing sequence starts with the arrival of the bunch crossing signal which resets all the buffers and enables the CAMAC output of this module. In the front panel it is possible to tune the delay between the T_0 and the integration gate. The modification of this delay changes of the same amount all the following time signals. This facility is used to align the incoming signal to all our timing scheme. This is done, in the first run period, by the help of a *Time to Amplitude* converter and a *Multi-Channel Analyzer* allowing to establish an online "arrival-time" histogram based on high energy events. Events belonging to the first bunch must be aligned $\simeq$ 200 ns after the opening of the gate, to ensure bunch tagging with high efficiency.

   The minimal time required to process the analog signal by the multiplexer is 5.3 μs (see Fig A.8), 5.3 μs after the T_0 the CONTROLLER starts to write the energy information for each channel to a multiplexer [123, 124] insuring the communication with the L3 data acquisition. The buffer of the multiplexer is piloted by a strobe signal generated by the CONTROLLER.

2. **The trigger**

   A set of 4 programmable 8-channels comparators are used to build a set of logical signals used for the trigger. All the energy informations from the INTEGRATORS are stocked in a temporary buffer and sequentially sent to the comparators. Since the Bhabha (BH), Single Tag (ST) and Gamma-Gamma (GG) trigger rates can have different sensitivities to the beam background, the threshold of the comparators, set by a CAMAC function, is independent for each of those sub-triggers. The set of the comparator results, one for each physical ALR trigger channel, is used by the trigger logic. The "*AND*" of the 32 channels gives the ST trigger, a coincidence between the e^+ and e^- sides gives the BH trigger. The GG trigger is made by the coincidence between at least one energetic deposit in one ALR channel and at least one track detected by the L3 central tracker. The information of the number of tracks is sent to our trigger by the electronic devoted to the central tracker and reach the controller module 9.6 μs after the T_0. The final result in the L3 trigger mask is the logic "*OR*" between BH,ST and GG. A particular attention has been devoted to keep the trigger rate lower than 0.4 Hz in order to avoid damages the L3 data acquisition efficiency. A natural limit on the GG trigger rate is set by asking a coincidence with a track in the central tracker and an additional rejection can be performed rising the comparator threshold for the GG trigger. To prevent a possible high rate coming from ST and BH triggers, we have inserted an 8-bits prescaler on those two triggers allowing a maximum rejection of 255. By carefully tuning the thresholds and the prescaling factors we had, during the first period of running of this trigger a stable configuration.

A similar logic configuration has been added to handle the incoming digital signals from the VSAT. The triggering logic on the VSAT, done by the CONTROLLER, is done by doubling the logic setup of the ALR trigger. A BH, ST and GG triggers are thus also implemented for the VSAT. The only security is that we add an ON/OFF programmable switch. The VSAT being very close to the beam pipe, its trigger rate may evolves dramatically with the beam background conditions. The switch allows a fine tuning of the VSAT trigger parameters without affecting the normal efficiency of the rest of the system.

3. **The monitoring**

In order to have a continuous off-line monitoring of the trigger status, all the needed information is sent to the L3 data acquisition. A pattern of 40 words of 16-bits is recorded for each L3 triggered event. The first 32 words corresponds to the 32 ALR trigger channels and contains the energy information (on nine bits) the overflows (on one bit) and the bunch tagging status (a maximum of 4 bunches per train is allowed and encoded on four bits). The trigger information of the ALR trigger is encoded on three bits of the 35^{th} word and the VSAT trigger information is encoded on three bits of the 36^{th} word. The remaining words are empty and we keep them as a free space for any possible future upgrade of the system.

A.7 Performances

The final trigger configuration has been installed during the 1995-96 shutdown and the running period "a" of LEP has been used to tune and debug the system. Since the ALR are read out in two parallels ways: the data acquisition line (DAQ) and the trigger read out, this gives a powerful way to check the functioning of the trigger. The Fig. A.10 shows the good correlation between the reduced energy from the DAQ (deposited MeV) ad the trigger line result (ADC). The sharp pick is due to the threshold effect while the bump at 2000 MeV is identified with Bhabha's events. Furthermore the analysis of the mean energy per scintillator (E/pp) in the e^+ and e^- sides of the detector allows to separate the Bhabha's events as shown in Fig. A.11.

A calibration factor for each channel can be obtained by computing the mean value of the ratio between the trigger output and the DAQ data. A quite uniform behavior is found as shown in Fig. A.12. This help us to place the different triggers thresholds at the needed energy value.

The contribution of the all sub-triggers to the final energy distribution of the ALR events is shown in Fig. A.13. The pick due to the threshold effect is clearly visible and mainly affect the GG and ST triggers which requires only one bump in the ALR. The threshold is well below the Bhabha's energy.

A.8 Conclusions

A performing simple trigger have been designed and realized. First test shows the working capabilities of the system and the first Bhabha's have been recorded from the ALR detector. The system has been conceived to be as compact and as simple as possible. The versatility of the concept allows us to add or modify the system with minor changes, as we did in including the VSAT in the trigger decision. More work in calibration is still necessary to uses the full range of capabilities of this detector.

	Incident electrons energies					
	5 GeV	20 GeV	30 GeV	45 GeV	60 GeV	90 GeV
Deposited energy (GeV)	0.114	0.417	0.610	0.886	1.147	1.672
Resolution (GeV)	0.042	0.151	0.223	0.331	0.444	0.654

Table A.1: Simulations: Deposited energies in the three layers of scintillators

LAYERS	ϕ-SECTORS (Deposited energy in MeV)						
	sec.1	sec.2	sec.3	sec.4	sec.5	sec.6	...
ϕ_1	0.00	0.00	7.20	148.1	0.00	0.00	...
ϕ_2	0.00	1.10	20.4	719.5	2.90	0.00	...
ϕ_3	0.00	11.9	433.2	143.2	0.00	0.00	...

Table A.2: Typical energy deposition in the scintillator sectors for a 45 GeV electron. The contribution of the tree scintillator layers shows the development of the electromagnetic shower.

First studies on tagged two photon physics, where the tagged electron belongs to the angular range covered by the ALR, are on progress.

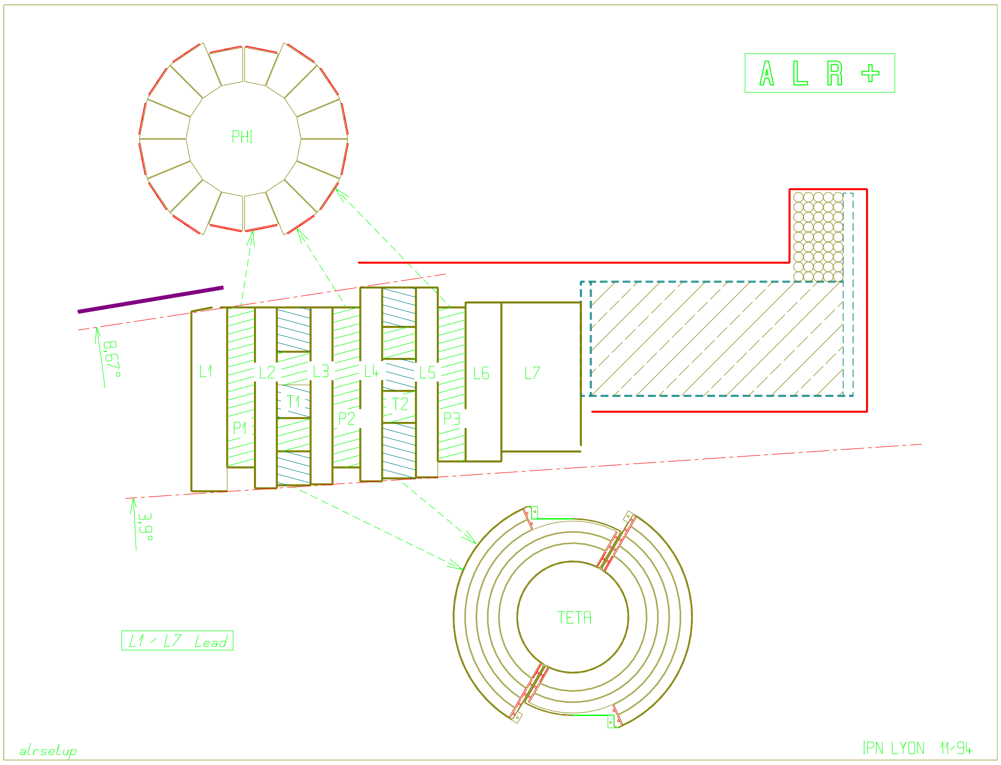

Figure A.1: The ALR configuration. Layers P1 to P3 are ϕ-scintillators while layers T1,T2 are Θ-scintillators. Each scintillator is embedded in two lead layers (L1 to L7).

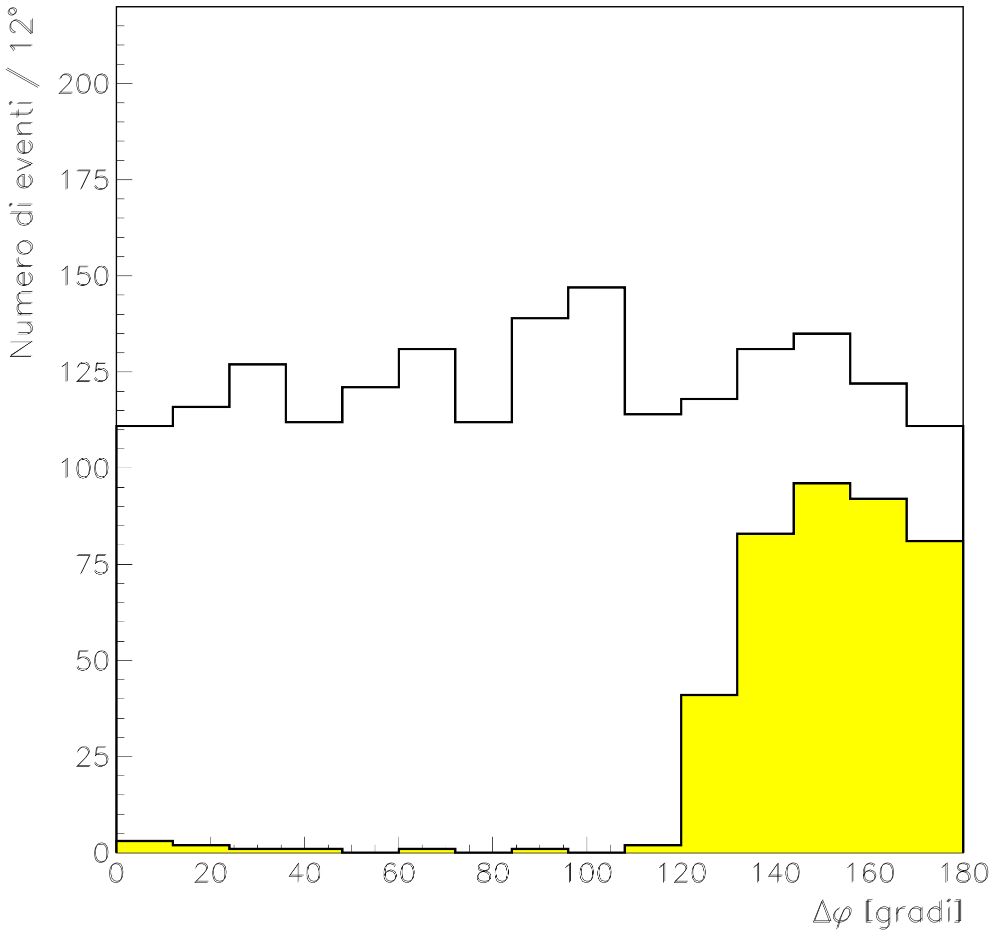

Figure A.2: $\Delta\phi$ distribution for $e^+e^- \longrightarrow e^+e^-\mu^+\mu^-$ events with a tag in the Luminosity Monitor (tag angle between 27 and 64 mrad). Shaded histogram starting at 120^o corresponds to the $\Delta\phi$ distribution for TEC triggered events. The uniform $\Delta\phi$ is obtained with a Luminosity Monitor based trigger.

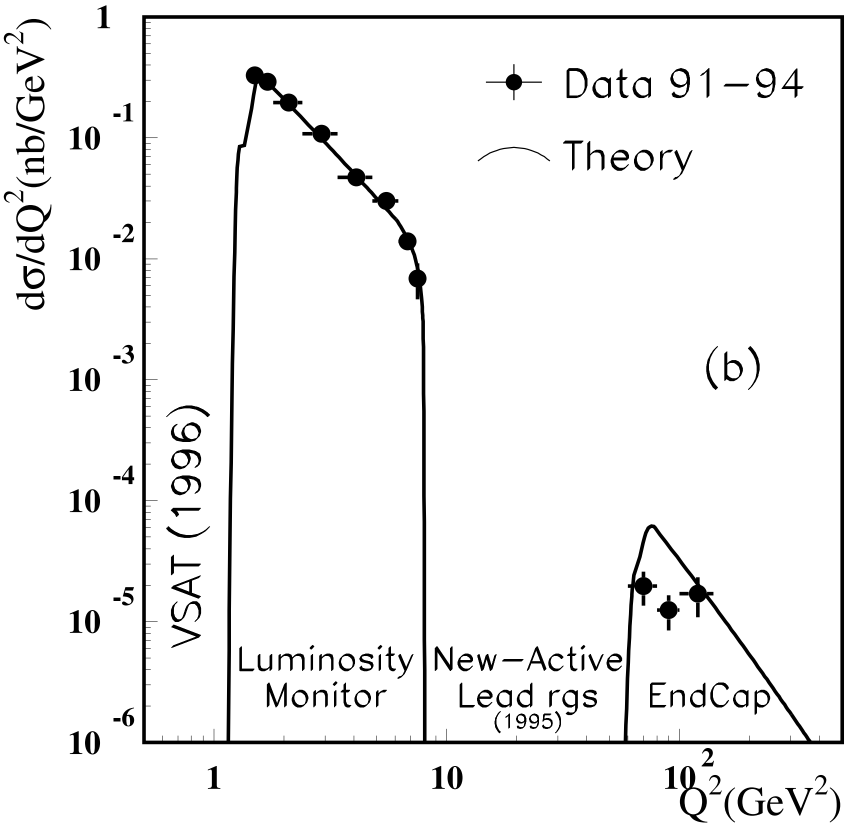

Figure A.3: $\frac{d\sigma}{dQ^2}$ distribution from 91-94 L3 data (from *DIS '96* G.F. Susinno's talk). The big gap is due to the absence of precise information coming from the ALR. Our upgrade will allow to have an uniform coverage in Q^2.

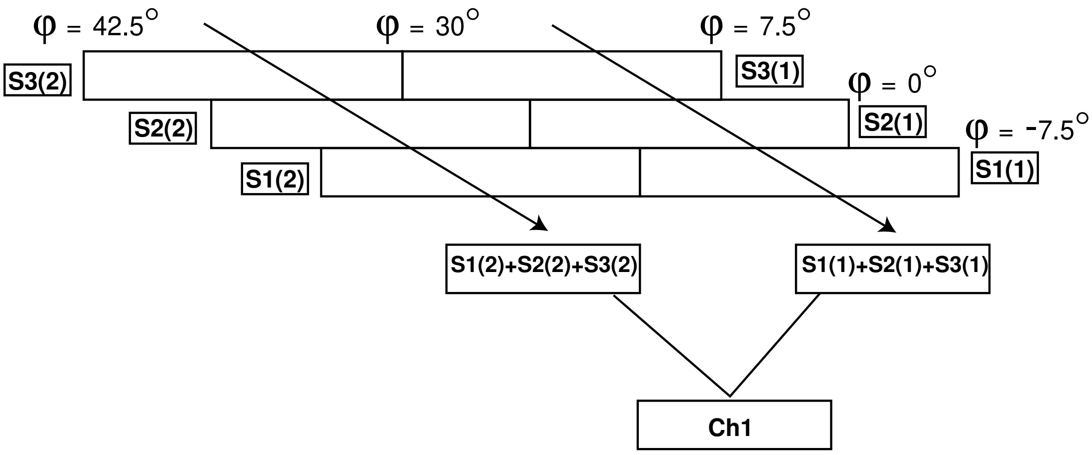

Figure A.4: Summation of two channels

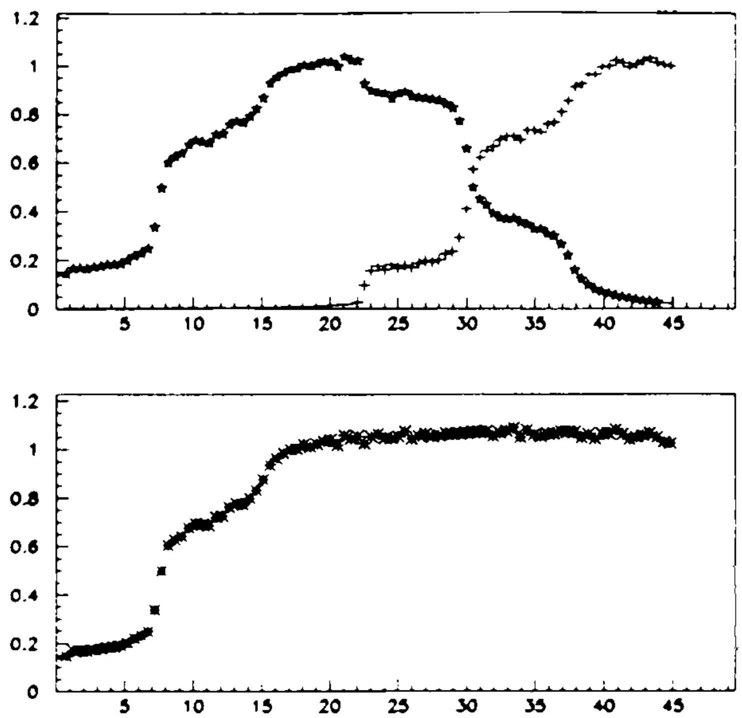

Figure A.5: Benefit of summing two neighbor channels: deposited Energy (GeV) as a function of the ϕ angle

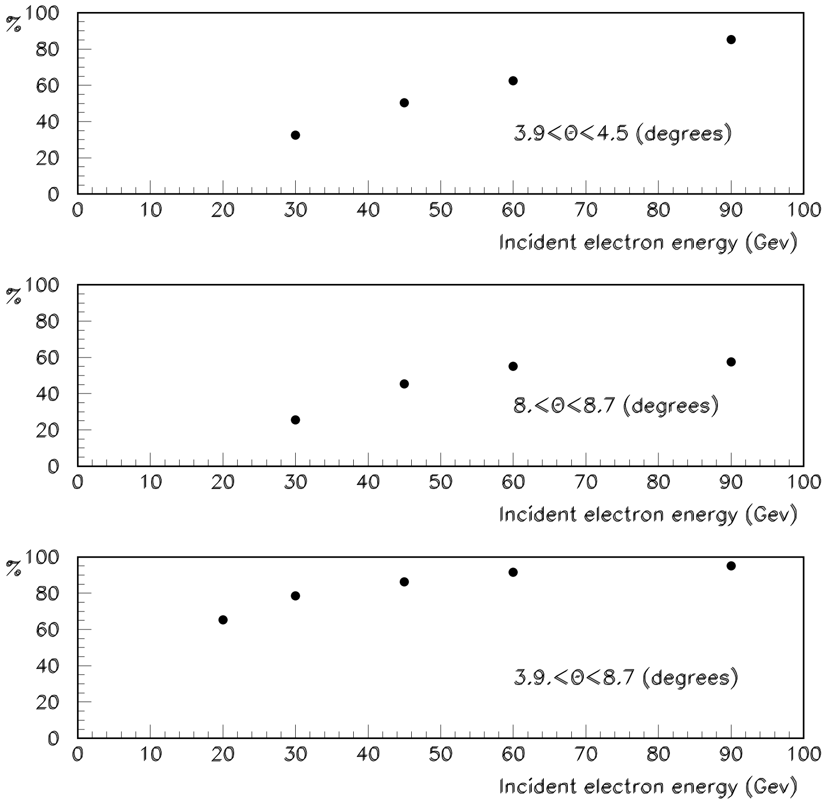

Figure A.6: Acceptance (ratio between the number of simulated events producing a trigger over the total number of generated events) for different studied angles as a function of incident electron energy. The first two plots show the acceptance at the edges of the detector while the last plot shows the overall acceptance.

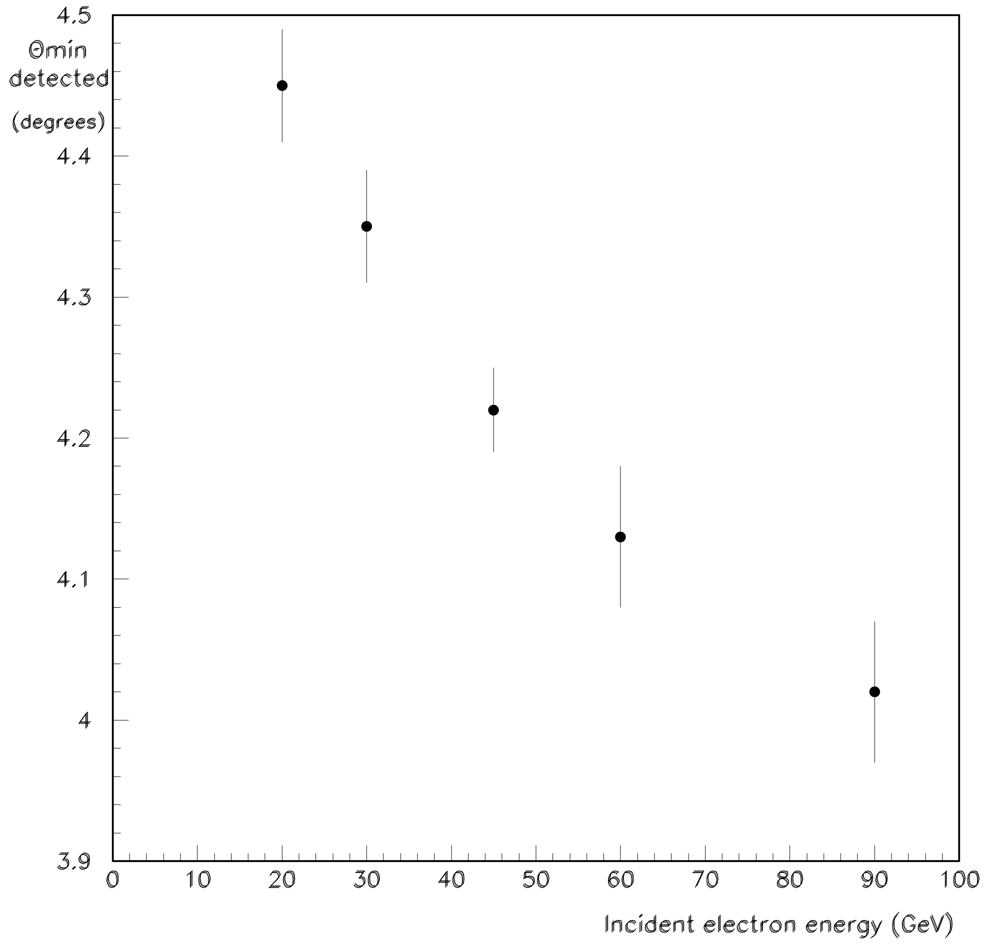

Figure A.7: θ minimal detected. Points corresponds to a 95% detection efficiency.

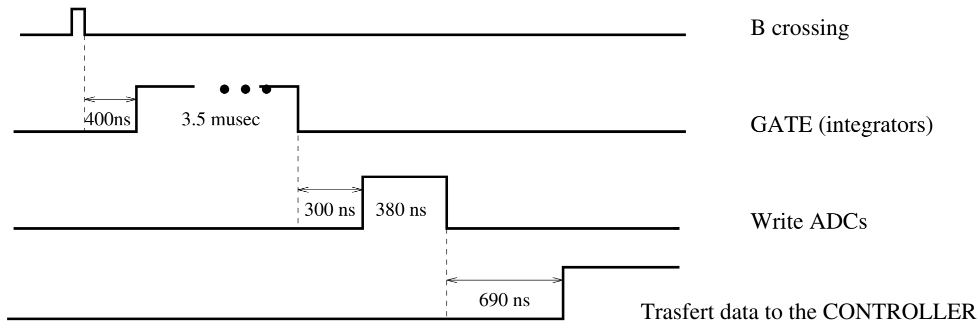

Figure A.8: Timing scheme for the INTEGRATOR operating configuration.

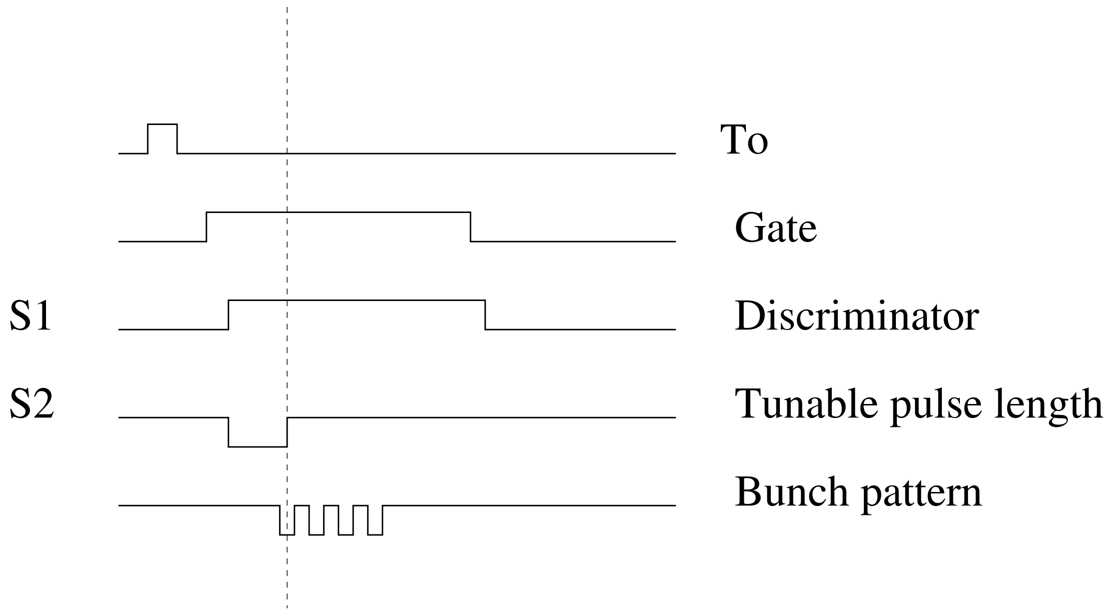

Figure A.9: Timing scheme for the bunch tag. The closing edge of the discriminator pulse must lie inside the window corresponding to one of the 4 bunchlets.

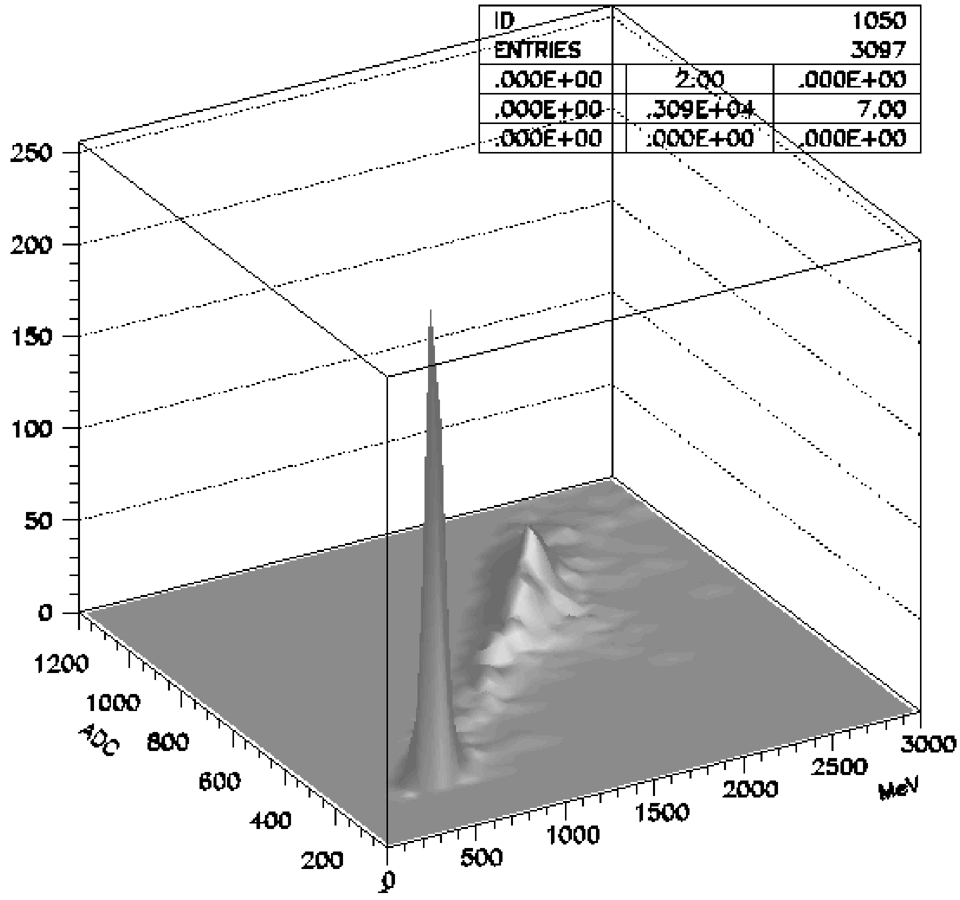

Figure A.10: DAQ(MeV) - Trigger(ADC) correlation for events with the ALR trigger on. The total energy deposited in the detector for each event is plotted. Data corresponding to a 45 GeV run.

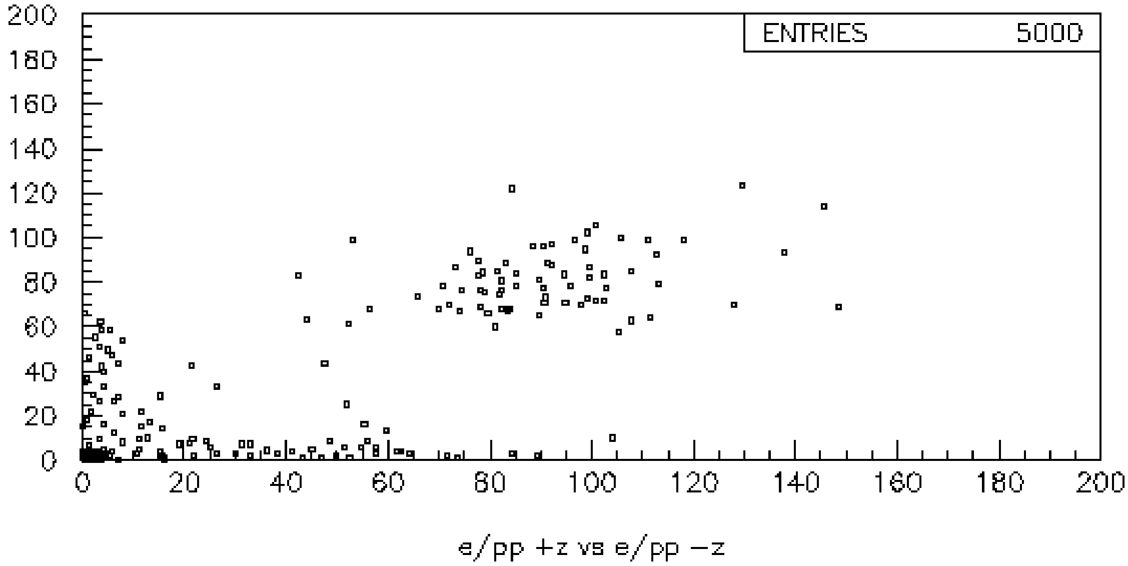

Figure A.11: Correlation between the mean energy per scintillator (e/pp) in the e^+ side with the same quantity in the e^- side. The Bhabha's are well separated and located around a value of e/pp = 100 MeV.

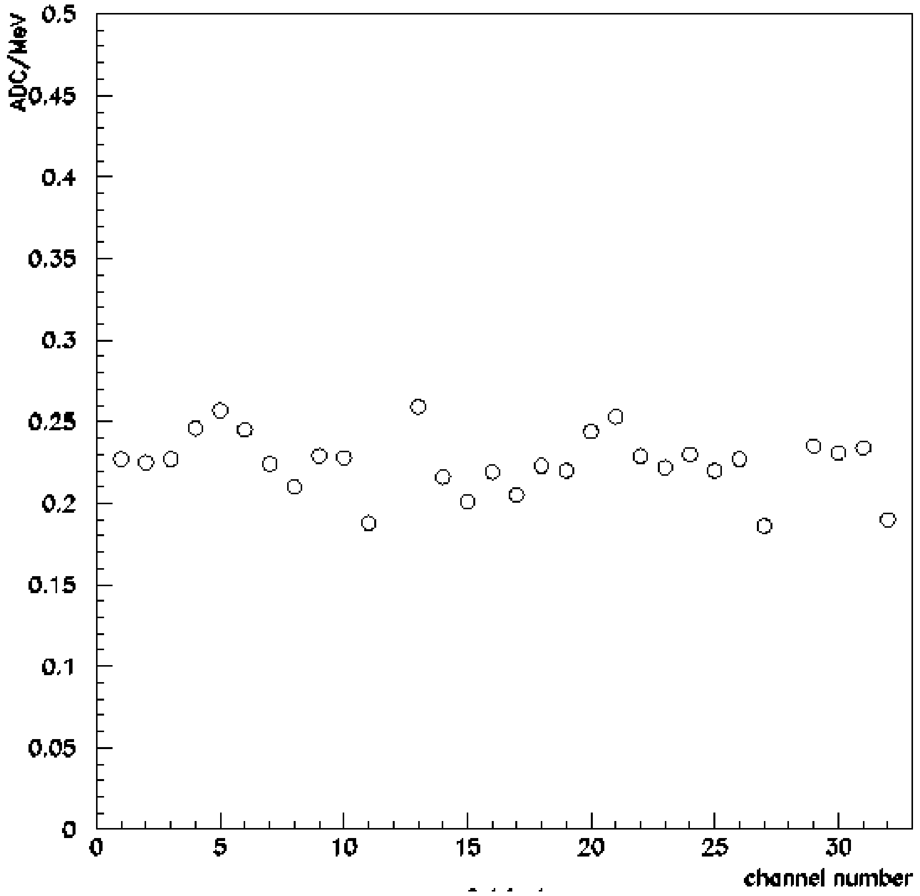

Figure A.12: Calibration factors for all the ALR trigger channels.

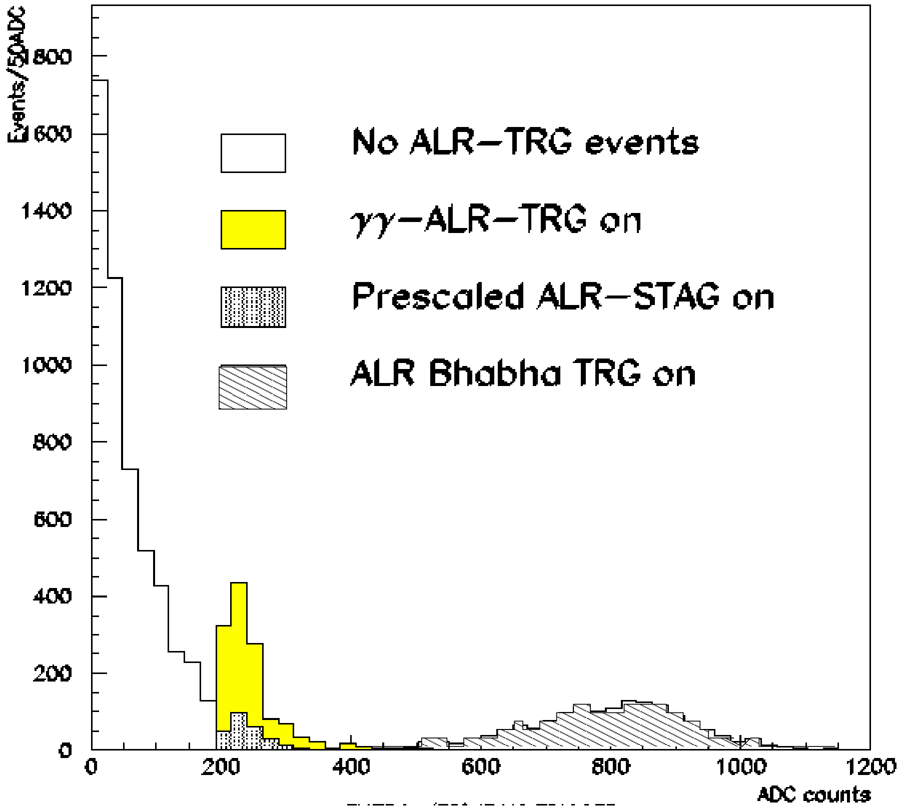

Figure A.13: Energy distribution (trigger line ADC counts) in the ALR. The pick at 0 ADC corresponds to events kept by another trigger of L3, while the Bhabha's are clearly visible around 800 ADC's. The total energy in the ALR is plotted.

Appendix B

The SMD Detector

Our first contribution to the L3 experiment has been given during the assembling of the Silicon Microvertex Detector (SMD). Therefore the SMD design deserves to be exposed in more details. The project for the construction of a silicon microvertex detector (SMD) began in 1991. The philosophy was to use well known technologies allowing to complete the project in less than two years. As already noted in Chap. 3 the SMD basic unit is a ladder built from four silicon sensors. A total of 24 ladders are mounted on a 1 m long carbon fiber-Nomex honeycomb composite structure, arranged into two cylindrical layers of 12 ladders each. The alignment and the mechanical structure have already been discussed in paragraph 3.3.1 (see also Fig. 3.7). Each ladder is given mechanical rigidity by a carbon fiber Ω-shaped stiffener, glued on the $r-\phi$ side of the four silicon sensors.

B.1 Sensors

The silicon sensors are based on the technology used by the ALPEH's vertex detector. Each half-ladder consists of two double-sided 300 μm thick silicon sensors of 4×7 cm^2 area. The sensor is made of a layer of high resistivity n silicon plate. To detect charges produced by traversing ionizing particles, both faces are doped as shown in Fig. B.1. To perform an $r-\phi$ and z coordinate measurement, the strips are implanted parallel to the beam axis in the $r-\phi$ side, and orthogonal to the beam axis in the z side (Fig. B.2). Since the readout electronics has been located at the extremities of the half-ladders, a special fanout circuit has been designed to read the transverse strips on z side. A 50 μm thick Kapton cable [133] with L-shaped copper strips has been used to bring the z-strips signal to the readout electronics.

The implantation strip pitch is 25 μm for strips parallel to the beam and 50 μm for strips orthogonal to the beam. Readout pitches are 50 μm on $r - \phi$ side and 150/200 μm in the central/forward region of the z side. An additional implant along the perimeter of both sides (a double p^+ implantation on the p-side and a similar implantation but in n^+ in the ohmic side), the guard ring, allows for the containment of surface currents. Moreover by a punch-through mechanism on the junction side

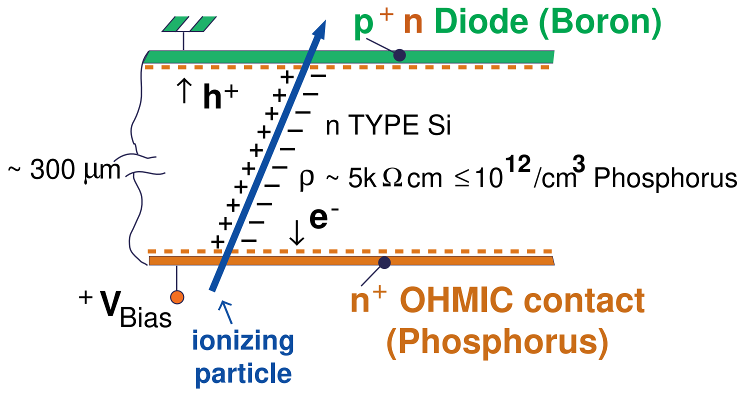

Figure B.1: The pn junction of an SMD sensor.

and by charge accumulation on the ohmic side, all the implantations are kept at the same potential. Thus the guard ring, which is also the bias ring, brings both the readout and the intermediate interpolation strips to the same voltage potential creating a uniform potential field below all the strips. A good inter-strip resistivity is performed by implanting p-stops between each pair of n-strips.

Capacitors of 150 pf with a typical breakdown voltage of 45 V are used to AC-coupling the sensors to the front end electronics [134]. Separate 128-element, 48 μm pitch capacitor chips are used for this purpose.

B.2 The Mechanical Structure and the Assembling

The general mechanical structure of an half-ladder is made of two sensors, a quartz thermal breaker and an aluminium nitrate plate. The whole system is glued together as shown in Fig. B.3. All the pieces have been glued using high precision vacuum jigs and holders. The precision required during the gluing has been 6 μm in positioning and 8 μm over 28 cm in alignment. Moreover the half-ladder surface is known to be planar within 20 μm. All the elements are connected by micro-bonding. There are 5 different bonding geometries as depicted in Fig. B.3. The most critical operation of the assembly has been the Kapton to capacitor bonding due to the geometrical constraints and instabilities of the Kapton substrate. Nevertheless a bonding failure rate less 1% on the total 220000 SMD bonds has been achieved. A carbon fiber Ω-shaped stiffener ("rib"), glued on the $r-\phi$ side, is used to assemble two half-ladders insuring in the meantime the mechanical rigidity of the ladder. Unfortunately in correspondence of the carbon fiber rib, the coupling of the strips to the external electromagnetic noise is modified. Hence the sensor baseline, on the $r-\phi$ assumes a particular shape in correspondence of the stiffener. This rib effect is large and leads to a saturation of the readout electronics in a non negligible fraction of the events (see Fig. B.4 top). Nevertheless, by wire connecting the rib to the readout electronics ground potential, the problem was solved (Fig. B.4 bottom).

B.3 The Readout Electronics

The preamplifier used for the strips readout is the radiation hard version of the SVX chip developed at LBL for the CDF silicon microstrip detector. The radiation hard version, the SVX-H is produced at UTMC with a CMOS technology with a minimum feature size of 1.2 μm. Each SVX-H chip contains 128 channels. A

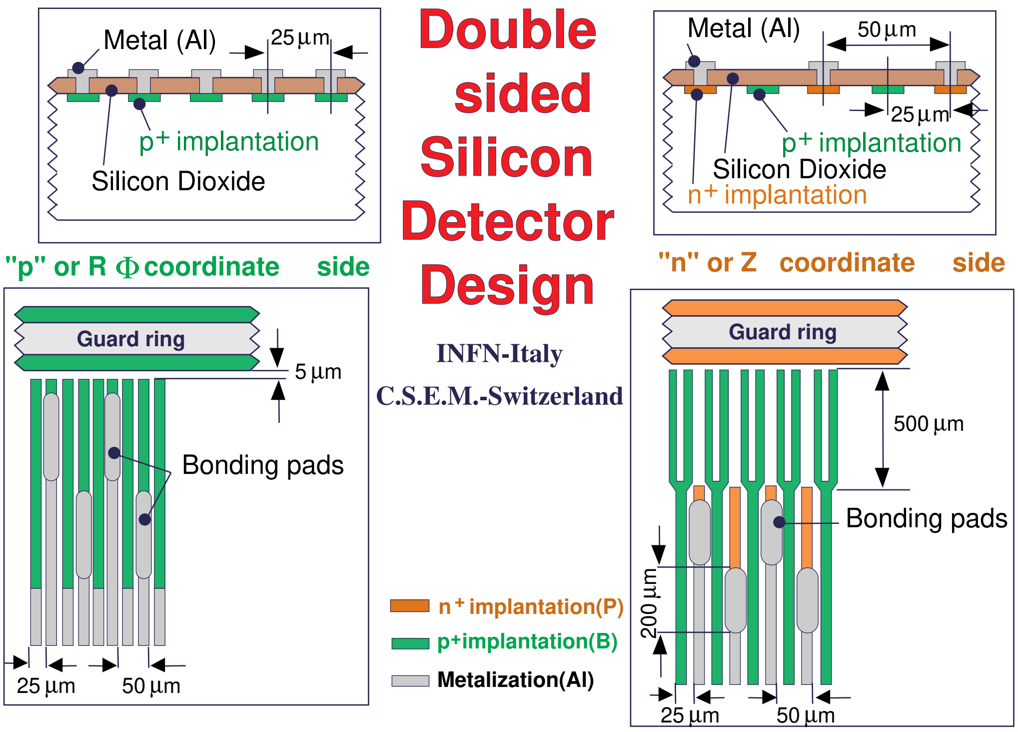

Figure B.2: General view of the double sided silicon sensor design.

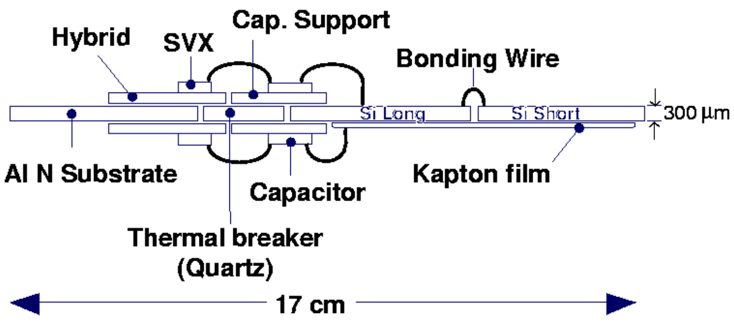

Figure B.3: Half ladder side view.

channel is subdivided in a high gain amplifier section followed by a stage of sample and hold, threshold storage, comparator, latch and digital circuitry to control the readout and calibration cycles. A single readout channel schema and the general logical layout of the whole SVX is shown in Fig. B.5. During the readout, the value of the integrated charge of each channel is placed on the single analog OUT, while at same time the channel address is presented on the digital bus. Two configurations of the integration cycles are possible: the Double Sample and Hold and The Quadruple Sample and Hold. In the former configuration, the voltage level at the integrator output is measured before and after the beam crossing with a fixed integration time Δt. The output signal is then the difference between the two measurements. This configuration allows for a removal of offset effects and helps to filter low frequency noise but, the intrinsic noise rises by a factor of $\sqrt{2}$. In the latter configuration, two Double Sample and Hold are performed before and after the beam crossing and their difference is taken as the output signal. Although in this case the leakage current effects are suppressed, the intrinsic noise rise by a factor $2\sqrt{2}$. Since the SMD strips are AC coupled to the readout through capacitors, the Simple and Hold scheme has been adopted.

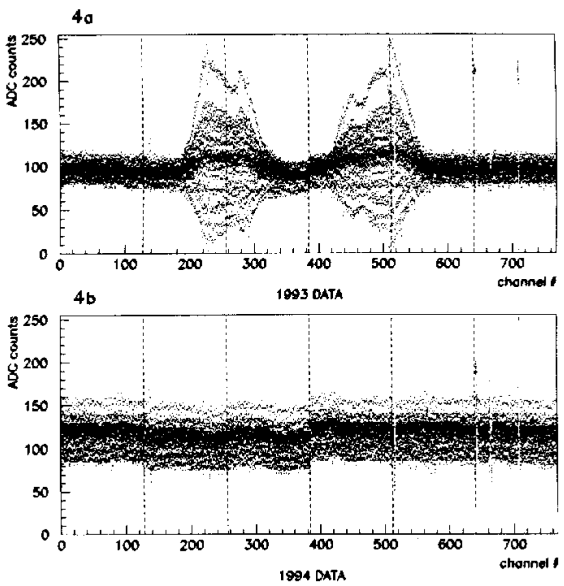

Figure B.4: Raw ADC data as function of the channel number. Several events have been superimposed for the same ladder. a) 1993 data b) 1994 data.

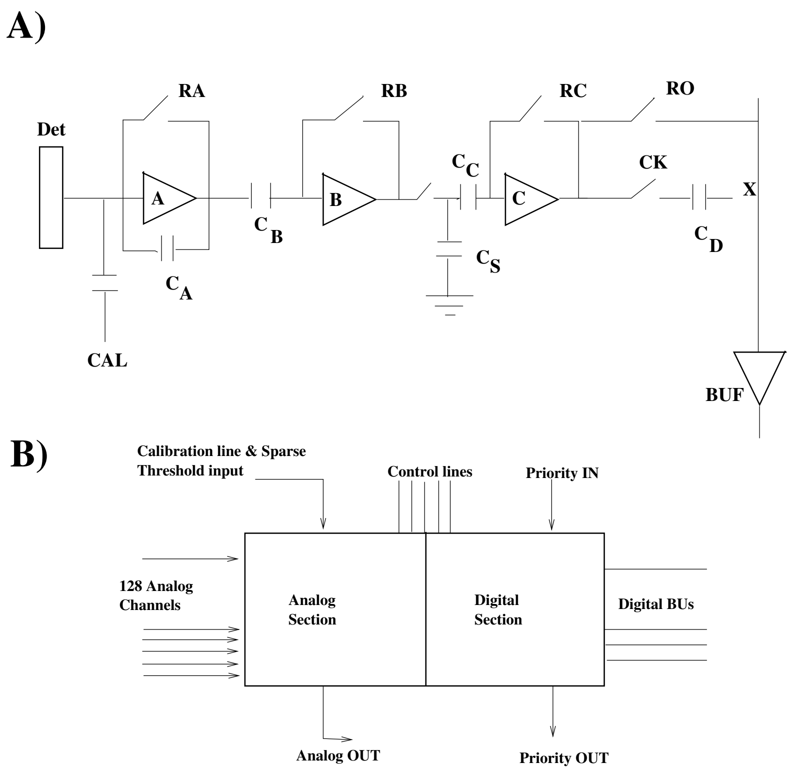

Figure B.5: Logical layout of a single analog SVX channel A) and of the whole SVX chip.

List of Figures

List of Tables

Bibliography

[1] D. Haidt and H. Pietschmann, *Electroweak Interactions*, vol. 10 of *Landolt-Börnstein: Numerical Data and Functional Relationships in Science and Technology.* Springer-Verlag, 1988.

[2] J. Adams. Annual Report to the CERN Council, 1979.

[3] S. Weinberg *Phys. Rev. Lett.* **1264** (1967) Lett. 19.

[4] A. Salam, *Elementary Particle Theory.* Almquist and Wiksell Publishers in Stockholm, 1968.

[5] **L3** Collaboration, B. Adeva *et. al.*, "The Construction of the L3 Experiment", *Nucl. Inst. Meth.* **A289** (1990) 35.

[6] **ALEPH** Collaboration, D. Decamp *et. al. Nucl. Inst. Meth.* **A294** (1990) 121.

[7] **OPAL** Collaboration, K. Ahmet *et. al. Nucl. Inst. Meth.* **A305** (1991) 275.

[8] **DELPHI** Collaboration, P. Abreu *et. al. Nucl. Inst. Meth.* **A303** (1991) 233.

[9] **TOPAZ** Collaboration, I.Levine *et. al.*, "Measurement of the Electromagnetic Coupling at Large Momentum Transfer", *Phys. Rev. Lett.* **78** (January, 1997) 424.

[10] G. Altarelli *et. al.*, "Physics at LEP2", CERN 96-01, February, 1996. Vol. 1,2.

[11] A. Ali and P. Söding, eds., *High Energy Electron-Positron Physics*, vol. 1 of *Advanced Series on Directions in High Energy Physics*, (Singapore), World Scientific, 1988.

[12] I. Wilson and H. Henke, "The LEP Main Ring Accelerating Structure", CERN-89-09.

[13] S. Myers, "The LEP Collider From Design to Approval and Commissioning", CERN-91-08.

[14] J. S. Kapustinsky *et. al.*, "The Design and Construction of a Double Sided Silicon Microvertex Detector for the L3 Experiment at CERN", *Ieee Trans. Nucl. Sci.* **41** (1994) 772.

[15] A. Adam *et. al.*, "Performance on Test Beam of the L3 Double Sided Silicon Microstrip Detector", *Nucl. Instrum. Meth.* **A348** (1994) 436.

[16] O. Adriani *et. al.*, "The New Double Sided Silicon Microvertex Detector for the L3 Experiment", *Nucl. Instrum. Meth.* **A348** (1994) 431.

[17] **L3 SMD** Collaboration, M. Acciarri *et. al.*, "The L3 Silicon Microvertex Detector", *Nucl. Instrum. Meth.* **A351** (1994) 300–312.

[18] A. Santocchia *et. al.*, "Design and Construction of Double Sided Silicon Ladders for the L3 Microvertex Detector", *Nucl. Instrum. Meth.* **A344** (1994) 133.

[19] B. Bertucci *et. al.*, "Upgrade of the Active Lead Ring (ALR) for LEP 200 Physics", L3 note 1504, 1993.

[20] W. Carithers *et. al. Nucl. Instrum. Meth.* **A289** (1990) 388.

[21] A. Akbari *et. al. Nucl. Instrum. Meth.* **A332** (1993) 33.

[22] H. Anderhub *et. al. Nucl. Instrum. Meth.* **A252** (1986) 357.

[23] H. Anderhub *et. al. Nucl. Instrum. Meth.* **A263** (1988) 1.

[24] N. Produit, *Le déclanchement par les particules chargées dans l'expérience L3 et applications à la physique de la collision de deux photons.* PhD thesis, Université de Genève, 1991.

[25] G. Forconi, *Algorithmes de reconstruction pour le filtrage en ligne et application à la mesure de la section efficace de la collision* $e^+e^- \longrightarrow (e^+e^-)\eta_c$ *avec le système de digitalisation rapide pour la chambre à vertex de l'expérience L3.* PhD thesis, Université de Genève, 1993.

[26] **L3** Collaboration, J. A. Bakken *et. al.*, "Performance of a Prototype BGO Calorimeter in an Electron Beam from 2-GeV to 50-GeV", *Nucl. Instr. Meth.* **A254** (1987) 535.

[27] F. Sauli, *Instrumentation in High Energy Physics.* Singapore World Scientific, 1992.

[28] M. Goyot *et. al. Nucl. Inst. Meth.* **A263** (1988) 180.

[29] J. Wenninger, *Mesure des paramètres électro-faibles du* Z^o *avec la ráction* $e^+e^- \longrightarrow e^+e^-(\gamma)$. PhD thesis, Université de Genève, 1992.

[30] W. Ruckstuhl, "Stability of the BGO Intercalibration from the Xenon System", L3 note 649, 1989.

[31] W. R. J. Wenninger, "Energy Scale and Resolution in the BGO: Contribution of the Xenon Monitoring System", L3 note 766, 1990.

[32] G. Morand, "Developpement et utilisation du systeme de moniteur au Xenon du calorimètre electromagnetique de L'experience L3", L3 note 1016, 1991.

[33] U. Uwer, "The L3 Scintillation Counter System", L3 note 1400, 1991.

[34] Y. Galaktinov *et. al. Nucl. Inst. Meth.* **A251** (1986) 258.

[35] A. Arefief *et. al. Nucl. Inst. Meth.* **A285** (1989) 403.

[36] **L3** Collaboration, "Technical Proposal", May, 1983.

[37] Berdugo *et. al.*, "The Alignment of the Forward-Backward Muon Chambers", L3 note 1909.

[38] I. Brock *et. al.*, "Luminosity Measurement in the L3 Detector at LEP", CERN-PPE/96-89, June, 1996.

[39] M. Chemarin *et. al.* To be published in Nucl. Instrum. Meth.

[40] M. Chemarin *et. al.*, "Test Beam Results for an Upgraded Forward Tagger of the L3 Experiment at LEP2", *Nucl. Instrum. Meth.* **A349** (1994) 345–355.

[41] R. Bizzarri *et. al.*, "The L3 Energy Trigger", *Nucl. Inst. Meth.* **A283** (1989) 799.

[42] R. Bizzarri *et. al.* *Nucl. Inst. Meth.* **A317** (1992) 463.

[43] M. Bourquin *et. al.*, "The New Level-1 Trigger for the Forward-Backward Active Lead Ring Calorimeter at L3", L3 note 2138, 1997. To be Published in Nucl. Inst. Meth.

[44] G. Susinno and A. Bay, "Trigger for the L3 Upgraded Forward Backward Tagger (ALR+) at LEP II", L3 note 1601, 1994.

[45] M. Bourquin *et. al.*, "Charged Particle Trigger for the L3 Experiment", in *Int. Conf. on the impact of Digital Microelectronics and Microprocessors on Particle Physics*, (Trieste), ICTP, 1988.

[46] P. Bene *et. al.* *Nucl. Inst. Meth.* **A306** (1991) 150.

[47] H. Hoorani, *The Level-1 Charged Particle Trigger of L3 Detector and the study of Two-Photon Production of e^+e^- and $\mu^+\mu^-$ Pairs in Untagged Events.* PhD thesis, Université de Genève, 1996.

[48] T. Dai and M. Fukushima, "L3 Level-1 Muon Trigger", L3 note 668, 1988.

[49] S. Beingessner *et. al.* *Nucl. Inst. Meth.* **A340** (1994) 322.

[50] V. Budnev *et. al.* *Phys. Rep.* **15C** (1975) 181.

[51] V. Baier *et. al.*, “Inelastic Processes in High Energy Quantum Electrodynamics“, *Phys. Rep.* **78** (1981), no. 3 293–393.

[52] H. Euler and B. Kokel *Nat. Wiss.* **23** (1935) 246.

[53] K. Mikaelian *Phys. Lett.* **115B** (1982) 267.

[54] H. Meyer, “Photons from the Universe New Frontiers in Astronoomy.“, CERN hep-ph/9710362, October, 1997.

[55] F. Stecker *et. al.* *Ap. J.* **L49** (1992) 390.

[56] D. Burke *et. al.*, “Positron Production in Multiphoton Light-by-Light Scattering“, *Phys. Rev. Lett.* **79** (September, 1997) 1626.

[57] C. Anderson *Phys. Rev.* **41** (1932) 405.

[58] L. Landau and E. Lifshitz *Sov. Phys.* **6** (1934) 244.

[59] A. Halprin *et. al.* *Phys. Rev.* **152** (1966) 1295.

[60] V. Bolakin *et. al.* *Phys. Lett.* **34B** (1971) 663.

[61] G. Barbiellini *et. al.* *Phys. Rev. Lett.* **32** (1974) 385.

[62] C. Berger and W. Wagner, “Photon-Photon Reactions.“, *Phys. Rep.* **146** (1987) 1.

[63] **L3** Collaboration, O. Adriani *et. al.*, “Measurement of η_c Production in Untagged Two-Photon Collisions at LEP“, *Phys. Lett.* **B318** (1993) 575.

[64] R. Rizzo, “Study of the η' Formation in Two-Photon Collisions“, L3 note 1963, 1996.

[65] T. van Rhee and A. Buijs, “χ_{c2} Formation in Photon-Photon Collisions“, L3 note 1781, 1995.

[66] S. Söldner-Rembold, "The Structure of the Photon", Talk given at the XVIII International Symposium on Lepton Interactions, August, 1997.

[67] J. Sakurai and D. Schildknecht *Phys. Lett.* **B41** (1972) 489.

[68] S. Brodsky and G. P. Lepage *Phys. Rev.* **D24** (1981) 1808.

[69] F. K. J.H. Field and L. Poggioli *Phys. Lett.* **B181** (1986) 362.

[70] T. Walsh *Phys. Lett.* **36B** (1971) 121.

[71] H. Behrend *et. al. Phys. Lett.* **126B** (1983) 384.

[72] J. Field in *Photon '95* (J. Miller, ed.), (Singapore), World Scientific, 1995. Summary talk.

[73] P. Kessler in *Photon '95* (J. Miller, ed.), (Singapore), World Scientific, 1995.

[74] C. Peterson *et. al. Nucl. Phys* **229B** (1983) 301.

[75] K. Ackers *et. al. Z. Phys.* **60C** (1993) 593.

[76] P. Abreu *et. al. Z. Phys.* **69C** (1996) 223.

[77] K. Ackerstaff *et. al.* CERN-PPE/96-153, 1996.

[78] P. Bevington and D. Robinson, *Data Reduction and Error Analysis for the Physical Sciences.* McGraw-Hill Inc., second ed., 1992.

[79] F. Berends *et. al. Comp. Phys. Comm.* **40** (1986) 285.

[80] J. Vermaseren *Nucl. Phys.* **B229** (1983) 347.

[81] F. Berends *et. al. Comp. Phys. Comm.* **40** (1986) 271.

[82] F. Berends *et. al. Nucl. Phys* **B253** (1985) 441.

[83] F. Berends *et. al. Comp. Phys. Comm.* **40** (1986) 309.

[84] R. Kleiss *Nucl. Phys.* **B241** (1984) 145.

[85] J. A. M. Vermaseren, "Two-Photon Processes at Very High Energy", *Nucl. Phys.* **B229** (1983) 347.

[86] G. Lepage *J. Comp. Phys.* **27** (1978) 192.

[87] W. L. van Neerven and J. A. M. Vermaseren, "Radiative Corrections to Two-Photon Physics, Including Effects from Nonperipheral Diagrams",. Talk given at the 8th Warsaw Symp. on Elementary Particle Physics, Kazimierz, Poland, May 27-31, 1985.

[88] W. L. van Neerven and J. A. M. Vermaseren, "Radiative Corrections to Two-Photon Physics", *Nucl. Phys.* **B238**.

[89] E. Laenen and G. Schuler, "Model-Independent QED Corrections to Photon Structure Function Measurements", CERN-TH/97-193, August, 1997.

[90] K. Affholderbach and G. Cowen, "Unfolding the Photon Structure Function", Contribution to the Proceedings of the Phenomenology Workshop on LEP2 Physics, Oxford, April, 1997.

[91] L. Collaboration, "Cross Section of Hadron Production in $\gamma\gamma$ Collisions at LEP", CERN PPE/97-48, June, 1997.

[92] V. Blobel. Proceedengs from 1994 CERN School of Computing, 1994.

[93] I. Nedelkov, "Improper Problems in Computational Physics", *Comp. Phys. Comm.* **4** (1972) 157.

[94] G. D'Agostini *Nucl. Inst. Meth.* **A362** (1995) 487.

[95] J. Allison *et. al.*, *Formulae and Methods in Experimental Data Evaluation.* European Physical Society (Computational Physics Group), 1984. Page 7.

[96] A. Höcker and V. Kartvelishvili. LAL-95/55, 1995.

[97] M. Thomson. CERN-PPE/96-055, 1996.

[98] W. Press *et. al.*, *Numerical Recipes in Fortran.* Cambridge University Press, 1992. page 796.

[99] C. Shannon in *Key Papers in The Development of Information Theory* (D. Slepian, ed.), (New York), IEEE Press, 1974.

[100] M. Hafidouni, "Correction of Measured Multiplicity Distributions by a Method Based on the Maximum Entropy Principle", CERN PPE/93-28, June, 1993.

[101] M. Schmelling. CERN CN/93-03, 1993.

[102] A. Savitzky and M. Golay in *Analytical Chemistry*, vol. 36, pp. 1627–1639. 1964.

[103] R. Engel *Z. Phys.* **C66** (1995) 203.

[104] T. Sjöstrand *Comput. Phys. Commun.* **82** (1994) 74.

[105] G. Susinno, "Tagged Dilepton Production in $\gamma\gamma$ Interactions at LEP with the L3 Detector", in *Deep Inelastic Scattering and Related Phenomena* (G. D'Agostini and A. Nigro, eds.), p. 269, World Scientific, 1996.

[106] R. Bizzarri *et. al. Nucl. Inst. Meth.* **A317** (1992) 463.

[107] **PEP-9** Collaboration, M. Cain *et. al. Phys. Lett.* **B147** (1984) 232.

[108] **PLUTO** Collaboration, C. Berger *et. al. Z. Phys.* **C27** (1985) 249.

[109] **MARKJ** Collaboration, B. Adeva *et. al. Phys. Rev.* **D38** (1988) 2665.

[110] G. Schuler and T. Sjöstrand, "Parton Distribution of the Virtual Photon", CERN-TH/96-04, January, 1996.

[111] G. Susinno, "Iterative Matrix Correction Approach to Data Unfolding.", L3 Note 1996, October, 1996.

[112] R. Nisius, "Results on Photon Structure Functions from LEP.", Talk at the International Europhysics Conference on High Energy Physics, August, 1997.

[113] **ZEUS** Collaboration, M. Derrick *et. al. Z. Phys.* **C65** (1995) 379.

[114] **H1** Collaboration, T. Ahmed *et. al. Nucl. Phys.* **B439** (1995) 471.

[115] H. Abramowicz *et. al. Phys. Lett.* **B269** (1991) 458.

[116] D. Duke and J. Owens *Phys. Rev.* **D26** (1982) 1600.

[117] **OPAL** Collaboration, K. Ackerstaff *et. al. Z. Phys* **C74** (1997) 33.

[118] *Z. Phys.* **C69** (1996) 33.

[119] M. Althoff *et. al. Z. Phys.* **C31** (1986) 527.

[120] H. Aihara *et. al. Z. Phys.* **C34** (1987) 1.

[121] C. Berger *et. al. Phys. Lett.* **B142** (1984) 111.

[122] S. Ting. L3 Note 1687.

[123] **L3** Collaboration, P.Bagnaia *et. al. Nucl. Instr. Meth.* **323** (1992) 528.

[124] **L3** Collaboration, P.Bagnaia *et. al. Nucl. Instr. Meth.* **324** (1993) 101.

[125] M. Chemarin *et. al.* L3 Note 1504, 1994.

[126] BC408 from Bicron Corporation P.O. Box 3093, 3760 DB Soest, The Netherlands.

[127] B. mouëllic. Note CERN/PS202, 1989. and references therein.

[128] "HAMAMATSU S6262-02/03", tech. rep., Hamamatsu Photonics, 1126-1 Hamamatsu City, 435 Japan.

[129] CERN, *GEANT Detector Description And Simulation Tool*, program library long writeup w 5013 ed.

[130] "A Low Noise Shaping Amplifier with Triggering Channel for Photodiode Readout.", Preprint LYCEN 8679 and L3 Note 408. IPN Lyon Group.

[131] National Semiconductor Corporation, *Application Note 813, A.P. Neves.*, 1992.

[132] *Wideband Transconductance Amplifiers (MAX435/MAX436)*, laser-& electronic-equipment ed. 19-0042; Rev 0/9/92.

[133] D. DiBitonto *et. al. Nucl. Instr. Meth.* **A338** (1994) 404.

[134] Batignani *et. al.*, "Development and Performance of Double Sided Silicon Strip Detectors", *Nucl. Instr. Meth.* **A310** (1991) 160.